Electromagnetic Vector-Sensor Direction-of-Arrival Estimation in the Presence of Interference

Daniel B. Tait

Thesis submitted to the Faculty of the
Virginia Polytechnic Institute and State University
in partial fulfillment of the requirements for the degree of

Master of Science
in
Electrical Engineering

R. Michael Buehrer, Chair
Harpreet S. Dhillon
Steven W. Ellingson

August 12, 2020
Blacksburg, Virginia

Keywords: Direction-of-Arrival Estimation, Array Signal Processing, ESPRIT,
Independent Component Analysis, Cyclostationarity, Higher-Order Statistics

Electromagnetic Vector-Sensor Direction-of-Arrival Estimation in the Presence of Interference

Daniel B. Tait

(ABSTRACT)

This research investigates signal processing involving a single electromagnetic vector-sensor, with an emphasis on the problem regarding signal-selective narrowband direction-of-arrival (DOA) estimation in the presence of interference. The approach in this thesis relies on a high-resolution ESPRIT-based algorithm. Unlike spatially displaced arrays, the sensor cannot estimate the DOA of sources using phase differences between the array elements, as the elements are spatially co-located. However, the sensor measures the full electromagnetic field vectors, so the DOA can be estimated through the Poynting vector. Limited information is available in the open literature regarding signal-selective DOA estimation for a single electromagnetic vector-sensor. In this thesis, it is shown how the Uni-Vector-Sensor-ESPRIT (UVS-ESPRIT) algorithm that relies on a time-series invariance and was originally devised for deterministic harmonic sources can be applied to non-deterministic sources. Additionally, two algorithms, one based on cyclostationarity and the other based on fourth-order cumulants, are formulated based on the UVS-ESPRIT algorithm and are capable of *selectively* estimating the source DOA in the presence of interference based on the statistical properties of the sources. The cyclostationarity-based UVS-ESPRIT algorithm is capable of selectively estimating the signal-of-interest DOA when the sources have the same carrier frequency, and thus overlap in frequency. The cumulant-based UVS-ESPRIT algorithm devised for this sensor relies on the independent component analysis algorithm JADE and is capable of selectively estimating the signal-of-interest DOA through the fourth-order cumulants only, is robust to spatially colored noise, and is capable of estimating the DOA of more sources than sensor elements.

Electromagnetic Vector-Sensor Direction-of-Arrival Estimation in the Presence of Interference

Daniel B. Tait

(GENERAL AUDIENCE ABSTRACT)

Electromagnetic vector-sensors are specialized sensors capable of capturing the full electromagnetic field vectors at a single point in space. Direction-of-arrival (DOA) estimation is the problem of estimating the spatial-angular parameters of one or more wavefronts impinging on an array. For a single electromagnetic vector-sensor, the array elements are not spatially displaced, but it is still possible to estimate the direction-of-arrival through the Poynting vector, which relates the electric and magnetic field vectors to the direction of propagation of an electromagnetic wave. Although direction-of-arrival estimation is a well-established area of research, there is limited discussion in the open literature regarding signal-selective DOA estimation in the presence of interference for a single electromagnetic vector-sensor. This research investigates this problem and discusses how the high-resolution Uni-Vector-Sensor-ESPRIT (UVS-ESPRIT) algorithm may be applied to non-deterministic sources. ESPRIT-based algorithms capable of selectively estimating the source DOA are formulated based on the cyclostationarity and higher-order statistics of the sources, which are approaches known to be robust to interference. The approach based on higher-order statistics is also robust to spatially colored noise and is capable of estimating the DOA of more sources than sensor elements. The formulation of the UVS-ESPRIT for higher-order statistics relies on the application of the independent component analysis algorithm JADE, an unsupervised learning technique. Overall, this research investigates signal-selective direction-of-arrival estimation using an ESPRIT-based algorithm for a single electromagnetic vector-sensor.

Contents

List of Figures

List of Tables

List of Abbreviations

AWGN Additive White Gaussian Noise

CRLB Cramer-Rao Lower Bound

DOA Direction-of-Arrival

EMVS Electromagnetic Vector-Sensor

ESPRIT Estimation of Signal Parameters via Rotational Invariant Techniques

JADE Joint Approximate Diagonalization of Eigenmatrices

MUSIC MUltiple SIgnal Classification

OFDM Orthogonal Frequency Division Multiplexing

PAM Pulse Amplitude Modulation

QAM Quadrature Amplitude Modulation

QPSK Quadrature Phase-Shift Keying

RMSE Root-Mean-Squared Error

SIR Signal-to-Interference Ratio

SNOI Signal-Not-of-Interest

SNR Signal-to-Noise Ratio

SOI Signal-of-Interest

UVS Uni-Vector-Sensor

Chapter 1

Introduction

This chapter first discusses the motivation behind the investigation into signal processing for a single electromagnetic vector-sensor and the relevance of DOA estimation. The general motivation behind conducting research into this subject is discussed and an explanation is provided into why additional algorithms based on cyclostationarity and higher-order statistics are investigated for estimating the DOA in the presence of interference.

After presenting the motivations, the prior contributions which form the basis of this work are provided to the reader. This includes a general discussion on DOA estimation and its relation to cyclostationary signal processing and higher-order statistics for array signal processing applications. Valuable references are provided to the reader that, so those who are interested in further exploration of this topic will know where to begin.

Finally, the distinctive contributions of this thesis to the DOA estimation problem for a single electromagnetic vector-sensor are presented and the content of each chapter is outlined.

1.1 Motivation

The direction-of-arrival estimation problem is related to the localization problem where the angular-spatial parameters of one or more wavefronts (also referred to as sources) impinging upon an array of sensors is estimated. The design of these sensors and the implementation of the DOA estimation algorithms in these systems can vary depending on the topology of the array because of the mapping between the wavefront and the array. For example, the approach taken towards applying DOA estimation algorithms to a uniform linear array of dipoles differs from those applied to a circular array [35]. In general, there are three classes of algorithms that may be applied to these sensor arrays: classical beamforming algorithms, parametric methods, and high-resolution subspace algorithms [55, 58]. The focus in this thesis is on a derivative of the high-resolution subspace algorithm ESPRIT for a single electromagnetic vector-sensor, termed Uni-Vector-Sensor ESPRIT by Wong and Zoltowski [61], and its application in the presence of interference.

One such sensor applicable to the DOA estimation problem is the electromagnetic vector-sensor. These sensors are comprised of three orthogonally oriented dipoles and three orthogonally oriented magnetic loops. The orthogonal orientation of the sensor elements provides the capability of capturing the full electric and magnetic field vectors at a point in space from the impinging wavefronts, which enables the sensor to uniquely estimate the DOA through the Poynting vector of its array manifold vectors [39]. In general, algorithms typically rely on interferometric approaches for spatially displaced elements, but the vector-sensor may have advantages over arrays with displaced dipoles. Chevalier suggests arrays with co-located elements may estimate the DOA of more sources than spatially displaced arrays [11].

The reader may ask why additional investigation into the direction-of-arrival estimation problem is warranted. Although direction-of-arrival estimation, and more broadly direction

finding, is an established area of research, it remains an active area of interest due to its breadth of applications in the modern world and the insatiable demand for higher performance and reduced complexity. The DOA estimation problem has found applications in a range of areas including wireless communications, radar, sonar, electronic warfare, and more [58]. There are civilian applications for DOA estimation, such as cognitive radio and its role in beamforming, as well as military applications. In some cases, these problems call for capabilities that selectively estimate the DOA of a signal-of-interest (SOI) through its statistical properties in the presence of interference.

Several algorithms have been devised that are applicable to a single electromagnetic vector-sensor. One example is the cross product estimator by Nehorai [39], although this approach can only reliably estimate the DOA of a single source in the absence of interference and has lower-resolution than ESPRIT-based subspace algorithms. Another approach is to compare the array manifold to a library of vectors through a search algorithm, but this requires a computationally expensive search and would perform poorly in the presence of interference. The high-resolution subspace algorithm MUSIC could also be applied [58, 60], but this also requires a computationally expensive search on the possible DOA of the impinging sources and information on the array manifold vectors.

The UVS-ESPRIT algorithm has several advantages over these algorithms. For example, it can estimate the DOA of two sources arriving from the same direction, provided the source polarization ellipticities are distinct, and is capable of estimating the DOA of multiple sources with distinct carrier frequencies [61]. Although the MUSIC algorithm can estimate the DOA through a 2D search of the spatial parameters, it would require a computationally prohibitive 4D search that includes the polarization parameters to achieve the same result. In contrast, the ESPRIT algorithm is faster because it does not rely on a search algorithm.

The investigation in this thesis focuses on ESPRIT-based algorithms, particularly those that

selectively estimate the DOA of a signal-of-interest based on its statistical properties. The basis for these approaches is the UVS-ESPRIT algorithm devised for harmonic sources [61]. Further, it is shown that UVS-ESPRIT itself may be applied to digital (or more generally, non-deterministic) sources under certain conditions. This capability is implied in papers by Xi and You that exploit non-deterministic signal properties [64, 66], but the approach towards this warrants investigation. The performance of the UVS-ESPRIT algorithm when applied to digital sources can also degrade, however, due to the spectral overlap between the source carriers that are responsible for the time-series invariance of the ESPRIT algorithm. Spectral overlap refers to overlap between the frequency spectra of the sources. The degree of overlap and its effect on the performance depends on the source bandwidth, carrier frequency spacing, and the source spatial and polarization parameters. An algorithm based on ESPRIT and cyclostationarity is shown to improve the performance in the case of spectral overlap, even if the sources have the same carrier frequency, but the algorithm based on ESPRIT and higher-order statistics does not.

The selective estimation of the source DOA when there are interferers present exploits the statistical properties of the signals-of-interest, particularly through the source cyclostationarity and higher-order statistics. DOA estimation algorithms based on cyclostationarity and the fourth-order cumulants are known to selectively estimate the DOA of sources [21, 38]. The performance of these algorithms in terms of the root-mean-square error (RMSE) is dependent on these statistical properties, however. The cyclic ESPRIT algorithm estimates the DOA based on the cyclostationary properties, while the algorithm based on higher-order statistics estimates the DOA based on the fourth-order cumulants. It is shown that the DOA of more sources than sensor elements can be estimated through the application of higher-order statistics to a single electromagnetic vector-sensor.

Overall, this thesis investigates direction-of-arrival estimation involving a single electromag-

netic vector-sensor and the problem of selectively estimating the source DOA based on cyclostationarity and higher-order statistics in the presence of interference. It expands upon the UVS-ESPRIT algorithm for harmonic sources through the formulation of algorithms based on non-deterministic signal properties, particularly cyclostationarity and higher-order statistics, that can selectively estimate the source DOA.

1.2 Prior Work

This thesis focuses on the application of DOA estimation algorithms to a single electromagnetic vector-sensor that are capable of selectively estimating the source DOA in the presence of interference. It primarily builds upon the work by Wong and Zoltowski, who first applied the UVS-ESPRIT algorithm to a single electromagnetic vector-sensor for the case of harmonic sources [61]. A scan of the literature reveals much of the work on the electromagnetic vector-sensor was pioneered by Wong and Zoltowski [71]. However, origins may be traced to Nehorai, who devised a model for the electromagnetic vector-sensor [39]. One example of more recent work in the area of DOA estimation for arrays of electromagnetic vector-sensors is discussed by Ho, et al. [32]. The availability of the full electromagnetic field information in antenna arrays allows for unique capabilities. For example, one paper by Wong and Zoltowski discusses DOA estimation through arbitrarily spaced electromagnetic vector-sensors at unknown locations [62]. There is limited information on DOA estimation involving a single electromagnetic vector sensor, although some papers have discussed this subject, such as the paper by Wang et al. that discusses a reduced-dimensionality UVS-MUSIC algorithm [60]. Nehorai also devised algorithms for tracking using the electromagnetic vector-sensor (EMVS) through the cross-product [40]. A paper on estimating DOA for a single vector-sensor when the phase is a polynomial is discussed by Yuan [67].

One ESPRIT-based algorithm improves the performance of UVS-ESPRIT through the use of mixed-order statistics [66]. Another paper proposes several algorithms for a single vector-sensor and is able to estimate the DOA of sources with the same carrier, but relies on linear polarization and non-circular source constellations [64]. One approach is described by Jhiang and Zhang using inner products [29]. Another approach by Tao et al. applied the Stokes parameters [54]. Although algorithms have been developed for this sensor, little is discussed on algorithms involving cyclostationarity, higher-order statistics, and selective estimation of the source DOA more generally.

Much of this thesis draws from DOA estimation using the established subspace techniques, with a focus on the ESPRIT algorithm. Major contributions in this area include the formulation of the ESPRIT algorithm by Roy and Kailath [45, 53] and the MUSIC algorithm by Schmidt [48]. General discussions related to this subject may be further explored in the comprehensive texts by Madisetti and Vijay [35] and Van Trees [59]. Many variants of these subspace algorithm have been investigated. Material that more thoroughly addresses the subject of direction-of-arrival estimation may be found in the text by Tuncer [58] and various authors in the volume by Theodoridis [55]. This is a well-researched topic and the literature reveals that there are many ways to approach the DOA estimation problem.

One way to approach DOA estimation is through cyclostationary signal processing techniques, which allow for selective estimation based on cyclostationary properties and improved performance in the case of spectral overlap with interfering sources. Important contributors to the area of cyclostationary signal processing include Gardner [21, 22] and Napolitano [37]. An example of DOA estimation techniques involving cyclostationarity signal processing is the paper by Zhi et al. [70] and Gardner [19]. Napolitano has written an insightful survey on the state of cyclostationary signal processing and its wide range of applications, including DOA estimation [38]. The DOA estimation problem can exploit far more than source

cyclostationarity, however.

In addition to cyclostationarity, the DOA estimation problem can be approached through the fourth-order cumulants. It was originally found that higher-order statistics may be applied to the DOA estimation problem through MUSIC by Pan and Nikias [42] and to ESPRIT by Chiang and Nikias [12]. A tutorial on cumulants [36] and a comprehensive overview on the application of cumulants to array processing are discussed in the popular series of papers by Mendel [16, 17, 23, 24, 25, 57]. This includes a paper on direction finding in the fourth paper of the series [25]. Of particular interest is the concept of virtual array aperture extension discussed by Mendel as well as Chevalier [11]. Cumulants can also be applied to DOA estimation algorithms as discussed by Cardoso [7]. Cardoso suggests that more sources than sensor elements may be resolved through the cumulant tensor in the blind source separation problem [6], which has also been discussed by Chevalier [11].

One approach used in this thesis is the application of independent component analysis to the DOA estimation problem for a single electromagnetic vector-sensor, which is used in the cumulant ESPRIT algorithm. For the cases discussed in this paper, the algorithm referred to as joint approximate diagonalization of eigenmatrices (JADE) by Cardoso [8] is applied both by itself and to the cumulant-based ESPRIT algorithm. This algorithm exploits the fourth-order cumulant tensor and provides all the advantages of cumulants in array processing. Other papers discussing how to apply independent component analysis to the DOA estimation problem are discussed by Sawada and Cardoso [8, 47]. Overall, this thesis builds upon a great deal of prior work.

1.3 Contributions

This thesis contributes to the field in the following ways.

- It is shown how the UVS-ESPRIT algorithm for a single vector-sensor may be applied to non-deterministic (or stochastic) sources, rather than just harmonic sources.
- Developed approaches that selectively estimate the DOA of signals-of-interest in the presence of interference based on cyclostationarity and higher-order statistics. The approach based on cyclostationarity is shown to improve performance when an interferer shares the same carrier frequency or spectrally overlaps with a signal-of-interest.
- An ESPRIT-based method for the single electromagnetic vector-sensor is developed that relies on the fourth-order cumulants and an application of independent component analysis to estimate the array manifold matrix and obtain the DOA.

1.4 Outline

The chapters that succeed this are organized as follows.

- Chapter 2, Background. This chapter presents a brief overview of relevant technical information. This includes the basis of the electromagnetic vector-sensor models used in our simulations, a discussion on direction-of-arrival estimation algorithms and the application of ESPRIT to the electromagnetic vector-sensor, an explanation of relevant performance metrics, as well as a brief discussion of cyclostationarity and higher-order statistics.
- Chapter 3, Algorithm Formulation. This chapter first formulates the UVS-ESPRIT

algorithm for non-deterministic sources assuming pulse-amplitude-modulated digital sources. The chapter then builds upon this algorithm through its application to cyclostationarity and fourth-order cumulants. These algorithms are capable of selectively estimating the DOA of sources based on their statistical properties. In addition, there is a discussion on the number of resolvable source DOAs with the electromagnetic vector-sensor.

- Chapter 4, Results and Discussion. The performance of the algorithms discussed in the previous chapter are simulated and compared. Approaches involving cyclostationarity and higher-order statistics are shown to be capable of selectively estimating the source DOA. The effect on performance due to spectral overlap with regards to these algorithms is also discussed. The chapter also provides a discussion on the limitations and capabilities of these algorithms, such as estimating the DOA of more sources than sensor elements, then concludes with a concise summary of the advantages and disadvantages of each algorithm.

- Chapter 5 Conclusions. The thesis is concluded with a summary of the findings and a discussion on the implications for future work.

Chapter 2

Background

This chapter discusses the relevant technical background involving direction-of-arrival estimation for a single electromagnetic vector-sensor. First, the model of the electromagnetic vector-sensor and the signals used throughout the simulations are presented. This provides the reader with an understanding of notation and its mathematical background. A model showing the approach to the problem when there is interference present and the DOA of sources are selectively estimated is also presented.

Then, background on the subspace algorithms for direction-of-arrival estimation algorithms is presented and it is shown how the ESPRIT algorithm can be adapted to a single electromagnetic vector-sensor. This presents the UVS-ESPRIT algorithm devised by Wong and Zoltowski [61] that the algorithms relying on cyclostationarity and higher-order statistics are based upon.

Finally, central ideas behind cyclostationarity and higher-order statistics are discussed. This allows readers who are not familiar with these concepts to understand their relevance to the direction-of-arrival estimation problem.

2.1 Modeling

2.1.1 Electromagnetic Vector-Sensor Model

In this section, a mathematical description for modeling the electromagnetic vector-sensor is provided. This model makes the narrowband assumption, all sources are located in the far-field, and the incident sources are treated as transverse electromagnetic plane waves traveling through a homogeneous medium. All sensor elements are treated as isotropic radiators. The described model has been confirmed to be an accurate representation of a real electromagnetic vector-sensor [39]. The electromagnetic vector-sensor has been built and tested by Antonio et al. [3] as well as Appadwedula and Keller [4].

The direction finding problem for an arbitrary array with a spatially uncorrelated complex additive white Gaussian noise (AWGN) channel may be modeled below as in 2.1 and may be represented using matrix notation as in 2.2 when there are a finite number of discrete samples, where bandwidth is assumed to be twice the sampling rate.

The notation for the continuous signal model in 2.1 is defined below.

- M is the total number of sensor elements
- K is the total number of sources
- $x_k(t) \in \mathbb{C}$ is the kth source
- $\boldsymbol{y}(t) \in \mathbb{C}^{M\times 1}$ is received signal vector
- $\boldsymbol{w}(t) \in \mathbb{C}^{M\times 1}$ circularly additive white Gaussian noise vector with variance σ_w^2
- $\boldsymbol{a}(\boldsymbol{\psi}_k) \in \mathbb{C}^{M\times 1}$ is the array steering vector for the kth source

- $\boldsymbol{\psi}_k$ is a vector containing the direction and polarization parameters of the kth source, the parameters are described later

$$\boldsymbol{y}(t) = \sum_{k=1}^{K} \boldsymbol{a}(\boldsymbol{\psi}_k) x_k(t) + \boldsymbol{w}(t) \tag{2.1}$$

The notation for the matrix representation of the data after being discretely sampled over some finite-duration time window is shown in 2.2 and is also defined below.

- N is the number of snapshots
- $\boldsymbol{X} \in \mathbb{C}^{K \times N}$ is the matrix of source data
- $\boldsymbol{Y} \in \mathbb{C}^{M \times N}$ is the matrix of received data
- $\boldsymbol{W} \in \mathbb{C}^{M \times N}$ is the matrix of complex AWGN
- $\boldsymbol{A}(\boldsymbol{\psi}) \in \mathbb{C}^{M \times K}$ is the matrix of steering vectors

$$\boldsymbol{Y} = \boldsymbol{A}(\boldsymbol{\psi})\boldsymbol{X} + \boldsymbol{W} \tag{2.2}$$

The model of the electromagnetic vector-sensor itself is now discussed. A visual representation of the EMVS is presented in Figure 2.1 and is comprised of three orthogonally oriented dipoles and three magnetic loops which measure the full electromagnetic field data at a point in space. Mathematically, the array manifold vector may be viewed as a product of the mapping between the directional and polarization parameters of the source as shown in 2.3 and 2.4. The array steering vector is a non-linear mapping between the signal and the received data vector. Since the sensor measures the full electromagnetic field, the array manifold matrix (also referred to as the array steering vector matrix) contains the electric and magnetic field vectors. The upper and lower sections of the steering vector are partitioned into

the three scalar electric and three magnetic field components in the Cartesian coordinate system. The free space impedance has also been neglected by convention. This result was established by Nehorai and Paldi [39]. An informative discussion on the polarization is given by DeSchamps [15]. In the EMVS case, the steering vector is a function of both the direction and polarization parameters.

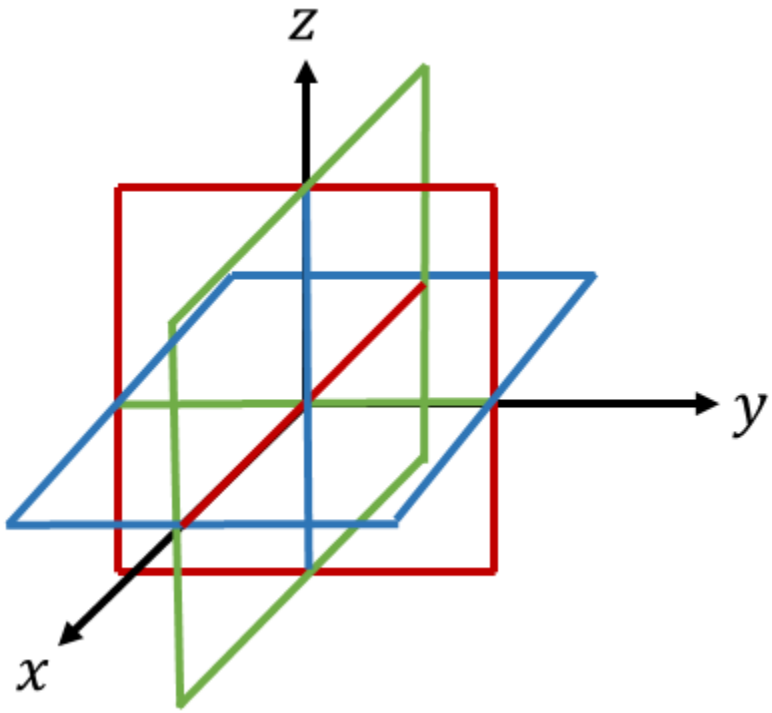

Figure 2.1: Visual representation of a single electromagnetic vector-sensor, comprised of both dipole and magnetic loop antennas. The x-oriented elements are shown in red, the y-oriented elements are shown in green, and the z-oriented elements are shown in blue.

- $\boldsymbol{\psi_k} = [\,\theta_k \quad \phi_k \quad \gamma_k \quad \eta_k\,]^T$ is the argument of the steering vector
- $\theta_k \in [0, \pi)$ and $\phi_k \in [0, 2\pi)$ are the elevation and and azimuth angles respectively in the spherical coordinate system, with θ_k defined from the positive z-axis
- $\gamma_k \in [0, \pi/2)$ and $\eta_k \in [-\pi, \pi)$ are the polarization phase angle (determines ellipticity) and polarization phase difference (between the electric and magnetic fields) respectively

$$\boldsymbol{a}(\boldsymbol{\psi}_k) = \boldsymbol{g}_\Theta(\theta_k, \phi_k)\boldsymbol{g}_p(\gamma_k, \eta_k) = \begin{bmatrix} e_x(\theta_k, \phi_k, \gamma_k, \eta_k) \\ e_y(\theta_k, \phi_k, \gamma_k, \eta_k) \\ e_z(\theta_k, \gamma_k, \eta_k) \\ h_x(\theta_k, \phi_k, \gamma_k, \eta_k) \\ h_y(\theta_k, \phi_k, \gamma_k, \eta_k) \\ h_z(\theta_k, \gamma_k) \end{bmatrix} \tag{2.3}$$

$$\boldsymbol{g}_\Theta(\theta_k, \phi_k) = \begin{bmatrix} \cos\phi_k \cos\theta_k & -\sin\phi_k \\ \sin\phi_k \cos\theta_k & \cos\phi_k \\ -\sin\theta_k & 0 \\ -\sin\phi_k & -\cos\phi_k \cos\theta_k \\ \cos\phi_k & -\sin\phi_k \cos\theta_k \\ 0 & \sin\theta_k \end{bmatrix}, \quad \boldsymbol{g}_p(\gamma_k, \eta_k) = \begin{bmatrix} \sin\gamma_k e^{j\eta_k} \\ \cos\gamma_k \end{bmatrix} \tag{2.4}$$

In some cases there is interest in DOA estimation when interference is present. Interference refers to sources that are not estimated by the DOA algorithm and degrade performance [70]. For example, some algorithms selectively estimate the DOA of sources based on the statistical characteristics of the signals present, and sources without these characteristics would be considered interferers, while those being selectively estimated are considered signals-of-interest. This is depicted in Figure 2.2. When interference is present, the models presented in 2.5 and 3.5 are adopted.

- L is the total number of interferers
- $i_l(t) \in \mathbb{C}$ is the lth interferer

$$\boldsymbol{y}(t) = \sum_{k=1}^{K} \boldsymbol{a}(\boldsymbol{\psi}_k) x_k(t) + \sum_{l=1}^{L} \boldsymbol{a}(\boldsymbol{\psi}_l) i_l(t) + \boldsymbol{w}(t) \tag{2.5}$$

- $\boldsymbol{X}_S \in \mathbb{C}^{K \times N}$ and $\boldsymbol{X}_I \in \mathbb{C}^{L \times N}$ are the matrices of signal-of-interest and interferer data respectively
- $\boldsymbol{\psi} = (\boldsymbol{\psi}_{soi}^T, \boldsymbol{\psi}_{int}^T)^T$ is a vector containing the direction and polarization parameters of all sources

$$\boldsymbol{Y} = \boldsymbol{A}(\boldsymbol{\psi}_{soi}) \boldsymbol{X}_S + \boldsymbol{A}(\boldsymbol{\psi}_{int}) \boldsymbol{X}_I + \boldsymbol{W} \tag{2.6}$$

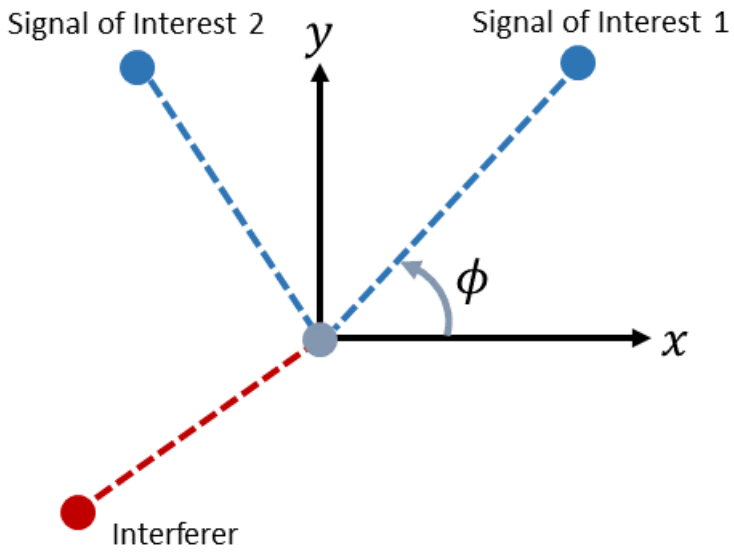

Figure 2.2: Visual representation of the problem with three sources present. In this case, the DOA of the two signals-of-interest would be estimated, while the interferer would be neglected. All sensor elements are located at the origin.

2.1.2 Signal Model

The signal model varies throughout the discussions in Chapter 4. In all cases, the complex bandpass representation described in 2.7 is applied, with a digital carrier frequency f_k measured in cycles/sample, signal power σ_k^2, and a phase offset $\psi_k \sim \text{Unif}[0, 2\pi)$. Signal-to-noise ratio (SNR) is determined by the ratio of the signal and noise power (σ_w^2), whereas signal-to-interference ratio (SIR) is determined by the ratio of the signal-of-interest power to the total power of the interferers. The simplest signal considered is the deterministic harmonic signal (or "tone") where $s_k(t) = 1$.

$$x_k(t) = \sigma_k s_k(t) e^{j2\pi f_k + j\psi_k} \tag{2.7}$$

In addition to the harmonic signal model, there is consideration of digital sources encoded through pulse amplitude modulation and multi-carrier orthogonal frequency-division multiplexing (OFDM). The source with pulse amplitude modulation (PAM) is represented as shown in 2.8 and is discussed by Proakis [44]. Here, the symbol period is denoted T_{sym}, b_i are the iid symbols sampled from a complex discretely uniform distribution that depends on the modulation scheme, such as quadrature amplitude modulation (QAM) or quadrature phase shift keying (QPSK), the parameter T_o is a uniform random variable sampled such that $T_r \sim \text{Unif}[0, T_{sym})$ to introduce statistical variation between signals when there are multiple sources present, and the function $p(\cdot)$ is a waveform denoting the pulse shaping. PAM sources generally use raised-cosine pulse shaping, although square pulse-shaping is considered for the higher-order statistics.

$$s_{PAM,k}(t) = \sum_{i=-\infty}^{\infty} b_{i,k} p_k(t - iT_{sym,k} - T_{o,k}) \tag{2.8}$$

There is also consideration of OFDM sources shown in 2.9 and described by Cho et al. [13]. The parameters in common with the PAM signal are the same. There are N_{SC} subcarriers and the waveform $g_n(\cdot)$ contains the ith symbol of the nth subcarrier generated by of the system. The parameters of greatest interest for this signal are the symbol period, which is such that $T_{sym} = T_g + T_{sub}$, where T_g is the guard interval and T_{sub} is the subcarrier interval. A visual description of the time-domain signal for one symbol period is shown in Figure 2.3. These OFDM signals use a cyclic prefix and raised-cosine or square windowing.

$$s_{OFDM,k}(t) = \sum_{n=1}^{N_{SC}} \sum_{i=-\infty}^{\infty} b_{n,i,k} g_{n,k}(t - iT_{sym,k} - T_{o,k}) \tag{2.9}$$

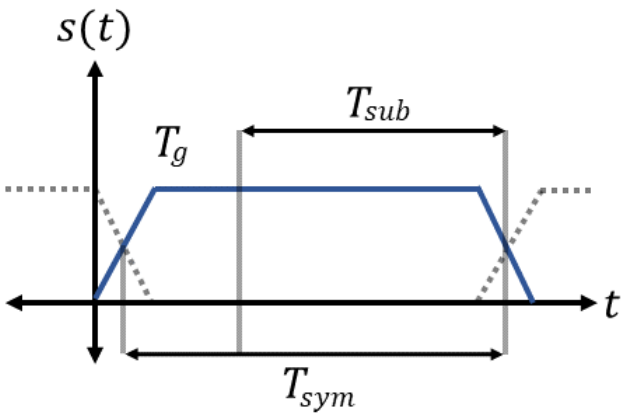

Figure 2.3: Time-domain representation showing the windowing and guard interval of an OFDM subcarrier.

2.2 Direction-of-Arrival Estimation with Subspace Techniques

Most direction finding algorithms can be categorized into the classical direction finding algorithms, such as the conventional beamformer and minimum-variance distortionless response, the parametric methods which exploit data directly, such as covariance matching, or as the high-resolution subspace techniques. A comprehensive overview of direction finding algorithms can be found in the text by Tuncer [58] and various authors in the fifteenth chapter of the volume by Theodoridis discussed by Haardt et al. [55]. This thesis focuses on the application of ESPRIT-based subspace techniques due to its high performance and speed. In traditional arrays, the array elements are spatially displaced and the phase difference between them is used to estimate the DOA, but in this case the sensor elements do not have spatial displacement.

The subspace algorithms exploit the signal and noise subspaces obtained from the eigendecomposition of the correlation matrix $\boldsymbol{R}_y$. The signal and noise subspaces are a vector-space that describes a statistical mapping of the signals which have been mixed into the sensor according to the array manifold vectors.

The correlation matrix may be defined as below.

$$\boldsymbol{R}_y = E[\boldsymbol{y}(t)\boldsymbol{y}^H(t)]$$

For discretely-sampled finite data, the biased sample correlation matrix may then be estimated as $\hat{\boldsymbol{R}}_y$.

$$\hat{\boldsymbol{R}}_y = \frac{1}{N}\boldsymbol{Y}\boldsymbol{Y}^H$$

The concept of signal and noise subspace is well-described by Proakis [43] and authors in the volume by Theodoridis [55]. First, assume that λ_i are the eigenvalues for the noiseless case and are ordered, such that $\lambda_1 \geq \lambda_2 \geq \cdots \geq \lambda_M$. In the noiseless case, only the eigenvalues $\{\lambda_1, \ldots, \lambda_K\}$ are nonzero and the orthonormal eigenvectors $\{\boldsymbol{e}_1, \ldots \boldsymbol{e}_K\}$ span what is referred to as the signal subspace. When the additive noise is introduced, the eigendecomposition below is obtained.

$$\begin{aligned}
\boldsymbol{R}_y &= \boldsymbol{A}\boldsymbol{R}_s\boldsymbol{A}^H + \sigma_w^2\boldsymbol{I} \\
&= \sum_{i=1}^{K} \lambda_i \boldsymbol{e}_i\boldsymbol{e}_i^H + \sum_{i=1}^{M} \sigma_w^2 \boldsymbol{e}_i\boldsymbol{e}_i^H \\
&= \sum_{i=1}^{K} (\lambda_i + \sigma_w^2)\boldsymbol{e}_i\boldsymbol{e}_i^H + \sum_{i=K+1}^{M} \sigma_w^2 \boldsymbol{e}_i\boldsymbol{e}_i^H
\end{aligned}$$

It can be seen that the set of eigenvectors $\{\boldsymbol{e}_1, \ldots \boldsymbol{e}_K\}$ spans the signal subspace and the set of eigenvectors $\{\boldsymbol{e}_{K+1}, \ldots \boldsymbol{e}_M\}$ spans what is referred to as the noise subspace. These signal and noise subspaces may be used to make inferences about source parameters, such as the DOA, as the eigenvectors of the signal and noise subspaces are related to the array manifold vectors. The subspace algorithm ESPRIT relies on the signal subspace, whereas the subspace algorithm MUSIC relies on the noise subspace.

2.2.1 Uni-Vector-Sensor ESPRIT Algorithm

ESPRIT-based algorithms estimate signal parameters through the signal subspace [45]. To apply ESPRIT, two data sets are taken from sub-arrays of an array, such that there is a spatially- or temporally-invariant phase difference between the two data sets. This unitary phase difference between the data sets $\mathbf{\Phi}$ is referred to as the rotation operator and acts as a reference between the two signal subspaces.

Typically, the ESPRIT algorithm relies on the spatial invariance between two data sets, but this is not possible with a single electromagnetic vector-sensor due to the collocation of its sensor elements. The application of this algorithm to the vector-sensor relies on an unconventional temporal displacement of the data, which is not typically used in the DOA estimation problem for arrays. Although, ESPRIT-based algorithms exploiting time-series may be applied to parametric estimation [44, 46] and have found applications in a multiple-invariance approach [53], they typically rely on spatial displacement for the case of DOA estimation. The ESPRIT algorithm applied to a single EMVS is able to obtain the DOA through its array manifold, so spatial displacement is unnecessary.

To apply the ESPRIT algorithm to a single vector-sensor, the temporal-invariance must be exploited through the phase difference between two data sets of samples [61]. This algorithm is termed the "UVS-ESPRIT" algorithm by Wong to emphasize the requirement of a single electromagnetic vector-sensor. It is assumed that the carrier frequencies of each source are different, so the temporal displacement between the data sets, $\tau = \Delta T$, results in a distinct phase offset such that the rotation operator $\mathbf{\Phi} = \text{diag}(e^{j2\pi f_1 \Delta T}, \ldots, e^{j2\pi f_K \Delta T})$. Note that the equality $\boldsymbol{y}_2(t) = \boldsymbol{y}_1(t - \Delta T)$ holds true only for the harmonic signal model.

$$\boldsymbol{y}_2(t) = \boldsymbol{y}_1(t - \Delta T) = \sum_{k=1}^{K} e^{j2\pi f_k \Delta T} \boldsymbol{a}(\boldsymbol{\psi}_k) s_k(t) e^{-j2\pi f_k t} + \boldsymbol{w}(t)$$

$$\tilde{\boldsymbol{y}}(t) = \begin{bmatrix} \boldsymbol{y}_1(t) \\ \boldsymbol{y}_2(t) \end{bmatrix} = \begin{bmatrix} \boldsymbol{A} \\ \boldsymbol{A}\boldsymbol{\Phi} \end{bmatrix} \boldsymbol{x}(t) + \boldsymbol{w}(t)$$

For the noiseless case, the sample correlation matrix of the data $\boldsymbol{R}_y$ would then be partitioned between the data sets as follows.

$$\boldsymbol{R}_y = \begin{bmatrix} \boldsymbol{A}\boldsymbol{R}_s\boldsymbol{A}^H & \boldsymbol{A}\boldsymbol{R}_s\boldsymbol{\Phi}^H\boldsymbol{A}^H \\ \boldsymbol{A}\boldsymbol{\Phi}\boldsymbol{R}_s\boldsymbol{A}^H & \boldsymbol{A}\boldsymbol{\Phi}\boldsymbol{R}_s\boldsymbol{\Phi}^H\boldsymbol{A}^H \end{bmatrix} = \frac{1}{N} \begin{bmatrix} \boldsymbol{Y}_1\boldsymbol{Y}_1^H & \boldsymbol{Y}_1\boldsymbol{Y}_2^H \\ \boldsymbol{Y}_2\boldsymbol{Y}_1^H & \boldsymbol{Y}_2\boldsymbol{Y}_2^H \end{bmatrix}$$

The signal subspace $\boldsymbol{E}_s$ is then obtained from the upper and lower partitions of the correlation matrix as shown below.

$$\boldsymbol{E}_s = \begin{bmatrix} \boldsymbol{E}_1 \\ \boldsymbol{E}_2 \end{bmatrix} = \begin{bmatrix} \boldsymbol{A}\boldsymbol{T} \\ \boldsymbol{A}\boldsymbol{\Phi}\boldsymbol{T} \end{bmatrix}$$

The eigendecomposition between the upper and lower partitions of the correlation matrix results in two signal subspaces that are related through the rotation operator $\boldsymbol{\Phi}$, which are the eigenvalues of $\boldsymbol{\Psi}$ described below.

$$\boldsymbol{E}_1\boldsymbol{\Psi} = \boldsymbol{E}_2 \implies \boldsymbol{T}\boldsymbol{\Psi} = \boldsymbol{\Phi}\boldsymbol{T} \implies \boldsymbol{\Psi} = \boldsymbol{T}^{-1}\boldsymbol{\Phi}\boldsymbol{T}$$

The matrix $\boldsymbol{\Psi}$ is then estimated through the total least squares estimate. Alternatively, the ordinary least squares method may be applied [45]. The total least squares estimate is selected since noise will be introduced. To apply the total least squares estimate, the matrix $\boldsymbol{U}$ is obtained from a singular value decomposition of the augmented matrix containing the signal subspace eigenvectors $\boldsymbol{E}_{12}^H\boldsymbol{E}_{12} = \boldsymbol{L}\boldsymbol{\Sigma}\boldsymbol{U}^H$, where the augmented matrix $\boldsymbol{E}_{12} = [\boldsymbol{E}_1|\boldsymbol{E}_2]$. The total least squares estimate is computed through the upper and lower right quadrants of $\boldsymbol{U}$, such that $\boldsymbol{\Psi}_{TLS} = -\boldsymbol{V}_{12}\boldsymbol{V}_{22}^{-1}$.

$$\boldsymbol{U} = \begin{bmatrix} \boldsymbol{V}_{11} & \boldsymbol{V}_{12} \\ \boldsymbol{V}_{21} & \boldsymbol{V}_{22} \end{bmatrix}$$

Finally, the eigenvalues of $\boldsymbol{\Psi}$ are the diagonal elements of $\boldsymbol{\Phi}$ and the right eigenvectors of $\boldsymbol{\Psi}$ are given by $\boldsymbol{E}_\Psi = \boldsymbol{T}^{-1}$. In spatially displaced arrays, the DOA can be estimated from the elements of $\boldsymbol{\Phi}$. However, the UVS-ESPRIT algorithm estimates it through the matrix of array steering or array manifold vectors denoted as $\hat{\boldsymbol{A}}$.

$$\hat{\boldsymbol{A}} = \frac{1}{2}\left(\boldsymbol{E}_1\boldsymbol{E}_\Psi + \boldsymbol{E}_2\boldsymbol{E}_\Psi\boldsymbol{\Phi}^{-1}\right)$$

Since the array manifold vectors contain the full electromagnetic field data, the DOA can be inferred through the Poynting vector. In electromagnetism, the Poynting vector describes

the spatial direction in which power travels through the propagation of an electromagnetic wave and is related to the electric and magnetic field vectors through the cross product. Therefore, this vector may be obtained through the six measured scalar electric and magnetic field components.

$$\hat{\boldsymbol{p}}_k = \frac{\hat{\boldsymbol{e}}_k}{||\hat{\boldsymbol{e}}_k||} \times \frac{\hat{\boldsymbol{h}}_k^*}{||\hat{\boldsymbol{h}}_k||} = \begin{bmatrix} \hat{u}_{x,k} \\ \hat{u}_{y,k} \\ \hat{u}_{z,k} \end{bmatrix}$$

Finally, the DOA estimates for the electromagnetic vector-sensor are obtained from the preceding unit vector and its relation to the spatial parameters.

$$\hat{\theta}_k = \arccos\big(\hat{u}_{z,k}\big), \quad \hat{\phi}_k = \arctan\big(\hat{u}_{y,k}/\hat{u}_{x,k}\big)$$

The source carrier frequencies are estimated from Φ_k, which are the diagonal elements of $\boldsymbol{\Phi}$.

$$\hat{f}_k = \frac{\angle \Phi_k}{2\pi \Delta T}$$

Although not of interest in this thesis, the polarization parameter estimators are included for completion. This is discussed by Wong and Zoltowski [61].

$$\hat{\gamma_k} = \sum_{n=1}^{N} \arctan \frac{\hat{g}_{k_1}(t_n)}{\hat{g}_{k_2}(t_n)}$$

$$\hat{\eta_k} = \sum_{n=1}^{N} \angle \hat{g}_{k_1}(t_n)$$

$$\hat{\boldsymbol{g}_k} = \begin{bmatrix} \hat{g}_{k_1} \\ \\ \hat{g}_{k_2} \end{bmatrix} = [\boldsymbol{g}_{\boldsymbol{\Theta}}^H(\hat{\theta}_k, \hat{\phi}_k)\boldsymbol{g}_{\boldsymbol{\Theta}}(\hat{\theta}_k, \hat{\phi}_k)]^{-1}\boldsymbol{g}_{\boldsymbol{\Theta}}^H(\hat{\theta}_k, \hat{\phi}_k)\hat{\boldsymbol{a}}_k$$

2.3 Performance Metrics

Root-Mean-Square Error

The DOA estimation algorithms may be evaluated according to the root-mean-square error and the Cramer-Rao lower bound. The RMSE for the azimuth and elevation is the conventional metric used to evaluate the performance of DOA estimation algorithms. An alternative metric has been proposed by Nehorai in his original paper on the electromagnetic vector sensor [39], but the RMSE is preferred because the units are in degrees.

The RMSE is the root of the mean-square error. The sample RMSE is presented in 2.10, where T are the number of trials, θ is the true parameter (e.g. the azimuth or elevation), and $\hat{\theta}$ is the estimated parameter. The subscript t denotes the index of the estimated parameters for the tth trial.

$$\begin{aligned} RMSE &= \sqrt{MSE} \\ &= \sqrt{(E[(\theta - \hat{\theta})^2]} \\ &= \sqrt{\frac{1}{T}\sum_{t=1}^{T}(\theta - \hat{\theta}_t)^2} \end{aligned} \tag{2.10}$$

The MSE is a measure of both the estimator variance (precision) and bias (accuracy) from the true parameter [10].

$$MSE = \text{Var}[\theta] + (\text{Bias}[\theta])^2$$

Cramer-Rao Lower Bound

The Cramer-Rao lower bound (CRLB) provides a lower bound on the variance of an unbiased estimator and is a reference against an ideal estimator. Although the full derivation for the CRLB for a single electromagnetic vector-sensor is not presented here, the reader may be referred to the derivation by Wong and Yuan [63, 67]. The bounds presented in the figures throughout the writing are shown in 2.11 and 2.12 are for the deterministic single source case, where σ_w^2 is the noise power and N is the number of snapshots.

In general, the source elevation in each trial are selected at random, but from a value close to $\theta = 90°$. Therefore, the bound is still expected to convey meaningful information. Fixing the elevation of the bound in this way also generalizes it for an arbitrary polarization. However, this constraint may influence the performance as the number of sources increases, due to the linear dependence among the source array manifold vectors [31].

$$CRLB_\theta = \frac{\sigma_w^2}{2N} \tag{2.11}$$

$$CRLB_\phi = \frac{\sigma_w^2}{2N} \frac{1}{(1 + (\cos\theta)^2[1 - 2(\cos\eta)^2 - 2(\cos\gamma)^2(\sin\eta)^2])}\bigg|_{\theta=90°} = \frac{\sigma_w^2}{2N} \tag{2.12}$$

2.4 Cyclostationarity

A stochastic process is considered cyclostationary (or almost-cyclostationary in the case of incommensurate periods) when it possesses moments that are periodic in the time-domain. For example, a moment periodic in $\tau = T_0$, as shown in 2.13, would exhibit cyclostationarity in the wide sense, due to the periodicity of its second-order moment. This may be compared to the requirement for periodicity for a continuous time-domain signal when the relation $x(t) = x(t + T_0)$ holds true for any t.

$$E[x(t)x^*(t)] = E[x(t+\tau)x^*(t)] \quad \forall t \in (-\infty, \infty) \tag{2.13}$$

The periodic nature of the statistics latent to cyclostationary signals lends itself to a convenient interpretation referred to as the fraction-of-time framework, in contrast with the stochastic framework. Although it is not applied in depth here, a comprehensive discussion of cyclostationary signal processing and the fraction-of-time framework is documented by Gardner [21] and Napolitano [22, 37].

With the fraction-of-time framework, a deterministic interpretation of cyclostationary signals is possible due to the periodic nature of the statistics which occur over infinitely long periods of time [21]. The time-average operator is then defined as in 2.14, which is used to evaluate the expectation of cyclostationary signals.

$$\langle \cdot \rangle \triangleq \lim_{T \to \infty} \frac{1}{T} \int_{-T/2}^{T/2} (\cdot) dt \tag{2.14}$$

In the case of second-order periodicities, an almost-cyclostationary signal with cycle frequency α would be considered cyclostationary when the cyclic autocorrelation function

is nonzero for α. For commensurate periods, the cycle frequency may be represented as $\alpha = k/T_0$ where k is an integer and T_0 is the period in 2.13. The cyclic autocorrelation function defined by Napolitano [37] for complex-valued signals is shown in 2.15, where the expectation to obtain the cyclic autocorrelation of a specified cycle frequency denoted $E^{\alpha}[\cdot]$ extracts the cyclic autocorrelation function from the autocorrelation function.

$$\begin{aligned} R_x^{\alpha}(\tau) &= E^{\alpha}[R_x(t,\tau)e^{-j2\pi\alpha t}] \\ &= \langle R_x(t,\tau)e^{-j2\pi\alpha t}\rangle \\ &= \langle x(t+\tau/2)x^*(t-\tau/2)e^{-j2\pi\alpha t}\rangle \end{aligned} \tag{2.15}$$

The cyclic autocorrelation functions for each cycle frequency may be interpreted as Fourier coefficients of the autocorrelation function. Therefore, it can be found that the power in the cyclic components of the cyclostationary signals will be less than the total signal power, which is related to the cyclic Wiener-Khinchin theorem (or Gardner relation) [37]. The autocorrelation function may be recovered from the sum of the nonzero cyclic autocorrelation functions as shown in 2.16. The set A denotes the cycle frequencies where $R_x^{\alpha}(\tau) \neq 0$.

$$R_x(t,\tau) = \sum_{\alpha\in A} R_x^{\alpha}(\tau)e^{-j2\pi\alpha t} \tag{2.16}$$

The cyclic autocorrelation possesses a signal selectivity property that has applications in DOA estimation, as it is possible to selectively estimate the DOA of a single source in the presence of multiple sources [21]. This has found applications in interference mitigation when estimating the DOA of a source with a known cyclostationarity, particularly in the presence of interferers that do not possess this cyclostationarity [70]. This approach is also used improve the estimate in the case of spectral overlap.

2.5 Higher-Order Statistics

Only the first- and second-order moments are typically considered in most signal processing applications. However, higher-order statistics, which are those statistics involving third-order moments and higher, have also found applications in signal processing, as signals are not completely described by their lower-order statistics. One application of higher-order statistics in signal processing is DOA estimation [12, 42]. A comprehensive description of the applications of higher-order statistics and cumulants in array processing is discussed in the series of papers by Mendel [16, 17, 23, 24, 25, 57]. One interpretation of cumulants in array processing is the phenomenon of array aperture extension, such that "virtual" array elements are formed due to the cross-cumulants, which allows for improved observability.

The nth-order moment of a random variable X is defined as shown in 2.17.

$$\mu_n = E[X^n] \tag{2.17}$$

A statistic closely related to the moments are the nth-order cumulants, which are computed through the moments and cumulants of orders less than or equal to n. This computation depends on the Bell numbers, discussed by Gardner and Spooner [20], and may be simplified in some cases, such as when the first-order statistics are zero. For example, the second-order cumulant is the variance, which may obtained by subtracting off the square of the first-order moment, the mean.

$$\kappa_2 = \mu_2 - \mu_1^2 \tag{2.18}$$

These cumulants possess many useful properties, the most notable being that the sum of the cumulants of two independent random variables is the cumulant of their sums (i.e. they accumulate). This thesis focuses on the fourth-order cumulants, also referred to as kurtosis, which provide a measure of non-Gaussianity.

For time-series applications, it can be assumed that communication signals do not possess first- or third-order moments [17]. Therefore, these moments are neglected, and the cumulant operation for a time-series is described as shown in 2.19. Note that the x_i presented here are functions of time and may contain a time-lag parameter, such that $x_i = x_i(t + \tau_i)$ where $\tau_4 = 0$, although this has been disregarded below for clarity.

$$\begin{aligned}\operatorname{cum}(x_1, x_2^*, x_2^*, x_4) =& E[x_1 x_2^* x_3^* x_4] - E[x_1 x_2^*]E[x_3^* x_4] \\ &- E[x_1 x_3^*]E[x_2^* x_4] - E[x_1 x_4]E[x_2^* x_3^*]\end{aligned} \tag{2.19}$$

Since the application here involves vectors, the formulation involves the complex fourth-order cumulant matrix (also referred to as the cumulant tensor or "quadrocovariance" in some cases [6]). This is computed through the Kronecker product. The estimation of the cumulant matrix for sources with zero first- and third-order statistics, which is typically the case in communication signals, is shown in 2.20.

$$\begin{aligned}\boldsymbol{C} = \operatorname{cum}(\boldsymbol{x}_1, \boldsymbol{x}_2^H, \boldsymbol{x}_3^H, \boldsymbol{x}_4) =& E\big[(\boldsymbol{x} \otimes \boldsymbol{x}^*)(\boldsymbol{x} \otimes \boldsymbol{x}^*)^H\big] \\ &- E\big[(\boldsymbol{x} \otimes \boldsymbol{x}^*)\big] E\big[(\boldsymbol{x} \otimes \boldsymbol{x}^*)^H\big] \\ &- E\big[(\boldsymbol{x}\boldsymbol{x}^H)\big] \otimes E\big[(\boldsymbol{x}\boldsymbol{x}^H)^*\big]\end{aligned} \tag{2.20}$$

Algorithms based on higher-order statistics are robust to spatially colored noise, have found

applications in interference mitigation [35], and possess invaluable properties for array processing applications as described by Mendel [17]. It has been shown that both MUSIC [42] and ESPRIT [12] may be applied to algorithms involving higher-order statistics. The cumulants will also be used to estimate the DOA of more sources than the number of sensor elements, which is not possible with the UVS-ESPRIT algorithm based on the second-order statistics. A useful resource on higher-order spectral analysis has been made available by Swami et al. [52], which includes both a Matlab toolbox and companion text for this topic.

Chapter 3

Algorithm Formulation

In this chapter, the ESPRIT-based algorithms for selectively estimating the DOA of sources in the presence of interference with a single electromagnetic vector-sensor are formulated. First, the approach to applying the UVS-ESPRIT algorithm to non-deterministic sources, using PAM sources as an example, and the problems that arise from this are discussed. Then, it is shown how to apply the Cyclic UVS-ESPRIT algorithm to sources that possess cyclostationary properties, and how it can be used to correct deficiencies with the UVS-ESPRIT algorithm. Finally, a Cumulant-based UVS-ESPRIT algorithm is also devised which selectively estimates the DOA of sources based on the fourth-order cumulants. This approach relies on the application of independent component analysis through the JADE algorithm.

3.1 UVS-ESPRIT Applied to Non-Deterministic Sources

The ESPRIT algorithm for the single electromagnetic vector-sensor by Wong and Zoltowski [61] was originally formulated for the case of deterministic harmonic sources and exploits a time-series invariance between two uniformly sampled data sets. In this section, it is shown how this algorithm may be applied to the case of PAM digital sources.

The conditions to apply this algorithm to digital sources are listed below.

1. There must be high correlation between the data sets. Therefore, the time delta between them must be as small as possible.

2. There must be distinct phase offsets that result from the carriers. Therefore, source carrier frequencies cannot be harmonically related. That is, the carriers are neither the same, nor are they integer multiples of the other carriers, such that the time-delay results in indistinct phase offsets.

First, the need for high correlation between the data sets is discussed. As previously discussed, applying ESPRIT to the electromagnetic vector-sensor relies on a time-series invariance. Other applications of ESPRIT involving time-series are the multiple invariance approach [53] and harmonic retrieval problems [43, 46]. It is possible to estimate the DOA through the time-series invariance because of the relationship between the Poynting vector and electromagnetic field data contained within the array manifolds.

Since this relies on a time difference between the data sets, the time-lag $\tau = \Delta T$ must be sufficiently small, so that there is high correlation. Consider the case of digital sources with pulse-amplitude modulation as shown in 3.1. When τ is greater than the symbol period T_{sym}, the iid symbols will be uncorrelated. When it is very small, such that $\tau \to 0$, there will be perfect correlation.

$$\begin{aligned} R_x(t,\tau) &= E[x(t+\tau)x^*(t)] \\ &= e^{j2\pi f_c \tau} \sum_{m,n} E[b_m b_n^*] p(t - mT_{sym} + \tau) p^*(t - nT_{sym}) \\ &= \sigma_s^2 e^{j2\pi f_c \tau} \sum_{m} p(t - mT_{sym} + \tau) p^*(t - mT_{sym}) \end{aligned} \tag{3.1}$$

Which follows from the iid relationship between the symbols, b_i.

$$E[b_m b_n^*] = \begin{cases} \sigma_s^2 & \text{if } n = m \\ 0 & \text{if } n \neq m \end{cases}$$

Furthermore, when $\tau \ll T_{sym}$, it is found that $p(t - mT_{sym} + \tau) \approx p^*(t - mT_{sym})$, resulting in high correlation. The reason that there must be high correlation in the ESPRIT algorithm is so the rotational operator $\mathbf{\Phi}$ remains unitary. However, the rotational operator will be contractive or expansive, since τ cannot be identically zero.

$$\mathbf{\Phi}^* \mathbf{\Phi} = \mathbf{\Phi} \mathbf{\Phi}^* = \boldsymbol{I}$$

This may also be understood through the signal subspace described below in 3.2. When samples are taken at a different time, the power of each kth source is scaled by some β_k that is dependent on the time-lag [17].

$$\boldsymbol{R}_y = \sum_{k=1}^{K} \beta_k \sigma_k^2 \boldsymbol{e}_k \boldsymbol{e}_k^H + \sigma_w^2 \boldsymbol{I} \tag{3.2}$$

When sampling at a point in time that is close to the previous point, $\beta_k \to 1$ as $\tau \to 0$. Samples are ideally be taken as close together as possible, so it is expected that higher sampling rates will yield better performance. The performance of the algorithm is also influenced by the pulse-shaping found in PAM sources, but this is generally found be an insignificant factor if the time-lag is sufficiently small, although an error floor is observed for square pulse-shaping.

As previously stated, there are two conditions for this algorithm to be applicable to the case of non-deterministic sources. The first is high correlation between the data, and the second is that the source carriers must result in distinct phase offsets from the time-lag. The need for distinct phase offsets arises from the principles of the ESPRIT algorithm. Roy and Kailath discusses the signal subspace between two subarrays [45].

$$\boldsymbol{T}\boldsymbol{\Psi}\boldsymbol{T}^{-1} = \boldsymbol{\Phi} \tag{3.3}$$

Since $\boldsymbol{\Phi}$ is diagonal, the eigenvalues along the diagonal of $\boldsymbol{\Psi}$ will equal the diagonal elements of $\boldsymbol{\Phi}$. If the entries along the diagonal of $\boldsymbol{\Phi}$ are the same, then the eigenvalues will be the same and the eigenvectors will be linearly dependent.

Although it is required that the time-lag between the data is sufficiently large (so that there are distinct phase offsets between the source carriers) the time-lag cannot result in phase offsets that are indistinct. This is a consequence of the relationship between the time-lag and the harmonic relationship between carrier frequencies that share the same fundamental frequency.

The above is clarified with an example. If the complex harmonics have the frequencies $f_k \in \{0.2, 0.4\}$ and a time lag of $\tau = 5$ samples, the phase offsets between these carriers will be as follows.

$$\boldsymbol{\Phi} = \text{diag}(e^{j2\pi f_1 \tau}, e^{j2\pi f_2 \tau}) = \text{diag}(e^{j2\pi (1/5)5}, e^{j2\pi (2/5)5}) = \boldsymbol{I}$$

Observe that these phase offsets are are not distinct and the signal subspace will therefore contain a single eigenvector. Therefore, there must be consideration of the source carriers when estimating the DOA of the impinging sources. This may be resolved by simply setting $\tau = 1$ sample, although it may not be so simple in a practical implementation.

There is one problem that arises from applying the UVS-ESPRIT algorithm to digitally-modulated sources however. Since the carriers are modulated with data, rather than complex harmonics (i.e. unmodulated carriers), the sources have some non-negligible bandwidth B_k. If the carriers are not sufficiently spaced, then the spectral components within the main lobe may be shared between the sources within the channel. Should these spectral components overlap with the source carrier, then the performance of the estimate will degrade. It is shown in the results chapter that this is because of the time-series invariance $\boldsymbol{\Phi}$, possibly because the rotational invariance of the signal subspace depends on both the carrier and overlapping source [46]. The performance of the algorithm when this occurs can be improved with the cyclic ESPRIT approach, which is discussed in the next chapter.

To conclude, this section has shown that the ESPRIT algorithm involving a single electromagnetic vector-sensor may be applied to non-deterministic sources with PAM digital modulation under two conditions. The first condition is to set a small time-lag $\tau = \Delta T$ between the time-shifted data sets, such that there is high correlation between them. The second condition requires that the time-lag results in distinct phase offsets. With some time-lags, the phase offsets may not be distinct if source carriers are harmonically related.

3.2 Cyclostationarity-based UVS-ESPRIT

The first approach to selectively estimating the source DOA in the presence of interference is through the cyclostationary statistics. The advantage of this approach is the reliance on second-order statistics and that many modern digital communications signals possess cyclostationarity, so it can be readily applied to most sources [37]. It can also be found that the UVS-ESPRIT algorithm discussed in the previous section that has been adapted to non-deterministic sources performs poorly when estimating the DOA of sources that spectrally overlap. The overlapping signals may be distinguished by their cyclostationary properties, however. By exploiting this cyclostationarity, the time-series invariance can be changed and the source DOA can be selectively estimated.

First, the signal models presented in chapter 2 are considered and cyclic autocorrelation matrices are computed. Let the matrix $\boldsymbol{R}_y^\alpha$ denote the received signal cyclic autocorrelation matrix and $\boldsymbol{R}_s^\alpha$ denote the source data cyclic autocorrelation matrix. The cyclic autocorrelation of the AWGN can be neglected, since it is not cyclostationary [19, 70].

$$\boldsymbol{R}_y^\alpha = \boldsymbol{A}(\boldsymbol{\psi})\boldsymbol{R}_s^\alpha \boldsymbol{A}^H(\boldsymbol{\psi}) \tag{3.4}$$

For the signal model with interferers, the matrix $\boldsymbol{R}_i^\alpha$ denotes cyclic autocorrelation of the interferers.

$$\boldsymbol{R}_y^\alpha = \boldsymbol{A}(\boldsymbol{\psi}_{soi})\boldsymbol{R}_s^\alpha \boldsymbol{A}^H(\boldsymbol{\psi}_{soi}) + \boldsymbol{A}(\boldsymbol{\psi}_{int})\boldsymbol{R}_i^\alpha \boldsymbol{A}^H(\boldsymbol{\psi}_{int}) \tag{3.5}$$

When interferers are present and there are $K+L$ total sources. The K largest eigenvalues of the eigendecomposition for the matrix $\boldsymbol{R}_y^\alpha$ will then correspond to the signal subspace of the

sources with the cycle frequency α. For the case of finite discrete samples, the eigenvalues $\{\lambda_{K+1}, \ldots, \lambda_{K+L}\}$ tend to zero as N becomes large.

$$\boldsymbol{R}_y^\alpha = \sum_{k=1}^{K} \lambda_k \boldsymbol{e}_k \boldsymbol{e}_k^H$$

It can be seen that α is a parameter that controls how the data are correlated. For example, if α is set so that the elements of $\boldsymbol{R}_i^\alpha$ tend to zero, then the sources contained within the signal subspace of $\boldsymbol{R}_s^\alpha$ can be selectively estimated.

Consider the PAM signal described by 3.1. For a small time delay between the data, it can be found that there is still high correlation as shown in the previous section. However, there is some degradation in the performance in comparison, since the signal component for that cycle frequency does not contain the full signal power [37].

As described previously, the UVS-ESPRIT algorithm relies on a time-series invariance through the time-lag. A time-series invariance can be obtained with the cyclic autocorrelation for an arbitary PAM source as shown in 3.6. The parameter T_0 denotes the period of the time-averaging operation of the cyclic autocorrelation.

$$
\begin{aligned}
R_x^{\alpha}(\tau) &= \langle R_x(t,\tau)e^{-j2\pi\alpha t}\rangle \\
&= \langle \sigma_s^2 e^{j2\pi(f_c+\alpha)\tau} \sum_m p(t-mT_{sym}+\tau/2)p^*(t-mT_{sym}-\tau/2)e^{-j2\pi\alpha t}\rangle \\
&= \lim_{T_0\to\infty} \frac{1}{T_0}\int_{-T_0/2}^{T_0/2} \sigma_s^2 e^{j2\pi(f_c+\alpha)\tau} \sum_m p(t-mT_{sym}+\tau/2)p^*(t-mT_{sym}-\tau/2)e^{-j2\pi\alpha t}dt \\
&= \sigma_s^2 e^{j2\pi(f_c+\alpha)\tau} \lim_{T_0\to\infty} \frac{1}{T_0}\int_{-T_0/2}^{T_0/2} \sum_m p(t-mT_{sym}+\tau/2)p^*(t-mT_{sym}-\tau/2)e^{-j2\pi\alpha t}dt \\
&= \sigma_s^2 e^{j2\pi(f_c+\alpha)\tau} \langle \sum_m p(t-mT_{sym}+\tau/2)p^*(t-mT_{sym}-\tau/2)e^{-j2\pi\alpha t}\rangle
\end{aligned}
\tag{3.6}
$$

The time-lag results in the time-series invariance $\Phi_k = e^{j2\pi(f_k+\alpha)}$ which can be applied to the UVS-ESPRIT algorithm through the same conditions discussed in the previous sections. The time-series invariance differs due to the cycle frequency α, however, and now depends on both the carrier frequency and cycle frequency. Sources with the same carrier frequency, but different cycle frequencies, will then have distinct phase offsets due to the time-lag.

Applications involving the Cyclic ESPRIT algorithm can either estimate the cycle frequencies of the data if the source cycle frequencies are unknown or directly specify them (i.e. they are known *a priori*) to compute the cyclic correlation matrix [37]. With a PAM digital source that has raised-cosine pulse shaping, it is known that the largest nonzero cycle frequencies occur when $\alpha \in \{-1/T_{sym}, 0, 1/T_{sym}\}$ as discussed by Napolitano [37]. For example, the cyclic correlogram for a signal with raised-cosine pulse shaping is presented in Figure 3.1 and large peaks are observed at the corresponding cycle frequencies. Therefore, DOA estimates applying cyclic ESPRIT for digital sources with raised-cosine pulses require an estimate of the cyclic autocorrelation for $\alpha = \pm 1/T_{sym}$.

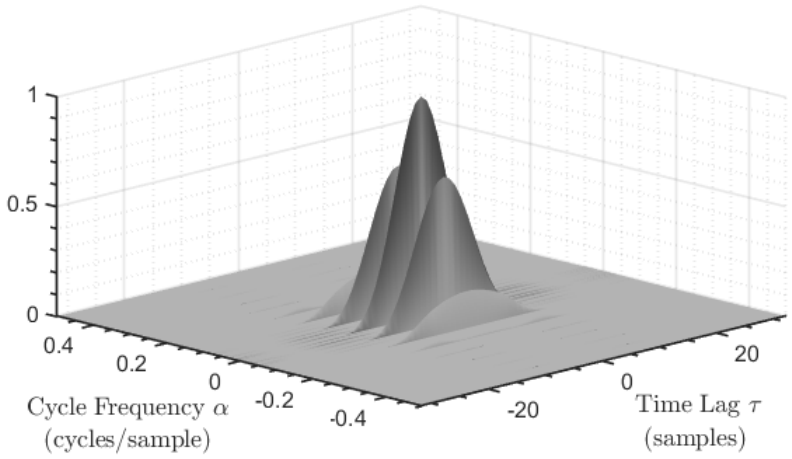

Figure 3.1: Cylic correlogram for a PAM digital signal with raised-cosine pulse shaping and $T_{sym} = 16$ samples.

When the carrier frequencies of all the sources are included, the rotation operator will be such that $\boldsymbol{\Phi} = \text{diag}(e^{j2\pi(f_1+\alpha)\tau}, \ldots, e^{j2\pi(f_K+\alpha)\tau})$. Where f_k are the carrier frequencies of the kth signal-of-interest. The sources that have the selected cycle frequency α can be estimated provided the phase-offsets are distinct.

It is now discussed how to construct the cyclic correlation matrix used in the ESPRIT algorithm. Recall that in the previous case, the correlation matrix was obtained from the $2M$-row vector formed by two data sets. A similar correlation matrix must be applied that will contain the time-series invariance between these data sets.

$$\tilde{\boldsymbol{y}}(t) = \begin{bmatrix} \boldsymbol{y}_1(t) \\ \boldsymbol{y}_2(t) \end{bmatrix} = \begin{bmatrix} \boldsymbol{y}_1(t) \\ \boldsymbol{y}_1(t-\tau) \end{bmatrix}$$

Computation of an arbitrary cyclic correlation matrix $\boldsymbol{R}_z^\alpha$ will involve cyclic cross-correlations between the rows of the data in the same manner as the correlation matrix $\boldsymbol{R}_z$. That is,

the (i,j)th elements of each $M \times M$ cyclic correlation matrix are obtained from the one-dimensional cyclic correlation function. Where $y_i(t)$ or $y_j(t)$ would be the ith or jth row of either $\boldsymbol{y}_k(t)$, where $k \in \{1,2\}$. When there are finite samples, the expectation may be estimated through the sample correlation.

$$\begin{aligned} R^{\alpha}_{z_i z_j}(\tau) &= E[z_i(t+\tau/2)z_j^*(t-\tau/2)] \\ &= E[(y_i(t+\tau/2)e^{j\pi\alpha(t+\tau/2)})(y_j(t-\tau/2)e^{-j\pi\alpha(t-\tau/2)})^*] \\ &= e^{j\pi\alpha\tau}E[(y_i(t+\tau/2)e^{j\pi\alpha(t+\tau/2)})(y_j(t-\tau/2)e^{-j\pi\alpha(t-\tau/2)})^*] \end{aligned}$$

Since the data is partitioned as $\tilde{\boldsymbol{y}}(t)$, the full cyclic correlation matrix between the time-delayed data sets $\boldsymbol{R}^{\alpha}_{\tilde{y}}$ is then a partition of the correlation matrices for various time-lags. Let the matrix $\boldsymbol{R}^{\alpha}_{ij}$ denote the cyclic correlation matrix between $\boldsymbol{y}_i(t)$ and $\boldsymbol{y}_j(t)$. The matrix $\boldsymbol{R}^{\alpha}_{\tilde{y}}$ would be obtained from a partition of $\boldsymbol{R}^{\alpha}_{ij}$, where $i,j \in \{1,2\}$.

$$\begin{aligned} \boldsymbol{R}^{\alpha}_{\tilde{y}} &= \begin{bmatrix} \boldsymbol{R}^{\alpha}_{11} & \boldsymbol{R}^{\alpha}_{12} \\ \boldsymbol{R}^{\alpha}_{21} & \boldsymbol{R}^{\alpha}_{22} \end{bmatrix} \\ &= \begin{bmatrix} E[\boldsymbol{y}_1(t)\boldsymbol{y}_1^H(t)] & E[\boldsymbol{y}_1(t)\boldsymbol{y}_2^H(t)] \\ E[\boldsymbol{y}_2(t)\boldsymbol{y}_1^H(t)] & E[\boldsymbol{y}_2(t)\boldsymbol{y}_2^H(t)] \end{bmatrix} \\ &= \begin{bmatrix} \langle \boldsymbol{y}(t)\boldsymbol{y}^H(t)e^{j2\pi t}\rangle & \langle \boldsymbol{y}(t)\boldsymbol{y}^H(t-\tau)e^{j2\pi t}\rangle \\ \langle \boldsymbol{y}(t-\tau)\boldsymbol{y}^H(t)e^{j2\pi t}\rangle & \langle \boldsymbol{y}(t-\tau)\boldsymbol{y}^H(t-\tau)e^{j2\pi t}\rangle \end{bmatrix} \end{aligned}$$

The Cyclic UVS-ESPRIT algorithm then proceeds as in the case of the UVS-ESPRIT algorithm for digital or harmonic sources. The difference is that K is the total number of sources with the selected cycle frequencies, which are the signals-of-interest, rather than the total number of sources present. That is, the eigenvectors corresponding to the K largest eigenvalues would be selected, even though $K + L$ sources are present.

Cyclostationarity has several applications in DOA estimation. Consider a cognitive radio, where a primary and secondary user are sharing a band of the frequency spectrum [28]. Source cyclostationarity may be exploited, such as through the introduction of a cyclostationary signature, which is the practice of embedding cyclic statistics in an OFDM source to provide control information to the receiver of a cognitive radio [49, 50]. This could potentially be exploited in DOA estimation to selectively estimate the source DOA of a primary or secondary user when the frequency spectrum is being shared.

This concludes the description of the Cyclic UVS-ESPRIT algorithm. The greatest advantage of this method is that it selectively-estimates the source DOA and is advantageous when there is spectral overlap from the interfering source, as this spectral overlap can degrade performance of the UVS-ESPRIT algorithm that does not exploit cyclostationarity. This is shown to outperform the ESPRIT algorithm when sources share the same carrier frequency, but different cyclostationary properties. However, performance will be worse otherwise, since the cyclic correlation operates on spectral redundancy and does not take full advantage of the total signal power.

3.3 Cumulant-based UVS-ESPRIT

This section devises an ESPRIT-based algorithm that relies exclusively on higher-order statistics for a single electromagnetic vector-sensor and is capable of selectively estimating the DOA in the presence of interference based on the higher-order statistics. The advantage of this approach over the cyclostationarity-based approach is the potential for higher performance when selectively estimating the signal-of-interest DOA, but this performance is dependant on the fourth-order statistics. Subspace algorithms based on higher-order statistics are described by Cardoso [7] and in the text by Tuncer [58]. Cumulants also provide notable benefits in array processing, such as robustness to colored noise and selective estimation of the source DOA based on higher-order statistics [16]. This is described in the series of papers by Mendel [17]. Subspace algorithms can be applied to higher-order statistics and is discussed by Nikias [12, 42].

This algorithm is based on the cumulant tensor. Although there are other formulations of the cumulant matrix, such as those presented by Mendel [2, 17, 68] and others, these were found to not be applicable to a single EMVS using the formulations attempted. It should be noted, however, that other approaches can exploit these cumulants, such as the algorithm for the electromagnetic vector-sensor described by Xu and Liu that relies on mixed-order (both second- and fourth-order) statistics [26, 66]. Different ways to formulate the cumulant matrix for ESPRIT are described by Yuen and Friedlander [68]. Additional approaches are described by Ahmed et al. [2]. These approaches exploit what is referred to as cumulant slices and do not use the full cumulant tensor. Further information on the higher-order subspace algorithms, also referred to as 2q-ESPRIT algorithms for $q > 1$, are described by Tuncer [58].

According to Cardoso, the cumulant tensor has the eigenstructure below [5, 9], where $\boldsymbol{C}_w$ is

the cumulant matrix of noise with arbitrary statistical properties and κ_k is the real-valued, positive or negative kurtosis of kth source the tensor. Therefore, the DOA estimates through subspace algorithms depend on the source kurtosis.

$$\boldsymbol{C}_y = \sum_{k=1}^{K} \kappa_k \sigma_k^4 (\boldsymbol{e}_k \boldsymbol{e}_k^H)(\boldsymbol{e}_k \boldsymbol{e}_k^H)^H + \boldsymbol{C}_w$$

To apply the cumulant UVS-ESPRIT algorithm, the data sets are first partitioned to form a $2M$-row column vector as in the UVS-ESPRIT algorithm.

$$\tilde{\boldsymbol{y}}(t) = \begin{bmatrix} \boldsymbol{y}_1(t) \\ \boldsymbol{y}_2(t) \end{bmatrix} = \begin{bmatrix} \boldsymbol{y}_1(t) \\ \boldsymbol{y}_1(t-\tau) \end{bmatrix} \approx \begin{bmatrix} \boldsymbol{A} \\ \boldsymbol{A}\boldsymbol{\Phi} \end{bmatrix} \boldsymbol{x}(t) = \boldsymbol{G}\boldsymbol{x}(t)$$

This is also described in the matrix notation below.

$$\tilde{\boldsymbol{Y}} = \begin{bmatrix} \boldsymbol{Y}_1 \\ \boldsymbol{Y}_2 \end{bmatrix} = \begin{bmatrix} \boldsymbol{A} \\ \boldsymbol{A}\boldsymbol{\Phi} \end{bmatrix} \boldsymbol{X} = \boldsymbol{G}\boldsymbol{X}$$

Recall the cumulant tensor described in section 2.5. To compute this for $\tilde{\boldsymbol{y}}(t)$.

$$\begin{aligned}
\boldsymbol{C}_{\tilde{y}} &= \mathrm{cum}(\tilde{\boldsymbol{y}}, \tilde{\boldsymbol{y}}^H, \tilde{\boldsymbol{y}}^H, \tilde{\boldsymbol{y}}) \\
&= E\big[(\tilde{\boldsymbol{y}} \otimes \tilde{\boldsymbol{y}}^*)(\tilde{\boldsymbol{y}} \otimes \tilde{\boldsymbol{y}}^*)^H\big] - E\big[(\tilde{\boldsymbol{y}} \otimes \tilde{\boldsymbol{y}}^*)\big] E\big[(\tilde{\boldsymbol{y}} \otimes \tilde{\boldsymbol{y}}^*)^H\big] - E\big[(\tilde{\boldsymbol{y}}\tilde{\boldsymbol{y}}^H)\big] \otimes E\big[(\tilde{\boldsymbol{y}}\tilde{\boldsymbol{y}}^H)^*\big] \\
&= E\big[((\boldsymbol{G}\boldsymbol{x}) \otimes (\boldsymbol{G}\boldsymbol{x})^*)((\boldsymbol{G}\boldsymbol{x}) \otimes (\boldsymbol{G}\boldsymbol{x})^*)^H\big] - E\big[((\boldsymbol{G}\boldsymbol{x}) \otimes (\boldsymbol{G}\boldsymbol{x})^*)\big] E\big[((\boldsymbol{G}\boldsymbol{x}) \otimes (\boldsymbol{G}\boldsymbol{x})^*)^H\big] \\
&\quad - E\big[((\boldsymbol{G}\boldsymbol{x})(\boldsymbol{G}\boldsymbol{x})^H)\big] \otimes E\big[((\boldsymbol{G}\boldsymbol{x})(\boldsymbol{G}\boldsymbol{x})^H)^*\big]
\end{aligned}$$

The non-stochastic matrix $\boldsymbol{G}$ can be removed from the expectation. This is shown for each term using the properties of the Kronecker product.

$$E\big[((\boldsymbol{G}\boldsymbol{x})\otimes(\boldsymbol{G}\boldsymbol{x})^*)((\boldsymbol{G}\boldsymbol{x})\otimes(\boldsymbol{G}\boldsymbol{x})^*)^H\big] = (\boldsymbol{G}\otimes\boldsymbol{G}^*)E\big[(\boldsymbol{x}\otimes\boldsymbol{x}^*)(\boldsymbol{x}\otimes\boldsymbol{x}^*)^H\big](\boldsymbol{G}\otimes\boldsymbol{G}^*)^H$$

$$E\big[((\boldsymbol{G}\boldsymbol{x})\otimes(\boldsymbol{G}\boldsymbol{x})^*)\big]E\big[((\boldsymbol{G}\boldsymbol{x})\otimes(\boldsymbol{G}\boldsymbol{x})^*)^H\big] = (\boldsymbol{G}\otimes\boldsymbol{G}^*)E\big[(\boldsymbol{x}\otimes\boldsymbol{x}^*)\big]E\big[(\boldsymbol{x}\otimes\boldsymbol{x}^*)^H\big](\boldsymbol{G}\otimes\boldsymbol{G}^*)^H$$

$$\begin{aligned}E\big[((\boldsymbol{G}\boldsymbol{x})(\boldsymbol{G}\boldsymbol{x})^H)\big]\otimes E\big[((\boldsymbol{G}\boldsymbol{x})(\boldsymbol{G}\boldsymbol{x})^H)^*\big] &= \boldsymbol{G}E\big[(\boldsymbol{x}\boldsymbol{x})^H)\big]\boldsymbol{G}^H\otimes\boldsymbol{G}^*E\big[(\boldsymbol{x}\boldsymbol{x}^H)^*\big]\boldsymbol{G}^T\\ &= (\boldsymbol{G}\otimes\boldsymbol{G}^*)E\big[(\boldsymbol{x}\boldsymbol{x}^H)\big]\boldsymbol{G}^H\otimes E\big[(\boldsymbol{x}\boldsymbol{x}^H)^*\big]\boldsymbol{G}^T\\ &= (\boldsymbol{G}\otimes\boldsymbol{G}^*)E\big[(\boldsymbol{x}\boldsymbol{x}^H)\big]\otimes E\big[(\boldsymbol{x}\boldsymbol{x}^H)^*\big](\boldsymbol{G}\otimes\boldsymbol{G}^*)\end{aligned}$$

Since the matrix $(\boldsymbol{G}\otimes\boldsymbol{G}^*)$ and its Hermitian will multiply the expectation on the left and right respectively and $\boldsymbol{C}_x = \boldsymbol{C}_s$, as the product of the complex harmonic carriers and its conjugate will be identity, the result will be 3.7. The matrix of AWGN $\boldsymbol{C}_w$ becomes zero, because it is normally distributed and does not have fourth-order statistics (i.e. $\kappa_w = 0$).

$$\boldsymbol{C}_{\tilde{y}} = (\boldsymbol{G}\otimes\boldsymbol{G}^*)\boldsymbol{C}_s(\boldsymbol{G}\otimes\boldsymbol{G}^*)^H \tag{3.7}$$

Consider the simpler case without any time-delay, such the data sets are not partitioned and $\boldsymbol{y}(t) = \boldsymbol{y}_1(t)$. In this case, we would then obtain the following result for $\boldsymbol{C}_y$.

$$\boldsymbol{C}_y = (\boldsymbol{A}\otimes\boldsymbol{A}^*)\boldsymbol{C}_s(\boldsymbol{A}\otimes\boldsymbol{A}^*)^H \tag{3.8}$$

When there are interferers present, the additive property of cumulants would result in two terms. Where $\boldsymbol{C}_i$ denotes a matrix with the kurtosis of the interferers (or signals that are not of interest). The matrices $\boldsymbol{A}_s$ and $\boldsymbol{A}_i$ denote the array manifolds of the signals-of-interest and

interferers respectively. The signal subspace have eigenvalues for each source that depends on κ_k for the signals-of-interest and κ_l for the interferers. The signals-of-interest may be selectively estimated when the interferers have $|\kappa_l| \approx 0$.

$$\boldsymbol{C}_y = (\boldsymbol{A}_s \otimes \boldsymbol{A}_s^*)\boldsymbol{C}_s(\boldsymbol{A}_s \otimes \boldsymbol{A}_s^*)^H + (\boldsymbol{A}_i \otimes \boldsymbol{A}_i^*)\boldsymbol{C}_i(\boldsymbol{A}_i \otimes \boldsymbol{A}_i^*)^H \tag{3.9}$$

Reconsider the case of partitioned data sets for $\tilde{\boldsymbol{y}}(t)$. Let $\boldsymbol{G} = \bar{\boldsymbol{A}}\bar{\boldsymbol{\Phi}}\bar{\boldsymbol{I}}$. Where $\boldsymbol{I}_K$ is a $K \times K$ identity matrix, $\boldsymbol{0}_{m\times n}$ is a $m \times n$ matrix of zeros, and $\bar{\boldsymbol{I}}$ is a stacked identity matrix.

$$\bar{\boldsymbol{A}} = \begin{bmatrix} \boldsymbol{A} & \boldsymbol{0}_{M\times K} \\ \boldsymbol{0}_{M\times K} & \boldsymbol{A} \end{bmatrix}, \quad \bar{\boldsymbol{\Phi}} = \begin{bmatrix} \boldsymbol{I}_K & \boldsymbol{0}_{K\times K} \\ \boldsymbol{0}_{K\times K} & \boldsymbol{\Phi} \end{bmatrix}, \quad \bar{\boldsymbol{I}} = \begin{bmatrix} \boldsymbol{I}_K \\ \boldsymbol{I}_K \end{bmatrix}$$

Where $\tilde{\boldsymbol{y}}(t) = \boldsymbol{G}\boldsymbol{x}(t) = \bar{\boldsymbol{A}}\bar{\boldsymbol{\Phi}}\bar{\boldsymbol{I}}\boldsymbol{x}(t)$. The Kronecker product $(\boldsymbol{G} \otimes \boldsymbol{G}^*)$ will then be such that

$$\begin{aligned} (\boldsymbol{G} \otimes \boldsymbol{G}^*) &= (\bar{\boldsymbol{A}}\bar{\boldsymbol{\Phi}}\bar{\boldsymbol{I}} \otimes \bar{\boldsymbol{A}}^*\bar{\boldsymbol{\Phi}}^*\bar{\boldsymbol{I}}^*) \\ &= (\bar{\boldsymbol{A}} \otimes \bar{\boldsymbol{A}}^*)(\bar{\boldsymbol{\Phi}} \otimes \bar{\boldsymbol{\Phi}}^*)(\bar{\boldsymbol{I}} \otimes \bar{\boldsymbol{I}}^*) \\ &= \tilde{\boldsymbol{A}}\tilde{\boldsymbol{\Phi}}\tilde{\boldsymbol{I}} \end{aligned}$$

Since the matrix $\bar{\boldsymbol{A}}$ is a block diagonal matrix with blocks $\boldsymbol{A}$, the matrix $\tilde{\boldsymbol{A}} = \bar{\boldsymbol{A}} \otimes \bar{\boldsymbol{A}}^*$ will then be

$$\tilde{\boldsymbol{A}} = (\bar{\boldsymbol{A}} \otimes \bar{\boldsymbol{A}}^*) = \begin{bmatrix} \boldsymbol{A} \otimes \bar{\boldsymbol{A}}^* & \boldsymbol{0}_{2M^2\times 2K^2} \\ \boldsymbol{0}_{2M^2\times 2K^2} & \boldsymbol{A} \otimes \bar{\boldsymbol{A}}^* \end{bmatrix}$$

Since the matrix $\bar{\boldsymbol{\Phi}}$ is a diagonal matrix, the matrix $\tilde{\boldsymbol{\Phi}} = \bar{\boldsymbol{\Phi}} \otimes \bar{\boldsymbol{\Phi}}^*$ will also be diagonal, such

that

$$\tilde{\boldsymbol{\Phi}} = (\bar{\boldsymbol{\Phi}} \otimes \bar{\boldsymbol{\Phi}}^*) = \begin{bmatrix} \boldsymbol{I}_K \otimes \bar{\boldsymbol{\Phi}}^* & \mathbf{0}_{2K^2 \times 2K^2} \\ \mathbf{0}_{2K^2 \times 2K^2} & \boldsymbol{\Phi} \otimes \bar{\boldsymbol{\Phi}}^* \end{bmatrix}$$

The matrix in the upper partition $\boldsymbol{I}_K \otimes \bar{\boldsymbol{\Phi}}^*$ will be comprised of K sets of diagonal elements containing the K elements in both $\boldsymbol{I} = \text{diag}(1, \ldots, 1)$ and $\boldsymbol{\Phi}^* = \text{diag}(\Phi_1^*, \ldots, \Phi_K^*)$. Furthermore, the matrix in the lower partition $\boldsymbol{\Phi} \otimes \bar{\boldsymbol{\Phi}}^*$ will also contain K sets of diagonal elements that are the products between the kth phase offset and the elements of $\boldsymbol{\Phi}^*$. That is, the kth diagonal matrix will consist of $\boldsymbol{\Phi}_k = \Phi_k \boldsymbol{I} = \text{diag}(\Phi_k, \ldots, \Phi_k)$ and $\Phi_k \boldsymbol{\Phi}^* = \text{diag}(\Phi_k \Phi_1^*, \ldots, \Phi_k \Phi_K^*)$.

The time-series invariance now contains products between the phase offsets for each kth source, suggesting that the UVS-ESPRIT algorithm will now depend on a time-series invariance for multiple phase offsets. This will create a problem when there are multiple sources, especially when estimating the DOA of a large number of sources, because the crowding between the power spectrums of each source will overlap with the time-series invariances of all the sources that grow with K^2. This is shown to be an issue later, although further analysis of this problem or a different approach may resolve it.

Since the elements of matrix $\bar{\boldsymbol{I}}$ are all real, the equality $\bar{\boldsymbol{I}}^* = \bar{\boldsymbol{I}}$ will be true. Therefore, the upper and lower partitions of the Kronecker product $\tilde{\boldsymbol{I}} = \bar{\boldsymbol{I}} \otimes \bar{\boldsymbol{I}}^* = \bar{\boldsymbol{I}} \otimes \bar{\boldsymbol{I}}$ will be the same. Both $\bar{\boldsymbol{A}}$ and $\bar{\boldsymbol{\Phi}}$ are block diagonal matrices, therefore the upper and lower partitions of the matrix $\boldsymbol{C}_{\tilde{y}}$ will contain the same signal subspace. We can then apply the UVS-ESPRIT algorithm by selecting the upper and lower partitions of the cumulant tensor.

However, a problem arises when estimating the array manifold matrix with the signal subspace eigenvectors. Rather than directly estimating the array manifold matrix $\boldsymbol{A}$, this ap-

proach will estimate the product $(\boldsymbol{A} \otimes \bar{\boldsymbol{A}}^*)\boldsymbol{U}$, where $\boldsymbol{U}$ is a $2K^2 \times K$ dimensional mapping. This has been described in 3.10 for clarity, where $\hat{\boldsymbol{\Phi}}$ is the $K \times K$ diagonal matrix of phases that allows for coherent addition between the signal subspace eigenvectors.

$$(\boldsymbol{A} \otimes \bar{\boldsymbol{A}}^*)\boldsymbol{U} = \frac{1}{2}\left(\boldsymbol{E}_1\boldsymbol{E}_\Psi + \boldsymbol{E}_2\boldsymbol{E}_\Psi\hat{\boldsymbol{\Phi}}^*\right) \tag{3.10}$$

We cannot retrieve $(\boldsymbol{A} \otimes \bar{\boldsymbol{A}}^*)$ however, as the mapping to the signal subspace with this approach is not invertible. That is, the $K \times K$ matrix $\boldsymbol{T}$ in the relationship between the signal subspace and array manifold $\boldsymbol{E} = \boldsymbol{A}\boldsymbol{T}$ is now singular, because of the mapping to a lower-dimensional space $\boldsymbol{E} = (\boldsymbol{A} \otimes \bar{\boldsymbol{A}}^*)\boldsymbol{U}$. Even if the matrix $(\boldsymbol{A} \otimes \bar{\boldsymbol{A}}^*)$ could be recovered, the Kronecker product between the array manifolds must be decomposed.

However, the array manifold matrix can be obtained by unfolding the matrix and treating the result as a blind source separation problem. The DOA can therefore be recovered by unfolding the $2M^2 \times K$ dimensional matrix in 3.10 into a $M \times 2MK$ matrix, then applying independent component analysis on the new data matrix. Independent component analysis is also a known approach towards Kronecker product decomposition [14] and has other other applications in DOA estimation as well [8, 47].

The columns of the matrix in 3.10 may also be selected and independent component analysis for a single component may be applied, since each column is expected to contain the signal subspace of a single source. This approach can be used to estimate the DOA of a large number of sources.

This is presented mathematically. Shown in 3.11, the goal is to estimate $\boldsymbol{A}$ through independent component analysis, $\boldsymbol{\Gamma}$ is the $M \times 2MK$ reshaped matrix, and $\boldsymbol{Z}$ is the $K \times 2MK^2$ matrix related to the mixing of the retrieved $\boldsymbol{A}$ matrix.

$$\boldsymbol{\Gamma} = \boldsymbol{AZ} \tag{3.11}$$

This application relies on the JADE algorithm by Cardoso [8]. The array manifold vectors used in the DOA estimation problem may be recovered through the operation $\mathcal{L}_{JADE}(\cdot)$, denoting the application of independent component analysis. The recovered $\hat{\boldsymbol{A}}$ would be the mixing matrix obtained through independent component analysis.

$$\hat{\boldsymbol{A}} = \mathcal{L}_{JADE}(\boldsymbol{\Gamma}) \tag{3.12}$$

The DOA estimates are obtained from the array manifold matrix. This approach is supported in the next chapter with simulation results, as the algorithm achieves the CRLB at some SNR for sources with high kurtosis depending on the spectral overlap of the sources. It is also found that this algorithm can estimate the DOA of more sources than sensor elements, although there are limitations.

To summarize, this section has shown that higher-order statistics may be applied to the DOA estimation problem involving a single vector-sensor through the cumulant tensor. This creates the problem of recovering the array manifold from a non-invertible transformation of the Kronecker product, but the application of independent component analysis can be used to recover the array manifold matrix. Further analysis of this approach may resolve the problems that arise from it, such as the dependence on multiple phase offsets.

3.4 Electromagnetic Vector-Sensor Observability

This section describes factors that influence the observability of the electromagnetic vector-sensor, which relates to the number of resolvable source DOAs. It is possible to estimate the DOA of a larger number of sources than sensor elements through the higher-order statistics. This is described in further detail by Mendel and Cardoso [6, 17].

The co-location of the sensor elements in the vector-sensor allows the estimation of a larger number of sources than an array with spatially displaced elements. In theory, a sensor with co-located elements is able to resolve the DOA of up to $M^2 - 1$ sources, whereas for spatially displaced arrays this reduces to $M^2 - M$. For electromagnetic vector-sensors however, redundancies between the electric and magnetic field data prevent a large number of sources from being estimated, due to linear dependence between the array manifold vectors. This issue is discussed by Nehorai, who states that for every five steering vectors, one of those steering vectors will be linearly dependent regardless of its DOA [30, 31, 33]. The DOA estimation of a large number of sources is limited by the linear dependence between between the array manifold vectors. Therefore, the theoretical limit of $M^2 - 1$ sources may not be achievable in practice. For example, if two sources came from the same direction, then these sources could only be distinguished by the polarization parameters, but not by the spatial parameters.

Through the higher-order statistics, it is possible to estimate the DOA of a larger number of sources than sensor elements. This is possible, because the dimensionality of the signal subspace will increase beyond the number of sensor elements [9]. This is understood through the concept of array aperture extension, which is an interpretation of the fourth-order cumulants that increase the observability of the array [17]. However, the cumulants will result in redundant array manifolds and limit the total number of resolvable source DOAs. This

problem is described by Wong for an electromagnetic vector-sensor array [65].

Another factor that should be taken into consideration are the cumulant slices, in contrast with the full cumulant tensor. This is discussed by Lie et al., who finds that the performance of algorithms relying exclusively on fourth-order DOA estimates is worsened when only using slices of the cumulant tensor [34]. Since it is desirable to take full advantage of the cumulant tensor, the approach applying fourth-order statistics only is taken for this algorithm described in this thesis.

A disadvantage of relying on the higher-order statistics for DOA estimation is that the DOA estimates are sensitive to the kurtosis of the sources, as well as the source power. This may be used to our advantage if the signal-of-interest has high kurtosis, which depends on the pulse-shaping and digital constellations. Further discussion on this is provided by Swami and Sadler [51], who present the theoretical higher-order statistics of the constellations for various digital modulation schemes. Further discussion by Ochiai addresses the role of pulse-shaping in higher-order statistics for linearly modulated digital communications schemes [41]. In general, pulse shapes with tails will perform worse due to the lower kurtosis of the statistical distribution, which are generally more bandwidth-efficient [44]. Square pulse shaping is found to be optimal due to the absence of tails, yet is not a bandwidth-efficient pulse shape.

To summarize this section, the literature shows that the number of resolvable source DOAs can go beyond the number of sensor elements through the application of higher-order statistics, but in practice appears to be limited by the linear dependence of the array manifold vectors. Furthermore, relying on the fourth-order statistics is not necessarily optimal and performance will depend on the statistical properties of the signal-of-interest.

Chapter 4

Results and Discussion

This chapter presents and discusses simulation results for the algorithms discussed in previous chapters after remarking on how simulations are performed. First, the performance of the algorithms are evaluated when there no interferers, with consideration for the polarization parameters. Then, the signal-selective capabilities of the cyclostationarity- and cumulant-based UVS-ESPRIT algorithms are evaluated when there is interference. The effect of spectral overlap on performance will then be demonstrated for each algorithm and it will be shown that the cyclic UVS-ESPRIT algorithm can improve the performance when this occurs. Additional results are then presented which show the impact on performance for different time-lags between the data sets and the DOA estimation of more sources then sensor elements. Finally, the chapter is concluded with a summary that compares each algorithm.

4.1 Simulation Setup

Before presenting the simulation results, details will be provided on how simulations were performed. All simulations apply the Monte Carlo method by running over a number of trials T and providing the average results in terms of the RMSE. Most simulations use $N = 2048$ snapshots of data and a time-lag of $\tau = 1$ sample between the data sets for the UVS-ESPRIT algorithm. A table detailing the specific conditions during each simulation is presented in Appendix B.

Since these algorithms output an unordered set of estimates, the estimates must be ordered according to a distance metric and paired with the true parameters. It is possible to pair the DOA estimates with the sources through the carrier frequency estimates, but there are cases where sources have close or overlapping carrier frequencies, due to the interest in spectral overlap. Therefore, the distance metric used is the arc-length between the unit vectors of the estimates and the unit vectors of the true values. The estimates are paired with the true parameters according to the smallest arc-length.

Although the source DOA is fixed for some simulations, most cases sample the DOA from a distribution. The azimuth angle is sampled such that $\phi \sim \text{Unif}[0°, 360°]$ and the elevation angles are sampled such that $\theta \sim \text{Unif}[80°, 100°]$. The bounds of these distributions are selected to allow for some spatial diversity among the sources and a comparison of the azimuth against the CRLB [63], which is a function of the source elevation and polarization parameters. The azimuth CRLB is a function of the elevation and polarization parameters and fixing $\theta = 90°$ in the analytical solution of the CRLB removes the dependence on the azimuth. Although the elevation is not sampled from only $\theta = 90°$, but instead near $\theta = 90°$, the CRLB is still believed to provide meaningful information and is further discussed in section 2.3.

The bounds of the elevation are chosen according to the impact that estimates may have on the RMSE. Variance in estimates of the azimuth when the source elevation is near the poles of the z-axis are greater than when the elevation is tangent to xy-plane due to a mapping between arc-length and the azimuth angle near the poles in the spherical coordinate system. This can be understood through the differential solid angle and is a result from calculus [56]. For a fixed $d\Omega$, high variation among the azimuth estimate will occur near the poles, as $\sin\theta \to 0$.

$$d\Omega = \sin\theta d\theta d\phi \implies d\phi = \frac{d\Omega}{\sin\theta d\theta}$$

Allowing for greater deviations in the azimuth with a constrained elevation also allows for a more realistic simulation, although it limits the source spatial diversity [31]. It is assumed that there is more interest in applications involving lateral movement, where the source elevation has less variability relative to the azimuth. There are applications where the elevation may be more relevant however, such as those involving aircraft. For example, one application of the electromagnetic vector-sensor applies the device to an aircraft [4].

There is also consideration of the source polarization parameters. The polarization parameters influence the linear independence of the array manifold vectors as discussed by Nehorai [31]. For example, there will be greater linear dependence between two linearly polarized sources, than two sources with both linear and circular polarization. Except for the cases where the polarization used in the simulation has been specified beforehand, two scenarios are applied. The first scenario applies diverse polarization, where the polarization parameters are fixed such that there are three linearly polarized sources and two circularly polarized sources. More specifically, the polarization phase angles are fixed as $\boldsymbol{\gamma} = [0°, 45°, 90°, 45°, 45°]$ and the polarization phase differences are fixed as $\boldsymbol{\eta} = [0°, 90°, 0°, -90°, 0°]$. In addition,

there is also consideration of the scenario where the sources are linearly polarized and have a random polarization phase angle. In this case, the polarization phase angle is sampled such that $\gamma \sim \text{Unif}[0°, 90°]$ and the polarization phase difference is fixed, such that $\boldsymbol{\eta} = \mathbf{0}$. Further information on polarization and polarization-sensitive arrays are described by DeSchamps [15] and Hatke [27].

As discussed in 3.1, the performance will degrade when the power spectra of sources overlap. The phrase "spectral overlap" is used repeatedly and refers to the situation where there are spectral components in the main lobe of one signal overlapping with the carrier of another signal. In general, the side-lobes of the sources are always overlapping with the carrier frequencies of other sources. However, this will have little effect on the performance unless there are a large number of sources present and the aggregate spectral overlap due to crowding among the sources in the power spectrum is substantial. Furthermore, if the main lobes of the sources overlap, then this will have a significant effect on the performance, even if there are few sources present. This problem is related to the time-series invariance in the ESPRIT algorithm that is determined by the carrier (or more generally, the center frequency). The degree to which this affects performance will depend on the source parameters. For example, the spatial and polarization parameters, bandwidth, carrier spacing, and relative signal power between the sources are all contributing factors.

To compare the effect that the spectral overlap will have on each algorithm, a frequency sweep is conducted, where the SNR of all sources are fixed and the carrier frequency of one source is swept over a range of frequencies. For each step in the frequency of the sweep, the performance computed is based on the average of several simulations with other parameters, such as the spatial and polarization parameters, selected at random. This simulation is intended to be an analog to the SNR sweep, since all other parameters besides the carrier frequency and SNR remain fixed. When there are multiple sources present, only one source

carrier frequency will be swept, while the other source carriers are fixed. An example of this simulation is presented in Figure 4.1 for the power spectrum in a single channel. In this case, three sources are present and the carriers of two sources are fixed. These simulations will be presented in section 4.3.

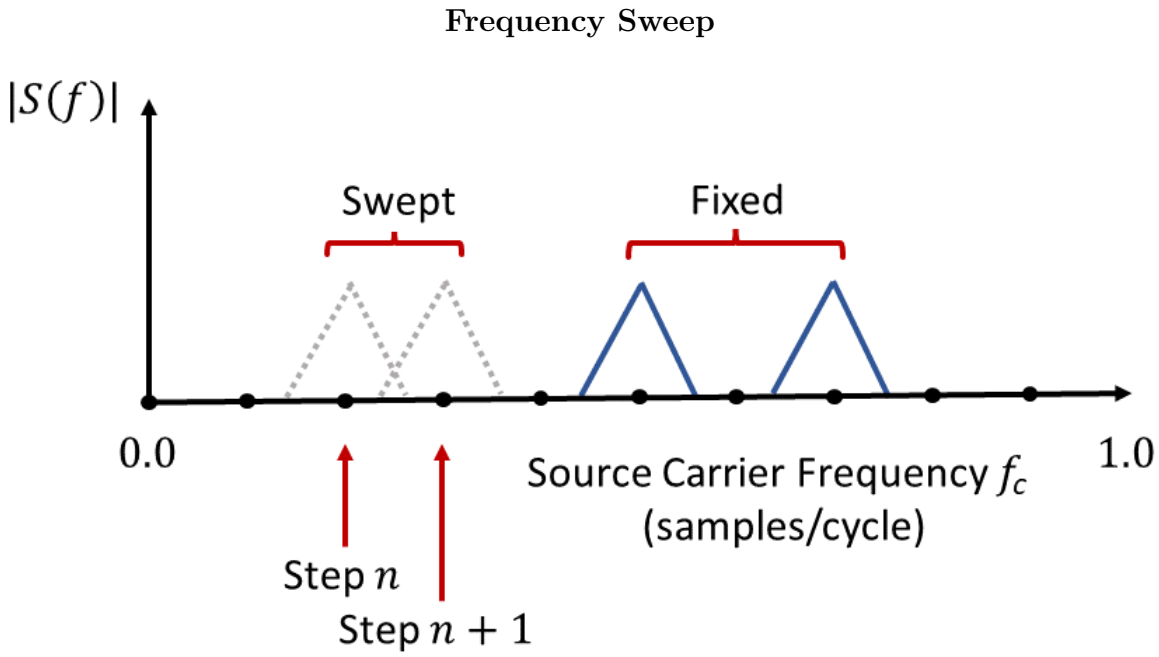

Figure 4.1: Visual representation of how the frequency sweep is performed when three sources are present. This depicts the power spectrum for a single channel, whereas the the electromagnetic vector-sensor contains six.

4.2 Algorithm Performance

4.2.1 Performance without Interference

This section presents the performance of each algorithm swept over a range of SNR where the DOA of all sources present are estimated. When interferers are present, the DOA of the signals-of-interest are selectively estimated. First, results for the original algorithm devised by Wong and Zoltowski [61] are presented, then results for the algorithms discussed in chapter 3 are presented. At the end, there will be a discussion on the differences between these algorithms and why one may be favored over another. Only the algorithms based on cyclostationarity and higher-order statistics may selectively estimate the source DOA.

UVS-ESPRIT Applied to Deterministic Harmonic Sources

Simulation results for the UVS-ESPRIT algorithm, which estimates the DOA of harmonic sources impinging upon a single electromagnetic vector-sensor, are presented. As previously discussed, ESPRIT algorithms typically estimate the DOA through the rotation operator $\mathbf{\Phi}$ obtained from spatial invariance, but this algorithm relies entirely on temporal invariance. This algorithm also unconventionally estimates of the DOA through the estimated array manifold [45] and the Poynting vector. This is discussed in further detail in section 2.2.1.

The first case presented involves diversely polarized sources, such that there are three linearly polarized sources and two circularly polarized sources. The RMSE over a range of SNR for up to five harmonic sources is presented in Figure 4.2.

The second case shows the performance for sources without polarization diversity, such that all sources are linearly polarized. These results are presented in Figure 4.3. Compared to the simulation results in Figure 4.2, a degradation in the performance is observed when there

are multiple sources present due to the linear dependence of the array manifold vectors. In contrast, diverse polarization yields better performance, since the array manifold vectors are more likely to be linearly independent.

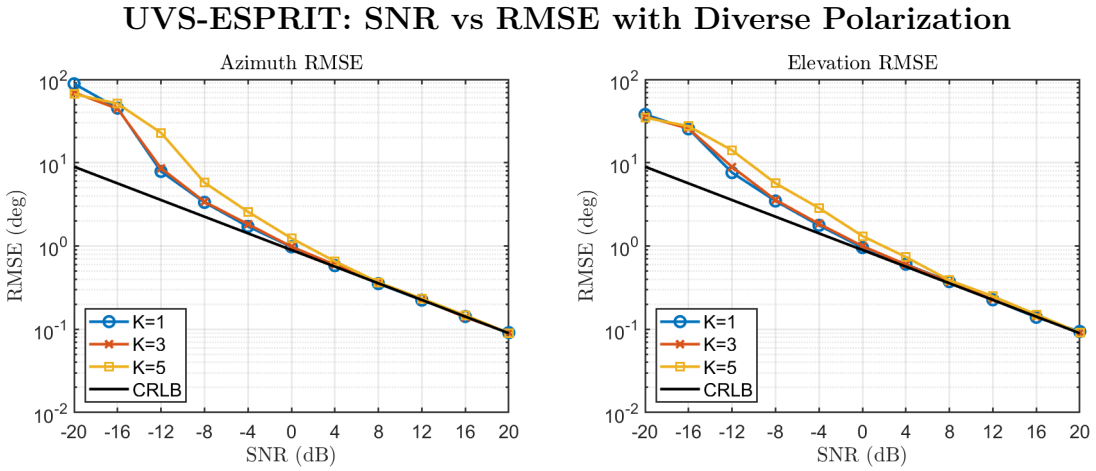

(a) Azimuth, ϕ (b) Elevation, θ

Figure 4.2: UVS-ESPRIT RMSE for up to five diversely polarized harmonic sources.

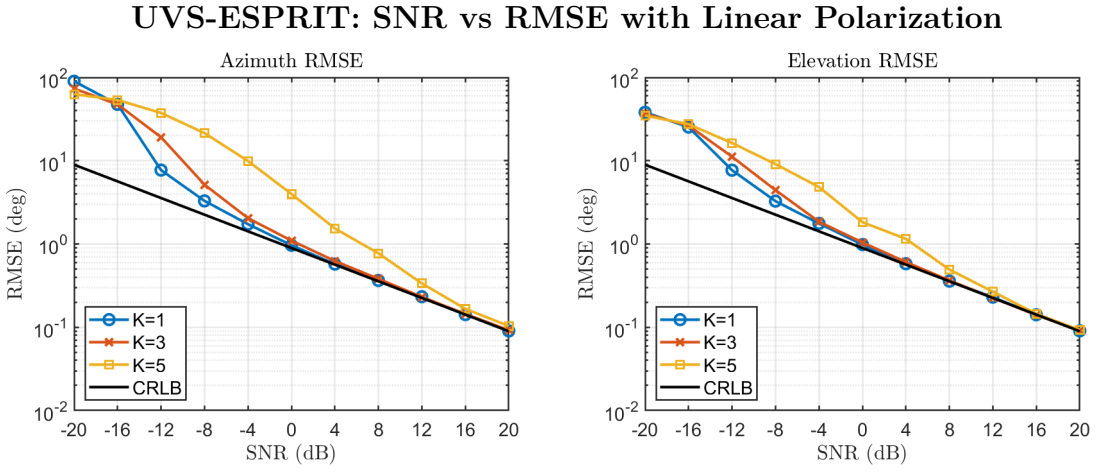

(a) Azimuth, ϕ (b) Elevation, θ

Figure 4.3: UVS-ESPRIT RMSE for up to five linearly polarized harmonic sources.

UVS-ESPRIT Applied to Non-Deterministic Sources

This section shows the performance of the UVS-ESPRIT algorithm adapted to digital sources discussed in section 3.1. Results are presented for digital sources with both pulse-amplitude modulation and multi-carrier modulation through OFDM. In these results, the same simulation conditions as the harmonic source case are maintained. For both cases, the time delta between the data sets is $\tau = 1$ sample, allowing for high correlation and distinct phase offsets. The frequency spacing between the sources for these results are shown in Figure 4.7, which show negligible spectral overlap.

First, the performance of simulations involving up to five diversely polarized PAM sources is presented. In this case, the symbol period of all sources is $T_{sym} = 64$ samples and use raised-cosine pulse-shaping with rolloff $r = 1$ and QPSK. The results of these simulations are presented in Figure 4.4. It is seen that the performance is comparable to the harmonic signal case in Figure 4.2.

In a manner similar to the case of harmonic sources, the performance when there is no polarization diversity among the sources is also presented. These results are shown in Figure 4.5. It is observed that the performance is similar to the results for harmonic sources in Figure 4.3 and marginally worse for the $K = 5$ source case. Therefore, the algorithm applied to digital sources has the same performance as when it is applied to harmonic sources.

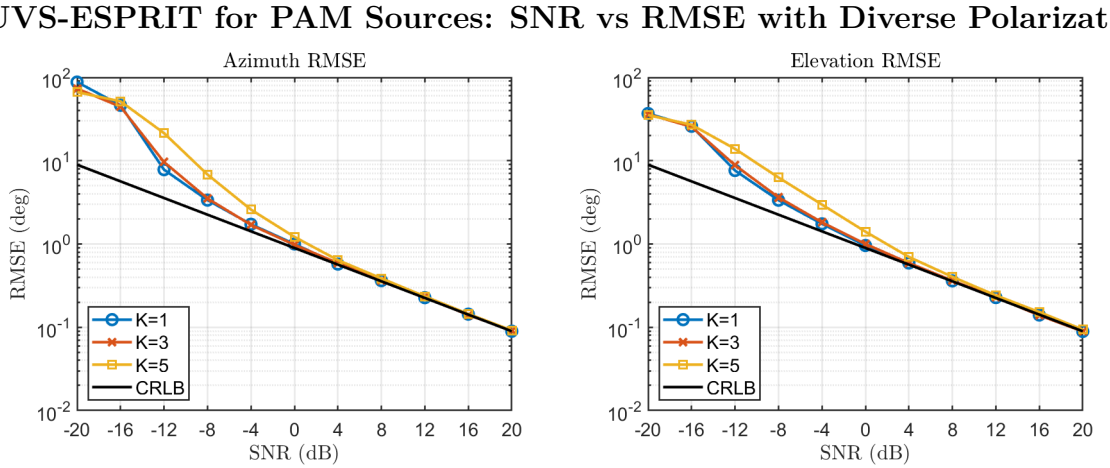

(a) Azimuth, ϕ (b) Elevation, θ

Figure 4.4: UVS-ESPRIT RMSE for up to five diversely polarized PAM digital sources with $T_{sym} = 64$.

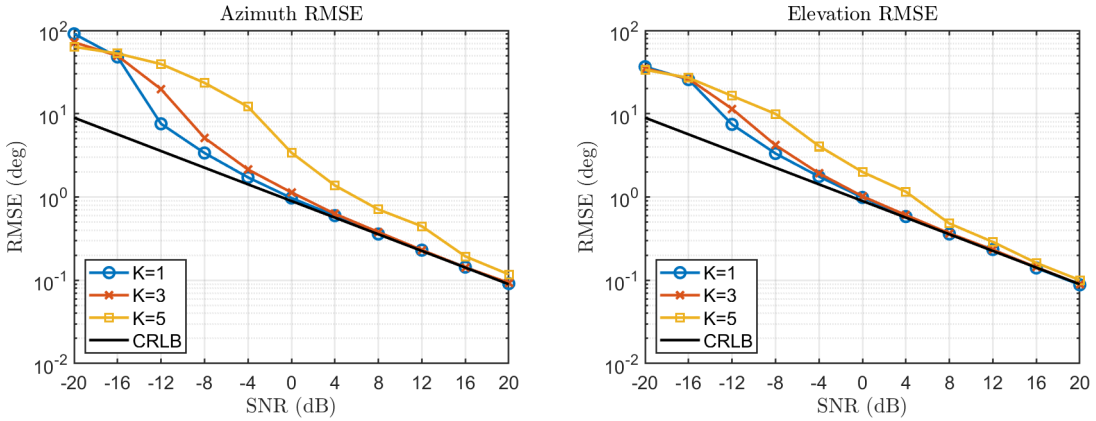

(a) Azimuth, ϕ (b) Elevation, θ

Figure 4.5: UVS-ESPRIT RMSE for up to five linearly polarized PAM digital sources with $T_{sym} = 64$.

In addition to PAM sources, consideration is given to the UVS-ESPRIT algorithm applied to OFDM sources. Interest in the performance for OFDM sources stems from its wide use in modern digital communications and the different power spectrum. This is a multi-carrier communication scheme and the original UVS-ESPRIT algorithm relies on a single harmonic carrier frequency.

For this simulation, the OFDM sources have a symbol period of $T_{sym} = 256$ samples, $N_{SC} = 10$ subcarriers, and a guard interval of $T_g = T_{sym}/4$. Although there is no pulse-shaping involved in OFDM, which affects the correlation between the data sets, there is windowing among the subcarriers. The OFDM sources here apply square windowing, but similar results are obtained for raised-cosine windowing. The results of this simulation for diversely polarized sources is presented in Figure 4.6. Performance appears similar to the case of PAM sources shown in Figure 4.4 as well as harmonic sources. There is a slightly worse performance however, which may be a consequence of the aggregate spectral overlap between the sources as K increases. The frequency spacing of the OFDM sources and the side-lobes in this simulation are presented in Figure 4.7 and compared against PAM sources. This shows the negative effect that spectral overlap may have on performance as the total number of sources increases.

Although it is not discussed, increasing the time lag beyond the symbol period of the OFDM symbol degrades the performance in a manner similar to the case of PAM digital sources. Further discussion on the time-lag and correlation are discussed later in section 4.4. Results when the OFDM sources are linearly polarized are not presented, but are found to be similar to those in Figure 4.5.

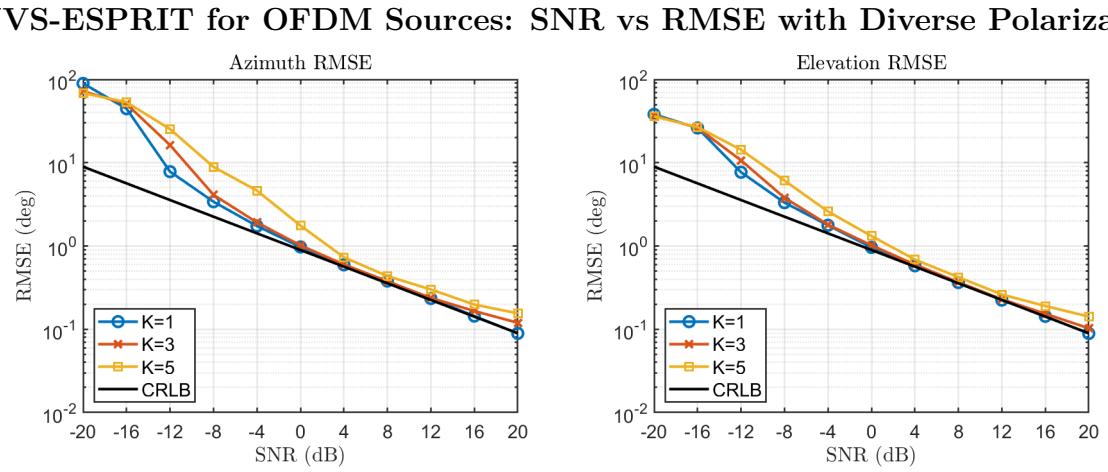

(a) Azimuth, ϕ (b) Elevation, θ

Figure 4.6: UVS-ESPRIT RMSE for up to five diversely polarized OFDM digital sources with $T_{sym} = 64$.

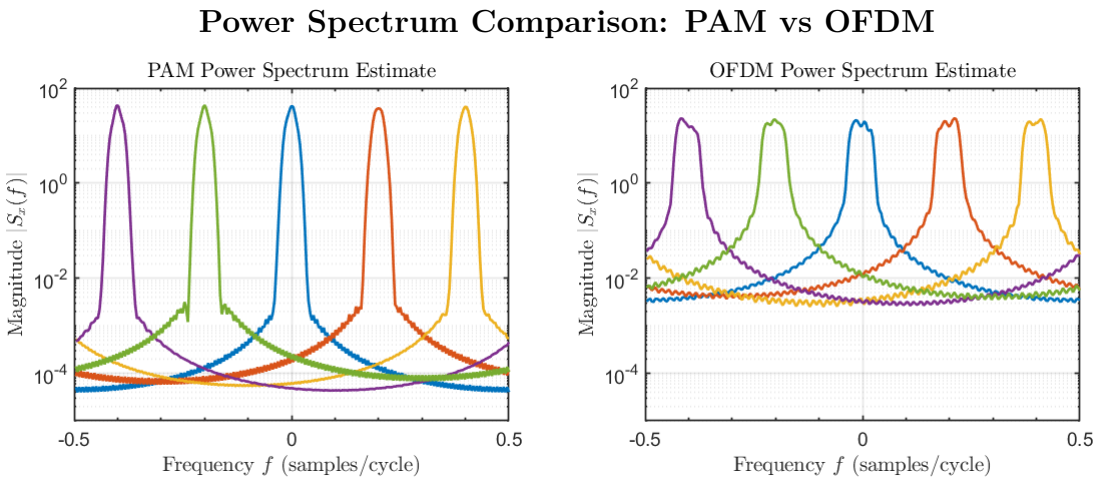

(a) PAM Sources (b) OFDM Sources

Figure 4.7: Comparison between the PAM and OFDM power spectra.

Cyclic UVS-ESPRIT

Simulation results that show the performance of the Cyclic UVS-ESPRIT algorithm discussed in section 3.2 are now presented. There is consideration for both PAM and OFDM sources, similar to the case where the UVS-ESPRIT algorithm applied to digital sources.

The performance of this algorithm is dependent on the cyclostationary properties of sources. This is a consequence of using the cyclic correlation matrix and not relying on the full signal power. This is related to the cyclic Wiener-Khinchin theorem that relates the cyclic autocorrelation and its power spectrum [21, 37]. Although these these components may be selected through the cyclic autocorrelation to selectively estimate the DOA of a source through its cycle frequencies, the full power of the signal is not used in the estimate. For example, the cyclic correlogram for a PAM source is shown in Figure 3.1, where it is seen that the full signal power is not contained within the cyclic autocorrelation at the cycle frequency $\alpha = \pm 1/T_{sym}$, yet there is nonzero correlation due to the spectral redundancy of the cyclostationary signal. Overall, the the performance may appear worse, but it is shown later that this algorithm can be used to reduce variance of estimates when there is spectral overlap through the cycle frequency. Therefore, the presentation of the performance of this algorithm is to demonstrate that the algorithm can be applied, but will not accurately depict for performance for all cases, which depends on the cyclostationary properties of the signal-of-interest.

The performance of the Cyclic UVS-ESPRIT algorithm for PAM digital sources is now evaluated. In this simulation, the sources have raised-cosine pulse shaping, symbol periods with duration $T_{sym} = 64$ samples, and a cyclic correlation matrix estimated for the cycle frequency $\alpha = 1/T_{sym}$. This cycle frequency is selected based on the raised-cosine pulse-shaping of the sources [37]. The performance of the algorithm is simulated for up to five

sources over a range of SNR as in previous simulations.

The results of these simulations for diversely polarized sources are shown in Figure 4.8. In these results the RMSE curve for each source is now above the CRLB, whereas previously the curves converged to the CRLB. This is a consequence of the cyclic correlation and not using the full signal power in the estimate. This demonstrates that the algorithm may be applied to PAM sources, but the performance may not represent a typical case.

In addition to dependence on the cyclostationary statistics, the performance for algorithms that exploit cyclostationarity will also be sensitive to the number of samples, since a large number of samples are required to reliably estimate the cyclostationary statistics [21]. Therefore, DOA estimation algorithms based on cyclostationarity generally require more samples.

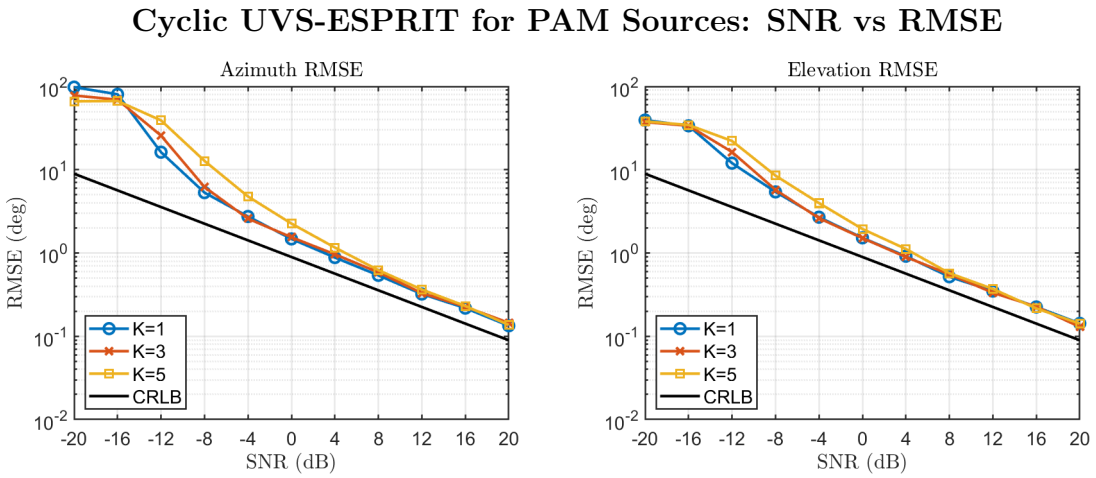

(a) Azimuth, ϕ (b) Elevation, θ

Figure 4.8: Cyclic UVS-ESPRIT RMSE for up to five diversely polarized PAM digital sources with $T_{sym} = 64$ and $\alpha = 1/T_{sym}$.

Consideration is also given to OFDM sources that possess cyclostationarity when a cyclic prefix has been appended to the signal. This is shown in Figure 4.9 and is obtained from the OFDM signal described by the signal model. The cyclic correlation for this signal model depends on the duration of the guard interval the spectral redundancy between the subcarriers. The cyclostationarity of OFDM sources is discussed in greater detail by Du [18] and Adrat [1], which take other factors into consideration, such as pilot symbols, the preamble, and variable sub-carrier power.

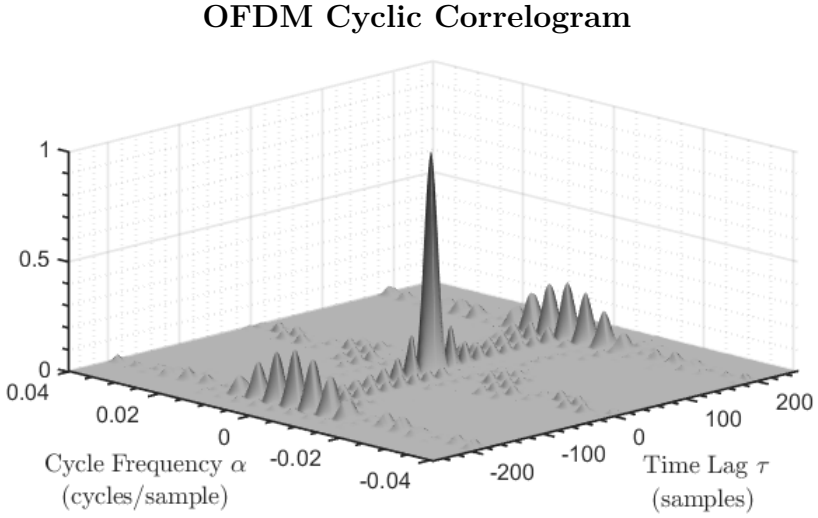

Figure 4.9: Cylic correlogram for a OFDM digital signal.

The performance of the Cyclic UVS-ESPRIT algorithm applied to a single OFDM source is shown in Figure 4.10. This performance depends on correlation between the subcarriers and performs worse than the Cyclic UVS-ESPRIT algorithm applied to PAM sources because of the difference in cyclostationary properties. Although, this approach may still be used this to selectively estimate the DOA of the OFDM source using the Cyclic UVS-ESPRIT algorithm. A performance improvement of the DOA estimate could be achieved by increasing the duration of the guard interval or by taking a larger number of samples.

Although the results have not been presented here, there was also consideration of PAM

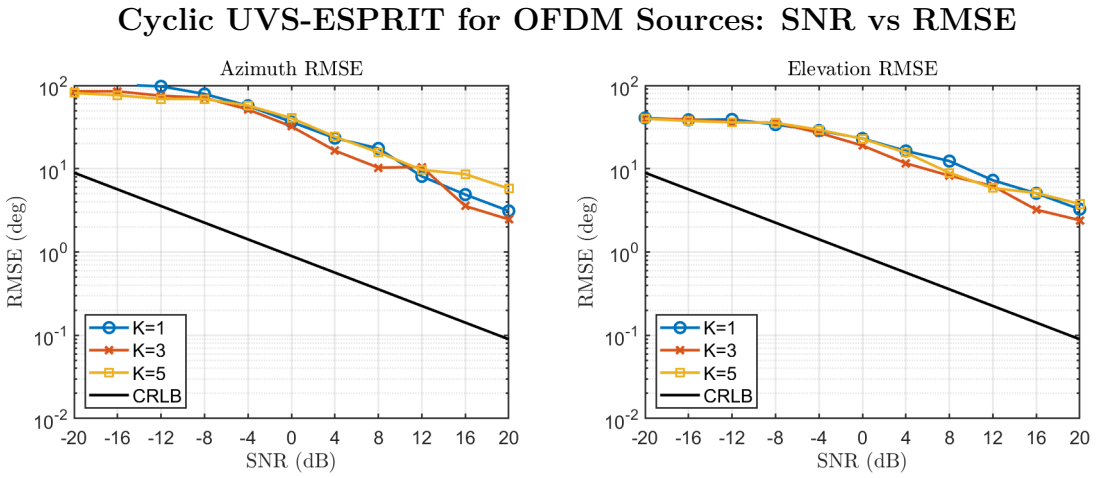

(a) Azimuth, ϕ (b) Elevation, θ

Figure 4.10: Cyclic UVS-ESPRIT RMSE for up to five diversely polarized OFDM digital sources with $N_{sc} = 10$, $T_{sym} = 256$, and $T_g = T_{sym}/4$.

sources with multi-carrier modulation. That is, two equal power PAM sources with carriers that are not necessarily orthogonal. In this case, the invariance of the sources depends on the center frequency, rather than the carrier frequencies of the sources. This occurs in spite of the absence of spectral components at that frequency.

Cumulant UVS-ESPRIT

The performance of the Cumulant UVS-ESPRIT algorithm discussed in section 3.3 is now presented for PAM sources. Results for the performance maintain the same conditions as the previous results. First, square pulse-shaping will be used with QPSK, so the kurtosis of the statistical distributions will be high. Then there will be consideration for waveforms with different pulse-shaping and digital constellations.

First, the results for the case of square pulse-shaping and QPSK for up to five diversely polarized sources is presented in Figure 4.11. While performance does achieve the CRLB for, it is poor for low SNR and there is an error floor for higher SNR when multiple sources are present. The error when the SNR is high may be attributed to issues related to the temporal correlation between time-delayed signals with square pulse-shaping. A similar error floor is observed for the UVS-ESPRIT algorithm for square pulse-shaping when cumulants are not involved. These results show optimal conditions for frequency spacing.

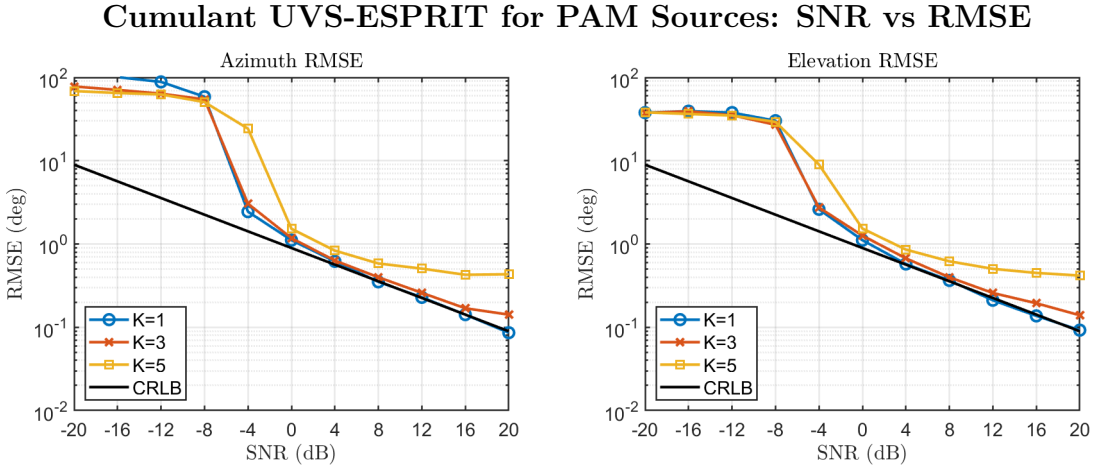

(a) Azimuth, ϕ (b) Elevation, θ

Figure 4.11: Cumulant UVS-ESPRIT RMSE for up to five diversely polarized PAM digital sources with $T_{sym} = 64$ and square pulse-shaping.

The case where there is a single source with variable fourth-order statistics is also considered. The fourth-order statistics of the waveforms that are due to pulse-shaping of the PAM sources and OFDM signals will affect the performance of the cumulant ESPRIT-based algorithm, which why it is capable of selectively estimating the source DOA, where the signals-of-interest are assumed to have higher fourth-orther statistics than the interferers. A simulation is performed for various waveforms with different fourth-order statistics, which is shown in Figure 4.12. For the square pulse-shaping, where $|\kappa| \approx 1.000$, the RMSE of the algorithm converges to the CRLB. It is seen that the performance decreases as the kurtosis of each waveform does. For example, the raised-cosine pulses have kurtosis $|\kappa| \approx 0.278$ for the rolloff $r = 0.5$ and $|\kappa| \approx 0.076$ for the rolloff $r = 1.0$, resulting in lower performance. It can be seen that OFDM, even with square-windowing, has the poorest performance with $|\kappa| \approx 0.026$.

The impact of the source kurtosis due to digital modulation schemes, such as QPSK and 16-QAM, is also considered. As discussed by Swami and Sadler [51], some constellations will have different higher-order statistics as a consequence of the Gaussianity of the statistical distributions. This is shown for QPSK and 16-QAM as shown in Figure 4.13. It can see that the QPSK performs better with higher-order statistics.

These results demonstrate how the cumulant-based ESPRIT algorithm is capable of selectively estimating the DOA of a signal-of-interest. That is, where the signals-of-interest have high kurtosis and the interferers have low kurtosis, which is a consequence of the statistical distributions of the waveforms. In this section, it was shown that this algorithm can estimate the DOA of up to five sources, but it will be shown later that it can estimate the DOA of more than that, although the ability to do this is affected by the carrier frequency spacing with the approach used in the Cumulant UVS-ESPRIT algorithm.

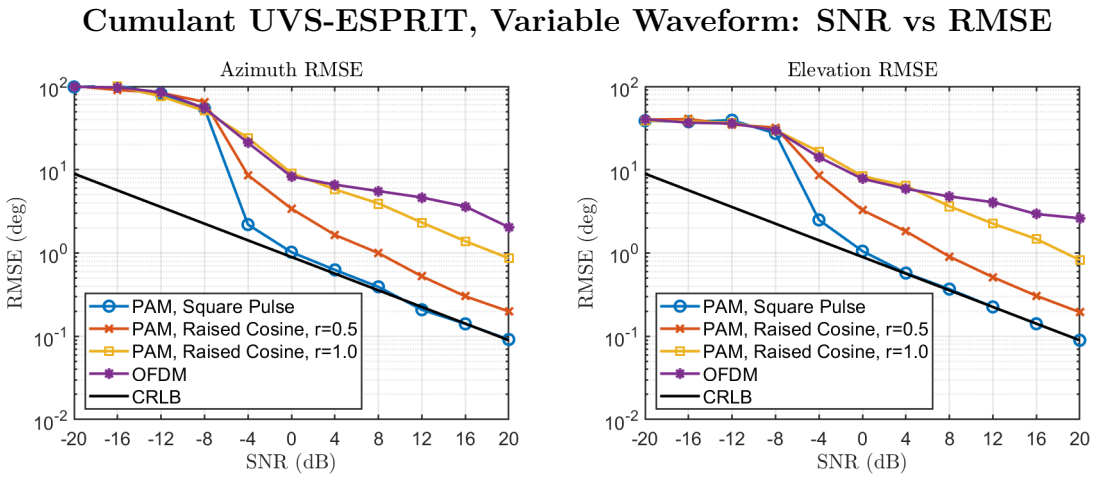

(a) Azimuth, ϕ (b) Elevation, θ

Figure 4.12: Performance of Cumulant UVS-ESPRIT with variable kurtosis due to different waveforms.

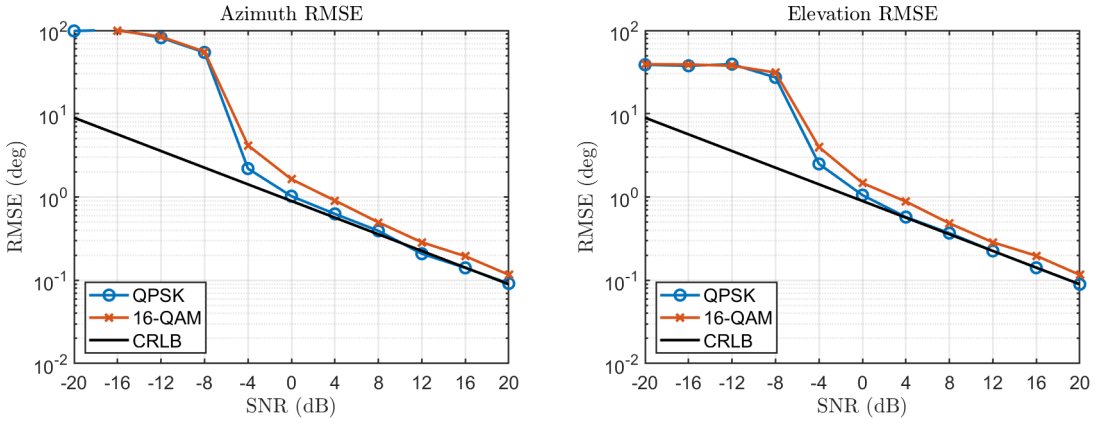

(a) Azimuth, ϕ (b) Elevation, θ

Figure 4.13: Performance of cumulant ESPRIT with variable kurtosis due to the digital constellations.

4.2.2 Performance with Interference

This section will present results showing that the Cyclic UVS-ESPRIT and Cumulant UVS-ESPRIT algorithms are capable of selectively estimating the DOA of signals-of-interest in the presence of interference. Although interference is present, the performance in this case will involve a sweep of the SNR to allow for comparisons against the previous results without interference. Both cases only consider one interferer with fixed SIR as the SNR increases. The interferer elevation is fixed to $\theta_L = 45°$ to prevent the effect of the interferer has on the spatial diversity between the signals-of-interest. Interference refers to a source that is not selectively estimated with the DOA estimation algorithm, which is defined in a previous section. The carrier frequency, polarization, and DOA of the interferer will influence how well the algorithms can selectively estimate the signal-of-interest DOA. For example, the performance would be worse if the interferer had the same carrier frequency or direction-of-arrival as a signal-of-interest, which is shown in section 4.3.

Cyclic UVS-ESPRIT

The performance of the Cyclic UVS-ESPRIT algorithm when there is an interferer present is shown for PAM digital sources, where the symbol period of the signal-of-interest will differ from the interferer. The symbol period of the $K = 2$ signals-of-interest is $T_{sym,K} = 64$ samples and the $L = 1$ interferer is $T_{sym,L} = 44$ samples. The cyclostationarity-based algorithm will selectively estimate the DOA of signals-of-interest with the cycle frequency for the signal-of-interest. Therefore, the cycle frequency is such that $\alpha = 1/T_{sym,K}$. It is shown that the DOA of multiple sources may be estimated in the presence of an interferer. The performance degrades as the SIR decreases for very high SNR. This shows that these algorithms are capable of selectively estimate the DOA of the signals-of-interest.

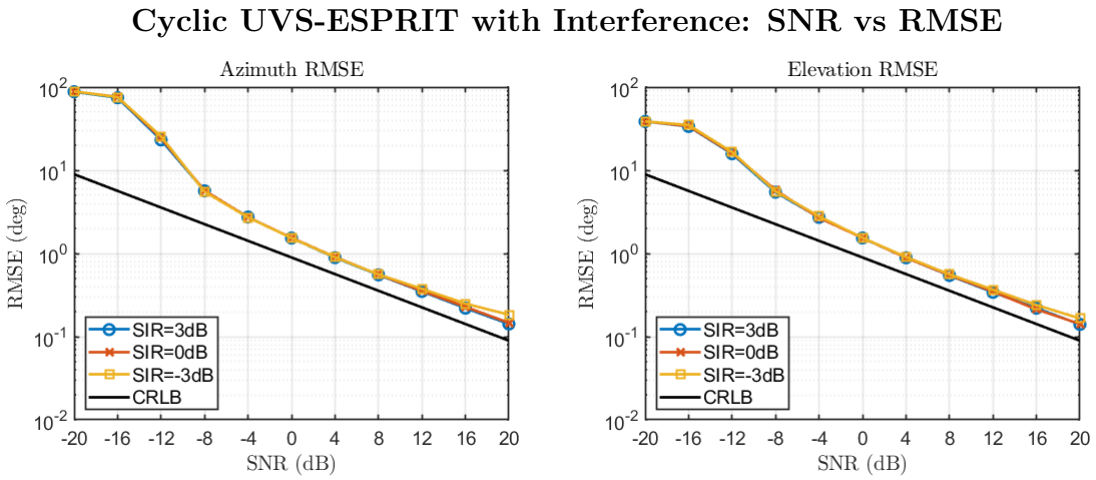

(a) Azimuth, ϕ (b) Elevation, θ

Figure 4.14: Performance of the Cyclic UVS-ESPRIT algorithm when an interferer is present.

Cumulant UVS-ESPRIT

The performance of the Cumulant UVS-ESPRIT algorithm when there is an interferer present is also considered. Since the cumulant-based algorithm estimates the DOA based on the source kurtosis, it can selectively estimate the DOA of signals-of-interest when the interferers have low kurtosis. It is shown that the DOA of multiple signals-of-interest with square pulse-shaping are selectively estimated in the presence of an interferer with raised-cosine pulse-shaping. These results are shown in Figure 4.14.

The sources with square pulse-shaping will have high kurtosis ($|\kappa_k| \approx 1$), while the interferer will have low kurtosis due to its raised-cosine pulse-shaping ($|\kappa_L| \approx 0$). The sources with square pulse-shaping can be selectively estimated. In this case, the carrier frequencies of the signals-of-interest are $f_k \in \{0.17, 0.23\}$, while the carrier of the interferer is $f_L = -0.30$. Although the signals-of-interest can be selectively estimated, it is found that there cannot be spectral overlap by the interferer with the carrier frequency of the signal-of-interest in spite of the selective estimation.

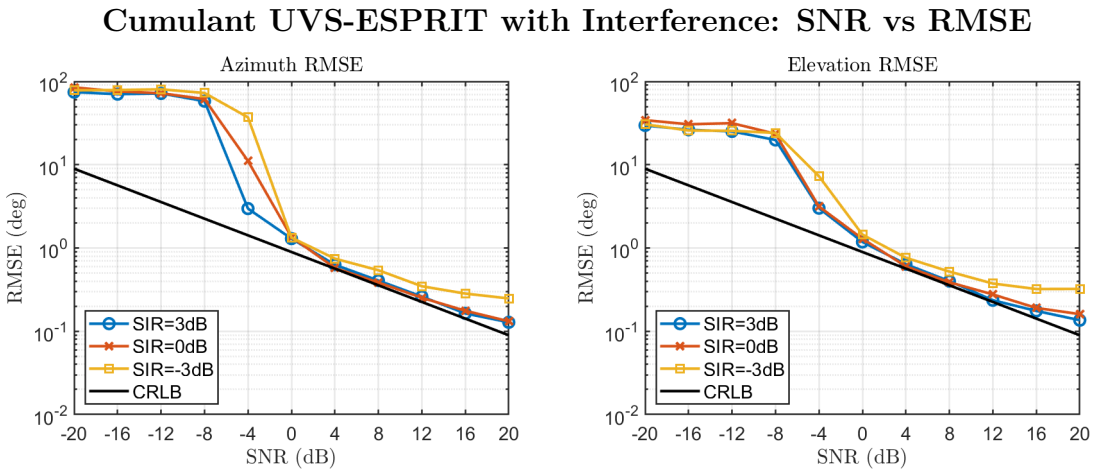

(a) Azimuth, ϕ (b) Elevation, θ

Figure 4.15: Performance of the Cumulant UVS-ESPRIT algorithm when an interferer is present.

4.2.3 Discussion

This section has presented simulation results to show the performance of the DOA estimation algorithms discussed in chapter 3. The relative performance between these algorithms is variable and depends on the statistical properties of the sources. However, the algorithms based on cyclostationarity and higher-order statistics are capable of selectively estimating the DOA in the presence of interference [17, 70] based on these statistical properties.

The algorithm based on cyclostationarity selectively estimates the DOA of sources based on the cyclostationary properties, while the algorithm based on cumulants selectively estimates sources based on kurtosis. The advantage one algorithm over another depends on the application, although the algorithm based on cyclostationarity may be preferred because it does not have problems with frequency spacing. For the approach based on cyclostationarity, the signals-of-interest must have a cycle frequency that the interferers do not. Otherwise, the signal-of-interest DOA cannot be selectively estimated. For the approach based on the fourth-order cumulants, the signals-of-interest must have a high kurtosis relative to the interferer. For the case of PAM digital sources, the signal-of-interest should have square pulse-shaping. If the interferer has square pulse-shaping however, then the signal-of-interest DOA cannot be selectively estimated. The algorithm based on cumulants has additional advantages as well, such as being robust to spatially colored noise [16, 36].

The remainder of this chapter presents performance results when there is spectral overlap between the sources. It is seen that the spectral overlap between the sources will affect the performance, depending on the algorithm and the degree of spectral overlap between the sources. A higher number of samples can be used to improve the performance when this occurs.

4.3 The Spectral Overlap Problem

In this section, the performance of the algorithms when spectral overlap occurs is discussed. This is a problem where the performance of the ESPRIT algorithm degrades due to the overlapping frequency spectra between the main lobes of the sources. The spectral overlap problem is described in further detail in section 3.1 and section 4.1.

4.3.1 Results

UVS-ESPRIT Applied to Non-Deterministic Sources

The UVS-ESPRIT algorithm for non-deterministic sources performs worse when there is spectral overlap between the sources. When encoded with digital information, the signals of the impinging sources have a non-negligible bandwidth due to pulse-shaping. This may reduce the performance of the estimator when there are multiple sources due to the overlapping power spectra of each source. A simulation to demonstrate this is conducted, which is described in section 4.1.

The results showing the RMSE for two sources, where the carrier frequency of one is fixed at $f_k = 0.20$ samples/cycle and the other is swept over a range. The impact of the overlap on the performance is seen in Figure 4.16. The estimator performs worse as the main lobe of the source overlaps with the fixed carrier frequency of the other source.

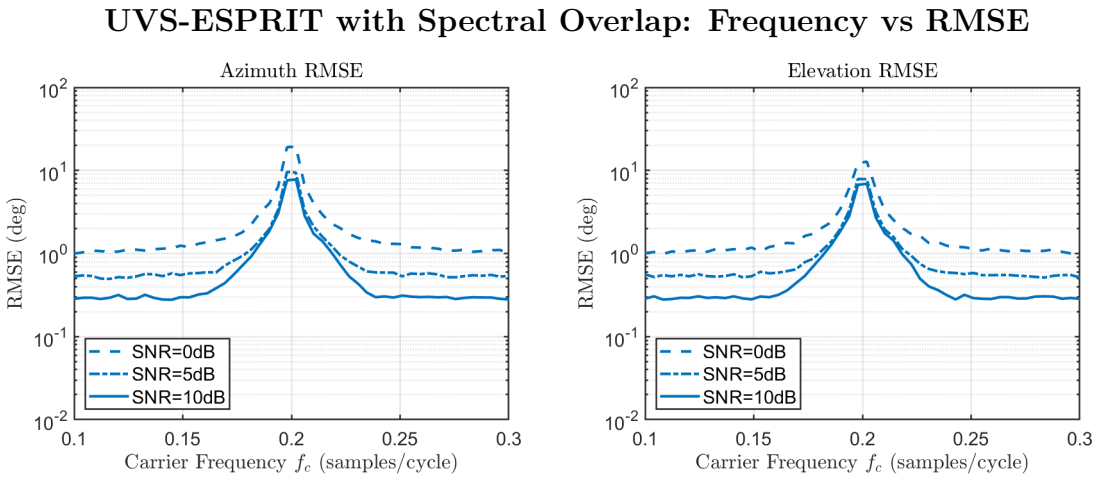

(a) Azimuth, ϕ (b) Elevation, θ

Figure 4.16: Performance of the UVS-ESPRIT algorithm when there is spectral overlap for two sources.

Cyclic UVS-ESPRIT

In this section, it is shown that the Cyclic UVS-ESPRIT algorithm presented in section 3.2 may be used to estimate the DOA of a source when there is an interferer with spectral overlap by changing the time-series invariance. First, results are shown for the case where the sources have different cycle frequencies and how the DOA of one source may be selectively estimated and the performance improved. Then it is shown that this does not occur when the cycle frequencies are the same.

Consider an interfering source that overlaps a signal-of-interest in frequency. Using the previously mentioned ESPRIT algorithm for digitally modulated sources, the DOA of a signal-of-interest may not be estimated reliably. However, the Cyclic UVS-ESPRIT algorithm makes it possible to selectively estimate its DOA and change the time-series invariance of the ESPRIT algorithm.

To show the performance of Cyclic UVS-ESPRIT in the event of spectral overlap between two sources, a simulation is performed that sweeps the carrier frequency of one source as was done previously. In this case, the symbol periods of the sources are $T_{sym} = 32$ samples and $T_{sym} = 44$ samples. The performance of the algorithm is presented in Figure 4.17. The SNR for both sources is fixed and the RMSE of the signal-of-interest estimated by the algorithm is lower when there is spectral overlap with its carrier frequency. However, it is observed that the RMSE increases when there is overlap with the frequency that has been shifted by the cycle frequency, $f + \alpha$. Therefore, this method can selectively estimate the source DOA when there is spectral overlap and improve the performance, but the performance is worse when there is no spectral overlap or when there is overlap with the frequency $f + \alpha$.

The performance of the Cyclic UVS-ESPRIT algorithm for two sources with the same cyclostationary properties is also evaluated, where $T_{sym} = 32$ samples for both sources. Although

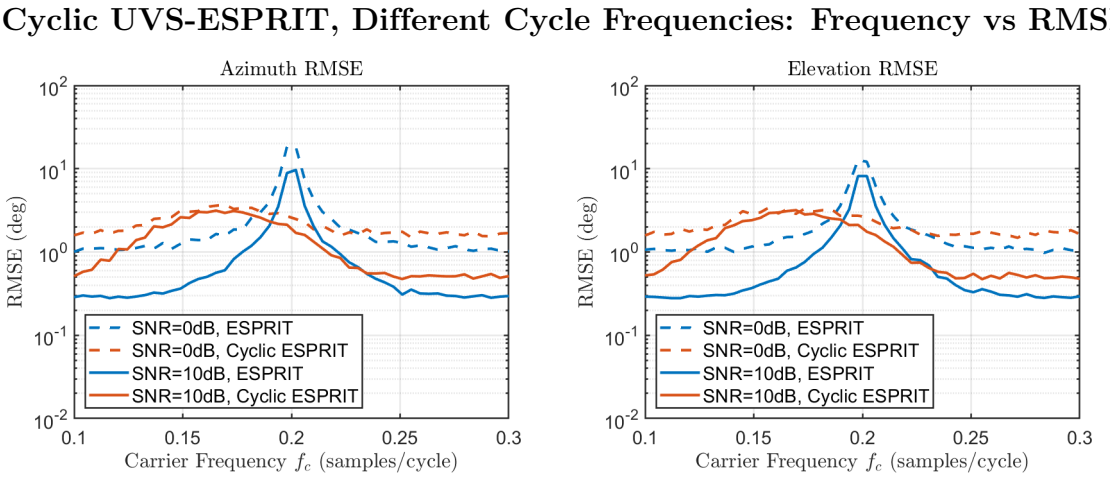

(a) Azimuth, ϕ (b) Elevation, θ

Figure 4.17: Performance of the Cyclic UVS-ESPRIT algorithm when there is spectral overlap for two sources with different cycle frequencies.

it is possible to selectively estimate the DOA of a source with the cyclic autocorrelation, the improvement in performance over the UVS-ESPRIT does not occur what if the sources have the same cycle frequency.

A simulation is also performed when the sources have the same cyclostationary properties. The DOA of the two sources are estimated and the carrier frequency of one source is swept. The results of this simulation are presented in Figure 4.18. As shown, Cyclic UVS-ESPRIT performance degrades when there is overlap with the carrier frequency, just as it did when the UVS-ESPRIT algorithm was applied to digital sources.

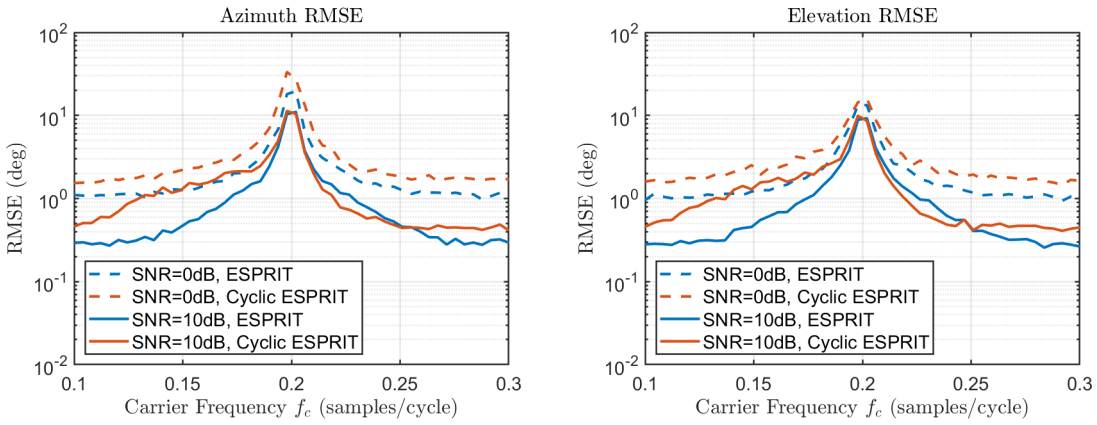

(a) Azimuth, ϕ (b) Elevation, θ

Figure 4.18: Performance of the Cyclic UVS-ESPRIT algorithm when there is spectral overlap for two sources with the same cycle frequency.

Cumulant UVS-ESPRIT

The problem of spectral overlap for the Cumulant UVS-ESPRIT algorithm is described in this section. Although the cumulants may selectively estimate the source DOA, the sources with high kurtosis still degrade performance depending on the spacing between the source carrier frequencies. It was shown that there are additional problems related to carrier spacing due to the requirement for distinct phase offsets.

In this simulations there are three sources present. The carrier frequency of one source is swept, while the others are fixed for $f_k \in \{0.20, 0.30\}$ samples/cycle. For the case of two sources, shown by the blue curve, the performance is worse when there is spectral overlap near $f_c = 0.25$ samples/cycle. This is similar to the UVS-ESPRIT algorithm for digitally modulated sources, where the performance degrades when the main lobes of the sources overlap with the carriers. It is shown that the performance is worse as the source approaches the frequencies $f_c \in \{0.10, 0.25, 0.40\}$ due to the additivity between the phase offsets described in section 3.3.

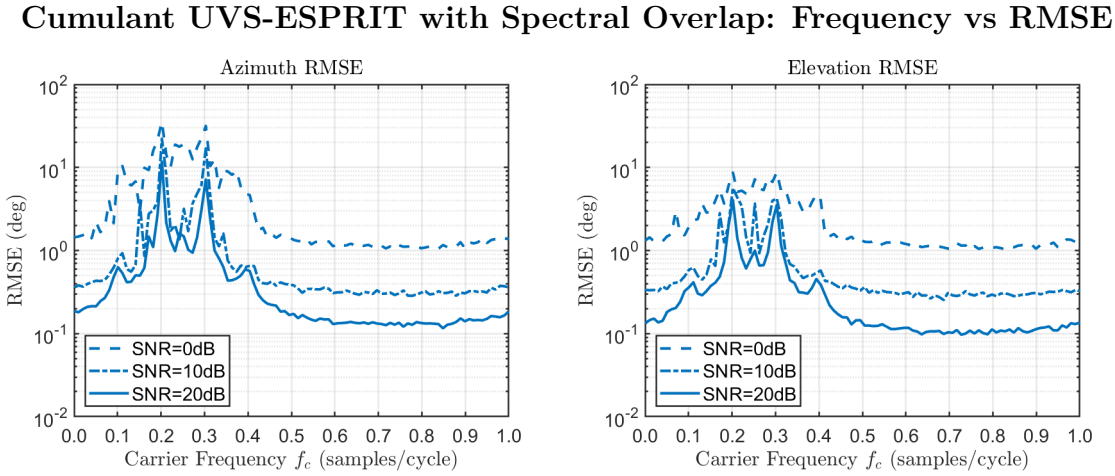

(a) Azimuth, ϕ (b) Elevation, θ

Figure 4.19: Performance of the Cumulant UVS-ESPRIT algorithm when there is spectral overlap for two sources, where $f_k \in \{0.20, 0.30\}$.

4.3.2 Discussion

This section has approached the problem of estimating the DOA of sources when there is spectral overlap, which is a consequence of the time-series invariance discussed in section 3.1 and the signal subspace. It is shown that selectively estimating the DOA of sources does not resolve the problem of spectral overlap between sources. Although the cyclic correlation can be used to improve the performance when this occurs, because it changes the time-series invariance of the UVS-ESPRIT algorithm [21].

The approach that estimates the DOA based on its cyclostationarity was found to be advantageous when there is spectral overlap. However, the performance of this algorithm depends on the cyclostationary statistics of the signal-of-interest and the cycle frequency. The performance will also be worse than the UVS-ESPRIT algorithm when there is no spectral overlap. An advantage of this approach is that most digital communications signals possess cyclostationarity properties [37], so it is widely applicable.

The approach using higher-order statistics will not perform well in the case of spectral overlap, but has higher performance the the cyclostationarity-based approach under certain conditions. A disadvantage of this approach is that it requires the signals-of-interest to have high kurtosis. This would require the sources to have have square pulse-shaping, which is not typically used in wireless communications due to its high bandwidth [43].

Overall, this section has explored the performance of these algorithms when the frequency spectra of the sources overlap. Although it is found that these algorithms are capable of selectively estimating the source DOA, the performance depends on the statistical properties of the sources involved and the source carrier frequencies. The remainder of this chapter discusses additional results that affect the performance of these algorithms and their capabilities.

4.4 Additional Results

In this section, other factors that affect the performance of these algorithms are discussed. The effect on performance of the time-lag and the time-series invariance when various source carriers are present is shown for non-deterministic sources. Then, the affect on performance of the source spatial diversity on the total number of resolvable source DOAs is shown. Finally, the algorithm based on higher-order statistics is shown to be capable of estimating the DOA of more sources than sensor elements depending on the source carrier frequencies.

4.4.1 Time-Lag for Non-Deterministic Sources

It is mentioned in section 3.1 that the the time-lag between the two data sets will impact the performance of the UVS-ESPRIT algorithm for digitally modulated sources. Ideally, the time-lag will be as small as possible for the case of digital sources. There must also be distinct phase-offsets maintained, which will depend on the source carriers present. The impact of the time-lag on the performance of the algorithm for PAM sources is compared to the performance for deterministic harmonic sources in Figure 4.20 when estimating the DOA of two diversely polarized sources. Both sources have a symbol period where $T_{sym} = 32$ samples and raised-cosine pulse-shaping. The decline in performance occurs because the iid symbols are uncorrelated in the digital sources, which does not occur for the deterministic harmonic source.

Furthermore, the importance of both time-lag and distinct phase offsets is emphasized by letting the carriers be harmonic, such that $f_c \in \{0.00, 0.50\}$. The RMSE is high for every even sample, because the phase offsets are not distinct. The reason this occurs is due to the relationship between the phase offsets and the signal subspace eigenvectors discussed previously in section 3.1.

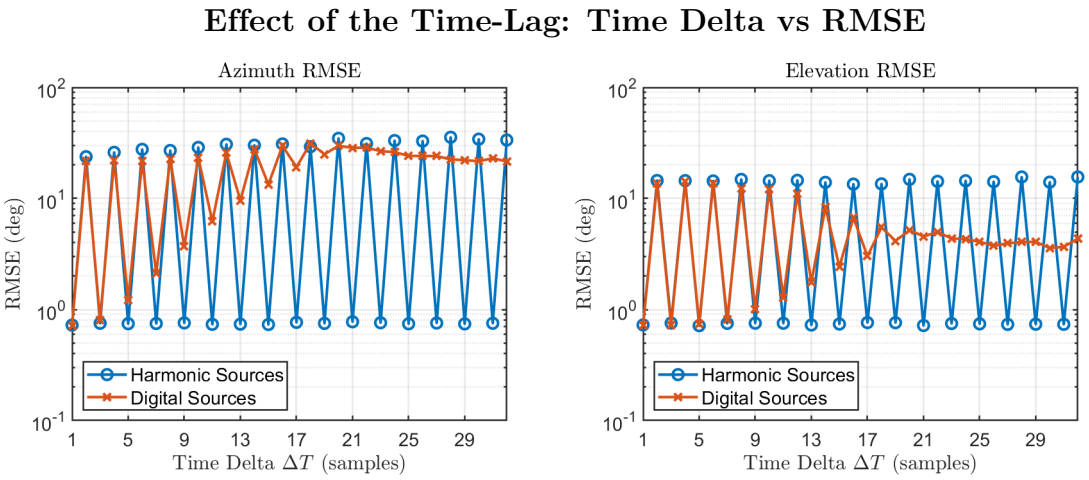

(a) Azimuth, ϕ (b) Elevation, θ

Figure 4.20: RMSE of the UVS-ESPRIT algorithm for harmonic and digitally modulated sources as the time lag increases, where $f_c \in \{0.0, 0.5\}$.

4.4.2 Spatial Diversity and Observability

As previously discussed, the linear dependence of the source array manifolds will affect the total number of sources than can be estimated. This is shown for a noiseless case with close spacing in the spatial coordinates between the sources, resulting in linear dependence between the array manifolds. The estimates are presented against the true values for $K = 16$ sources and $T = 32$ trials using the approach in Appendix A. This is performed twice, but with a different fixed DOA for the sources in each case, as shown in Figure 4.21. In the first case, four sources have a fixed elevation, but change in the second case. The introduction of spatial diversity improves the performance of the algorithm, as shown visually by the decreased variance of the estimates. The theoretical limit to the number of sources that may be estimated is also proposed by Cardoso and Chevalier [6, 11], but it is seen that this limit may depend on the linear independence between the array manifold vectors of the electromagnetic vector-sensor. Note that this refers to *linear* independence, which should not be confused with statistical independence.

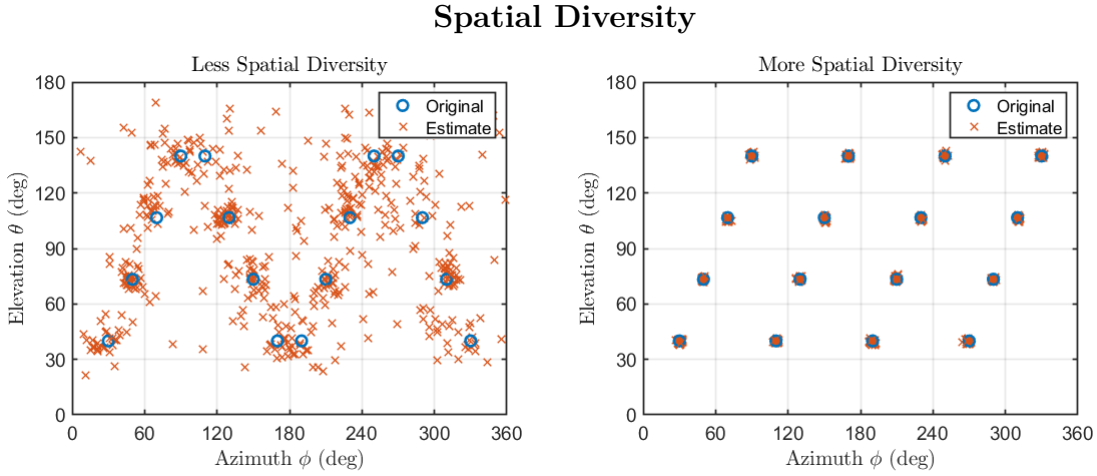

(a) Less spatial diversity (b) More spatial diversity

Figure 4.21: Estimates for fixed azimuth and elevation for $K = 16$ sources and $T = 32$ trials.

4.4.3 Estimating More Sources Than Sensor Elements

It is possible to estimate a larger number of sources than there are sensor elements. This is demonstrated using the Cumulant UVS-ESPRIT algorithm for a large number of samples, where $N = 10 \cdot 1024$, and high SNR of 10dB. Three trials are presented with a different number of sources in each trial. The estimated DOA compared to the original DOA is presented in Figure 4.22. The estimates match the true parameter, which is generally the case given the conditions of the simulation. Estimation of a large number of sources depends on the spatial and polarization parameters among the sources [31].

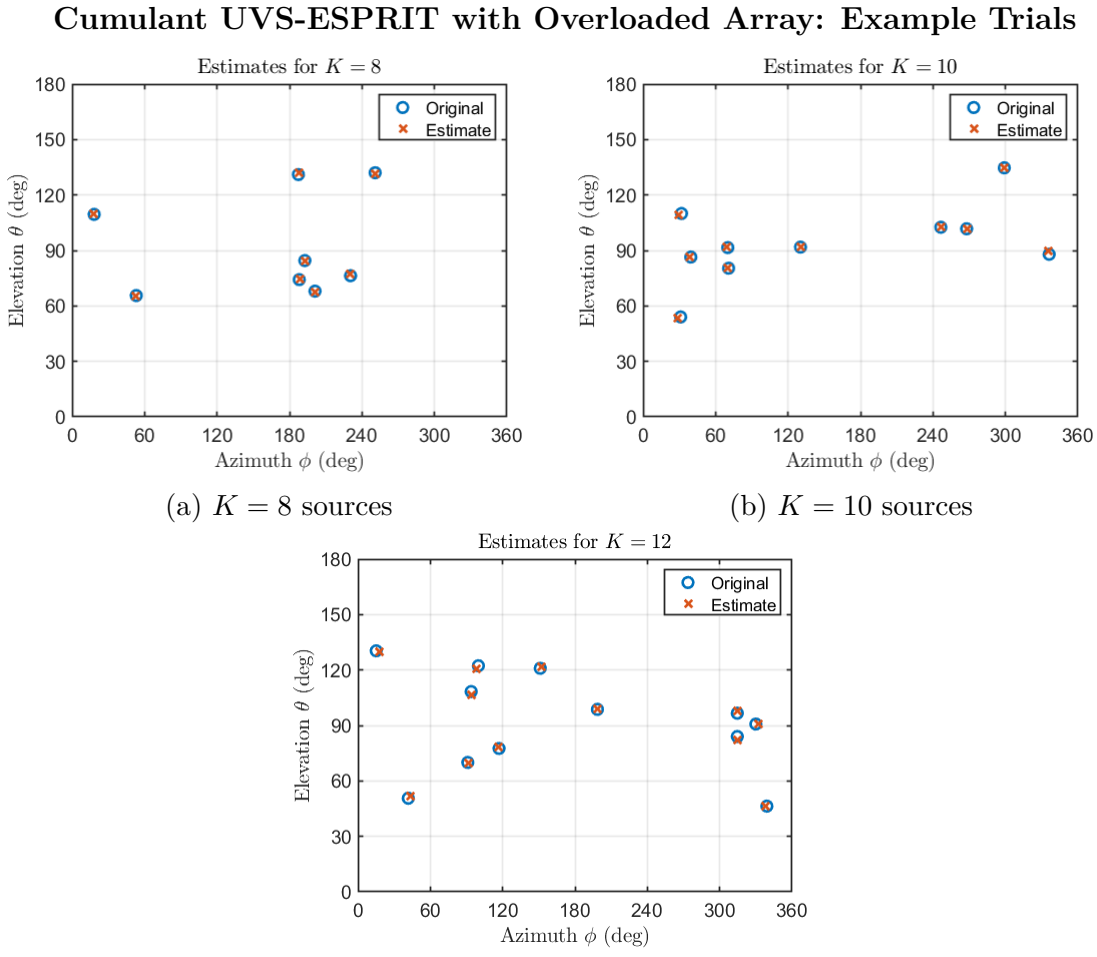

(a) $K = 8$ sources

(b) $K = 10$ sources

(c) $K = 12$ sources

Figure 4.22: Example trials where $\phi \sim \text{Unif}[0°, 360°]$ and $\theta \sim \text{Unif}[45°, 135°]$.

Several factors will influence the performance of the the Cumulant UVS-ESPRIT algorithm when there are a large number of sources. First, as the number of sources increases, the spatial and polarization diversity will decrease, causing the array manifold vectors of the sources to be linearly dependent. Secondly, the spectral overlap among the sources will become increasing large, which is an issue for the implementation of this algorithm.

This simulation demonstrates the effect of the frequency spacing on performance. For this case there are $N = 2048$ snapshots, $K = 8$ sources, a high SNR of 10dB for each source, and a symbol period of $T_{sym} = 128$ for the square pulse-shaping. The DOA of each source is fixed for each trial and $T = 32$ trials are ran. The first simulation considers the case where there is equal spacing among the source carriers in the frequency spectrum, such that the spacing is $\Delta f = 1/K$. The second case randomizes the source carrier of each source for each trial, so the carriers are shifted by a uniformly random value of $f_{shift} \sim \text{Unif}[0, \Delta f/4]$, so that the carriers of the second trial $f_{k,2} = f_{k,1} + f_{shift}$. This is done because the sources are dependent on multiple distinct phase offsets as described in section 3.3. The results of these simulations are presented in Figure 4.23.

As shown, the estimates when the source carriers have equal frequency spacing have higher variance than when the frequency spacing is generally not equal due to statistical variation. These results agree with the theory discussed in section 3.3 and with the results for the spectral overlap for the Cumulant UVS-ESPRIT algorithm discussed in section 4.3. Not only does the frequency spectrum become increasingly crowded as the number of sources increases, but the number of phase offsets in the ESPRIT algorithm that this approach depends on will increase as well.

Cumulant UVS-ESPRIT with Overloaded Array: Variable Frequency Spacing

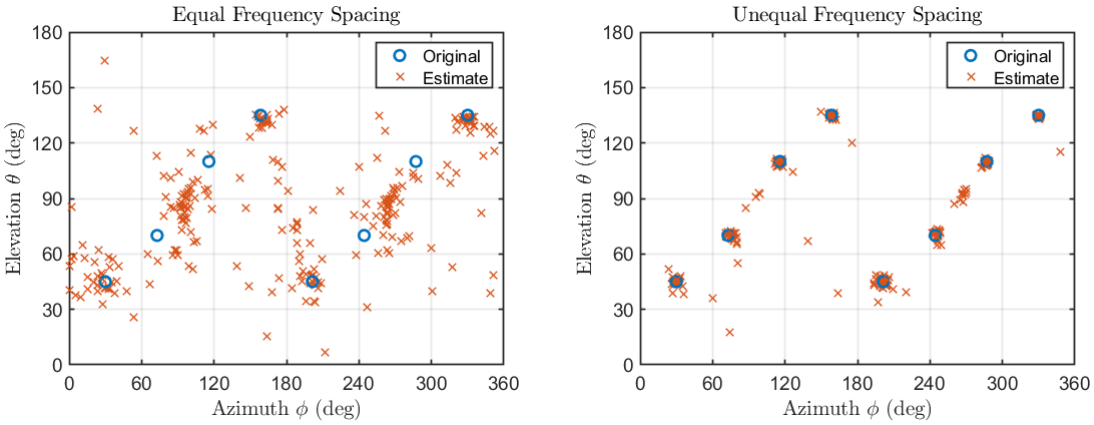

(a) Equal Spacing (b) Unequal Spacing

Figure 4.23: Cumulant UVS-ESPRIT algorithm for a large number of sources and variable frequency spacing.

4.5 Algorithm Comparison

This section provides a concise summary of each approach presented below. An additional approach using independent component analysis only is described in Appendix A, but this approach is not capable of selectively estimating the source DOA in the presence of interference.

Algorithm Comparison	
UVS-ESPRIT	Estimates the DOA of up to five sources. High resolution. Cannot selectively estimate source DOA. Requires distinct carrier frequencies.
Cyclic UVS-ESPRIT	Selectively estimates the source DOA based on cyclostationary properties. High resolution. Performance depends on source cyclostationary properties. Capable of estimating the DOA when carrier frequencies are not distinct.
Cumulant UVS-ESPRIT	Selectively estimates the source DOA based on fourth-order statistics. High resolution. Performance depends on source carrier frequencies and higher-order statistics. Can estimate the DOA of a large number of sources, depending on source carrier frequencies.

Table 4.1: Comparison of the algorithms discussed in this thesis.

Chapter 5

Conclusions

This chapter concludes the thesis. The first section summarizes its content and reiterates the most important points from each chapter. Finally, recommendations for future work are made based on the work that was done.

5.1 Summary

This thesis has described the application of signal-selective DOA estimation algorithms to a single electromagnetic vector-sensor. It is shown how the UVS-ESPRIT algorithm may be applied to non-deterministic sources for a single electromagnetic vector-sensor and that the performance of this algorithm is excellent for up to five sources, provided there is not substantial overlap between the sources. Two ESPRIT-based algorithms have been formulated for the electromagnetic vector-sensor based on cyclostationarity and higher-order statistics, which are approaches that are known to be robust to interference. The developed cumulant-based UVS-ESPRIT algorithm relies on the application of independent component analysis through the JADE algorithm devised by Cardoso [8]. The performance of these algorithms and their application to DOA estimation in the presence of interference are verified through simulation.

It was shown that the UVS-ESPRIT algorithm can be applied to non-deterministic sources. This will have comparable performance to the UVS-ESPRIT algorithm for harmonic sources,

but the performance will be degraded when there is spectral overlap with the source carriers responsible for the time-series invariance in the ESPRIT algorithm.

The algorithm based on cyclostationarity could be applied to selectively estimate the DOA of a signal-of-interest in the presence of interference. The performance of this algorithm depends on the cyclostationary statistics of the sources. It was shown that this algorithm will have greater performance than the UVS-ESPRIT algorithm, because the time-series invariance will be different due to the cycle frequency.

Furthermore, the algorithm based on higher-order statistics could also selectively estimate the DOA of a signal-of-interest in the presence of interference. The performance of this algorithm instead depends on the fourth-order statistics of the sources and is capable of selectively estimating the source DOA if the signal-of-interest kurtosis is high relative to the inferferers. Furthermore, this algorithm was found to be influenced by the spacing of the source carrier frequencies.

Overall, this thesis thoroughly investigates the application of ESPRIT-based DOA estimation algorithms for a single electromagnetic vector-sensor in the presence of interference. An ESPRIT-based approach is devised for the vector-sensor that relies on independent component analysis.

5.2 Future Work

Although this thesis provides a thorough investigation into the application of ESPRIT-based DOA estimation algorithms for a single electromagnetic vector-sensor, it has only breached this subject. There are still several areas left to explore in the area of signal processing for this sensor, including ESPRIT-based approaches. Possible future work in this area is now

discussed.

First, this thesis has not touched on the subject of cyclic cumulants [20]. Although the applications of cyclostationarity and higher-order statistics have been discussed, this approach has not been taken. Cyclostationarity was found to correct problems related to the spectral overlap, which may improve the performance of the cumulant-based ESPRIT approach. However, such an approach may be unwieldy and impractical, since it requires prior knowledge of the cycle frequencies.

Secondly, there may be additional applications involving independent component analysis applied to a single electromagnetic vector-sensor. Although it was found that independent component analysis may be applied to the cumulant-based ESPRIT algorithm, there may be additional applications, since the DOA can be directly estimated from the array manifold vectors. Furthermore, the approach taken to the cumulant-based algorithm may not be optimal and other approaches may not have the same problem with spectral overlap and frequency spacing.

Other possible future work for this sensor includes the application of algorithms that exploit time. This sensor cannot rely on the spatial displacement between the array elements that are typically used in array signal processing. For example, temporal smoothing, in contrast with spatial smoothing, may be applied to the electromagnetic vector-sensor, which is beneficial in multipath environments [69].

Overall, there may still be work that can be done on signal-selective DOA estimation involving a single electromagnetic vector-sensor in the future.

Bibliography

[1] M. Adrat, J. Leduc, S. Couturier, M. Antweiler, and H. Elders-Boll. 2nd order cyclostationarity of OFDM signals: Impact of pilot tones and cyclic prefix. In *2009 IEEE International Conference on Communications*, pages 1–5. doi: 10.1109/ICC.2009.5198574. ISSN: 1938-1883.

[2] A. Ahmed, S. A. Hamza, and M. Tufail. Comparative analysis of fourth order cumulant based esprit algorithms. In *2014 12th International Conference on Frontiers of Information Technology*, pages 133–138, 2014.

[3] G. S. Antonio, W. W. Lee, and M. Parent. High frequency vector sensor design and testing. In *2013 US National Committee of URSI National Radio Science Meeting (USNC-URSI NRSM)*, pages 1–1, 2013.

[4] S. Appadwedula and C.M. Keller. Direction-finding results for a vector sensor antenna on a small UAV. In *Fourth IEEE Workshop on Sensor Array and Multichannel Processing, 2006.*, pages 74–78. doi: 10.1109/SAM.2006.1706094. ISSN: 2151-870X.

[5] J. Cardoso. Eigen-structure of the fourth-order cumulant tensor with application to the blind source separation problem. In *International Conference on Acoustics, Speech, and Signal Processing*, pages 2655–2658 vol.5, 1990.

[6] J. Cardoso. Super-symmetric decomposition of the fourth-order cumulant tensor. blind identification of more sources than sensors. In *[Proceedings] ICASSP 91: 1991 International Conference on Acoustics, Speech, and Signal Processing*, pages 3109–3112 vol.5, 1991.

[7] J. Cardoso and E. Moulines. Asymptotic performance analysis of direction-finding algorithms based on fourth-order cumulants. *IEEE Transactions on Signal Processing*, 43(1):214–224, 1995.

[8] Jean-François Cardoso and Antoine Souloumiac. Blind beamforming for non Gaussian signals. *IEE Proceedings-F*, 140(6):362–370, December 1993.

[9] Jean-François Cardoso. Higher-order narrow-band array processing. 1991.

[10] G. Casella and R.L. Berger. *Statistical Inference*. Duxbury advanced series in statistics and decision sciences. Thomson Learning. ISBN 978-0-534-24312-8.

[11] P. Chevalier and A. Ferreol. On the virtual array concept for the fourth-order direction finding problem. *IEEE Transactions on Signal Processing*, 47(9):2592–2595, 1999.

[12] Hsing-Hsing Chiang and C.L. Nikias. The esprit algorithm with higher-order statistics. In *Workshop on Higher-Order Spectral Analysis*, pages 163–168. doi: 10.1109/HOSA.1989.735289.

[13] Y.S. Cho, J. Kim, W.Y. Yang, and C.G. Kang. *MIMO-OFDM Wireless Communications with MATLAB*. Wiley - IEEE. Wiley, 2010. ISBN 978-0-470-82562-4.

[14] A. Cichocki, D. Mandic, L. De Lathauwer, G. Zhou, Q. Zhao, C. Caiafa, and H. A. PHAN. Tensor decompositions for signal processing applications: From two-way to multiway component analysis. *IEEE Signal Processing Magazine*, 32(2):145–163, 2015.

[15] G.A. Deschamps. Techniques for Handling Elliptically Polarized Waves with Special Reference to Antennas: Part II - Geometrical Representation of the Polarization of a Plane Electromagnetic Wave. *Proceedings of the IRE*, 39(5):540–544, May 1951. ISSN 2162-6634. doi: 10.1109/JRPROC.1951.233136. Conference Name: Proceedings of the IRE.

[16] M. C. Dogan and J. M. Mendel. Applications of cumulants to array processing. ii. non-gaussian noise suppression. *IEEE Transactions on Signal Processing*, 43(7):1663–1676, 1995.

[17] M. C. Dogan and J. M. Mendel. Applications of cumulants to array processing .i. aperture extension and array calibration. *IEEE Transactions on Signal Processing*, 43 (5):1200–1216, 1995.

[18] Changlai Du, Huacheng Zeng, Wenjing Lou, and Y. Thomas Hou. On cyclostationary analysis of WiFi signals for direction estimation. In *2015 IEEE International Conference on Communications (ICC)*, pages 3557–3561. doi: 10.1109/ICC.2015.7248876. ISSN: 1938-1883.

[19] W. A. Gardner. Simplification of music and esprit by exploitation of cyclostationarity. *Proceedings of the IEEE*, 76(7):845–847, 1988.

[20] W. A. Gardner and C. M. Spooner. The cumulant theory of cyclostationary time-series. i. foundation. *IEEE Transactions on Signal Processing*, 42(12):3387–3408, 1994.

[21] W.A. Gardner. *Cyclostationarity in Communications and Signal Processing*. Electrical Engineering, Communications, and Signal Processing. IEEE Press, 1994. ISBN 978-0-7803-0434-5.

[22] William A. Gardner, Antonio Napolitano, and Luigi Paura. Cyclostationarity: Half a century of research. 86(4):639–697. ISSN 0165-1684. doi: 10.1016/j.sigpro.2005.06.016.

[23] E. Gonen and J. M. Mendel. Applications of cumulants to array processing. iii. blind beamforming for coherent signals. *IEEE Transactions on Signal Processing*, 45(9): 2252–2264, 1997.

[24] E. Gonen and J. M. Mendel. Applications of cumulants to array processing. part vi. polarization and direction of arrival estimation with minimally constrained arrays. *IEEE Transactions on Signal Processing*, 47(9):2589–2592, 1999.

[25] E. Gonen, J. M. Mendel, and M. C. Dogan. Applications of cumulants to array processing. iv. direction finding in coherent signals case. *IEEE Transactions on Signal Processing*, 45(9):2265–2276, 1997.

[26] X. Gong, Z. Liu, and Y. Xu. Regularised parallel factor analysis for the estimation of direction-of-arrival and polarisation with a single electromagnetic vector-sensor. *IET Signal Processing*, 5(4):390–396, 2011.

[27] G. F. Hatke. Conditions for unambiguous source location using polarization diverse arrays. In *Proceedings of 27th Asilomar Conference on Signals, Systems and Computers*, pages 1365–1369 vol.2, 1993.

[28] Simon Haykin, David J. Thomson, and Jeffrey H. Reed. Spectrum sensing for cognitive radio. 97(5):849–877. ISSN 1558-2256. doi: 10.1109/JPROC.2009.2015711. Conference Name: Proceedings of the IEEE.

[29] Jingfei Jiang and Jianqiu Zhang. A weighted inner product estimator in the geometric algebra of euclidean 3-space for source localization using an EM vector-sensor. 25(1): 83–93. ISSN 1000-9361. doi: 10.1016/S1000-9361(11)60365-8.

[30] Kah-Chye Tan, Kwok-Chiang Ho, and A. Nehorai. Uniqueness study of measurements obtainable with arrays of electromagnetic vector sensors. *IEEE Transactions on Signal Processing*, 44(4):1036–1039, 1996.

[31] Kah-Chye Tan, Kwok-Chiang Ho, and A. Nehorai. Linear independence of steering

vectors of an electromagnetic vector sensor. *IEEE Transactions on Signal Processing*, 44(12):3099–3107, 1996.

[32] Kwok-Chiang Ho, Kah-Chye Tan, and B. T. G. Tan. Efficient method for estimating directions-of-arrival of partially polarized signals with electromagnetic vector sensors. *IEEE Transactions on Signal Processing*, 45(10):2485–2498, 1997.

[33] Kwok-Chiang Ho, Kah-Chye Tan, and A. Nehorai. Estimating directions of arrival of completely and incompletely polarized signals with electromagnetic vector sensors. *IEEE Transactions on Signal Processing*, 47(10):2845–2852, 1999.

[34] S. Lie, A. R. Leyman, and Y. H. Chew. Fourth-order and weighted mixed order direction-of-arrival estimators. *IEEE Signal Processing Letters*, 13(11):691–694, 2006.

[35] Vijay Madisetti. *The Digital Signal Processing Handbook*. CRC Press. ISBN 978-0-8493-8572-8.

[36] J. M. Mendel. Tutorial on higher-order statistics (spectra) in signal processing and system theory: Theoretical results and some applications. *Proceedings of the IEEE*, 79 (3):278–305, 1991.

[37] A. Napolitano. *Cyclostationary Processes and Time Series: Theory, Applications, and Generalizations*. Elsevier Science, 2019. ISBN 978-0-08-102708-0.

[38] Antonio Napolitano. Cyclostationarity: New trends and applications. 120:385 – 408. ISSN 0165-1684. doi: https://doi.org/10.1016/j.sigpro.2015.09.011.

[39] A. Nehorai and E. Paldi. Vector-sensor array processing for electromagnetic source localization. *IEEE Transactions on Signal Processing*, 42(2):376–398, February 1994. ISSN 1053-587X. doi: 10.1109/78.275610.

[40] A. Nehorai and P. Tichavsky. Cross-product algorithms for source tracking using an em vector sensor. *IEEE Transactions on Signal Processing*, 47(10):2863–2867, 1999.

[41] H. Ochiai. High-order statistical analysis for linearly modulated signals. In *MILCOM 2015 - 2015 IEEE Military Communications Conference*, pages 1524–1529, 2015.

[42] R. Pan and C. L. Nikias. Harmonic decomposition methods in cumulant domains (array processing). In *ICASSP-88., International Conference on Acoustics, Speech, and Signal Processing*, pages 2356–2359 vol.4, 1988.

[43] J.G. Proakis and D.G. Manolakis. *Digital Signal Processing*. Prentice Hall International Editions. Pearson Prentice Hall, 2007. ISBN 978-0-13-187374-2.

[44] John G. Proakis. *Digital Communications*. McGraw-Hill, 2008. ISBN 978-1-283-38746-0.

[45] R. Roy and T. Kailath. Esprit-estimation of signal parameters via rotational invariance techniques. *IEEE Transactions on Acoustics, Speech, and Signal Processing*, 37(7): 984–995, July 1989. doi: 10.1109/29.32276.

[46] R. Roy, A. Paulraj, and T. Kailath. Esprit–a subspace rotation approach to estimation of parameters of cisoids in noise. *IEEE Transactions on Acoustics, Speech, and Signal Processing*, 34(5):1340–1342, 1986.

[47] H. Sawada, R. Mukai, and S. Makino. Direction of arrival estimation for multiple source signals using independent component analysis. In *Seventh International Symposium on Signal Processing and Its Applications, 2003. Proceedings.*, volume 2, pages 411–414 vol.2, 2003.

[48] R. Schmidt. Multiple emitter location and signal parameter estimation. *IEEE Transactions on Antennas and Propagation*, 34(3):276–280, March 1986. ISSN 1558-2221. doi:

10.1109/TAP.1986.1143830. Conference Name: IEEE Transactions on Antennas and Propagation.

[49] Francois-Xavier Socheleau, Philippe Ciblat, and Sebastien Houcke. OFDM system identification for cognitive radio based on pilot-induced cyclostationarity. In *2009 IEEE Wireless Communications and Networking Conference*, pages 1–6. doi: 10.1109/WCNC.2009.4917840. ISSN: 1558-2612.

[50] Paul D. Sutton, Keith E. Nolan, and Linda E. Doyle. Cyclostationary signatures in practical cognitive radio applications. 26(1):13–24. ISSN 1558-0008. doi: 10.1109/JSAC.2008.080103.

[51] A. Swami and B. M. Sadler. Hierarchical digital modulation classification using cumulants. *IEEE Transactions on Communications*, 48(3):416–429, 2000.

[52] A. Swami, J.M. Mendel, C.L. Nikias, and Inc MathWorks. *Higher-Order Spectral Analysis Toolbox: For Use with MATLAB*. MathWorks partner series. MathWorks.

[53] A. L. Swindlehurst, B. Ottersten, R. Roy, and T. Kailath. Multiple invariance esprit. *IEEE Transactions on Signal Processing*, 40(4):867–881, 1992.

[54] Jian-wu Tao, Qiong-jian Fan, and Fei Yu. Stokes parameters and DOAs estimation of partially polarized sources using a EM vector sensor. 11(4):737–744. ISSN 1863-1711. doi: 10.1007/s11760-016-1017-z.

[55] S. Theodoridis and R. Chellappa. *Academic Press Library in Signal Processing: Array and Statistical Signal Processing*, volume 3 of *ISSN*. Elsevier Science. ISBN 978-0-12-411621-4.

[56] G.B. Thomas, M.D. Weir, J. Hass, and F.R. Giordano. *Thomas' Calculus*. Addison-Wesley Longman, Incorporated. ISBN 978-0-321-22651-8.

[57] Tsung-Hsien Liu and J. M. Mendel. Application of cumulants to array signal processing .v. sensitivity issues. *IEEE Transactions on Signal Processing*, 47(3):746–759, 1999.

[58] T. Engin Tuncer and Benjamin Friedlander. *Classical and Modern Direction-of-Arrival Estimation*. Academic Press, July 2009. ISBN 978-0-08-092307-9.

[59] H.L. Van Trees. *Optimum Array Processing: Part IV of Detection, Estimation, and Modulation Theory*. Detection, Estimation, and Modulation Theory. Wiley, 2004. ISBN 9780471463832.

[60] Lanmei Wang, Le Yang, Guibao Wang, Zhihai Chen, and Minggao Zou. Uni-vector-sensor dimensionality reduction MUSIC algorithm for DOA and polarization estimation. 2014:682472. ISSN 1024-123X. doi: 10.1155/2014/682472. Publisher: Hindawi Publishing Corporation.

[61] K. T. Wong and M. D. Zoltowski. Uni-vector-sensor esprit for multisource azimuth, elevation, and polarization estimation. *IEEE Transactions on Antennas and Propagation*, 45(10):1467–1474, October 1997. ISSN 0018-926X. doi: 10.1109/8.633852.

[62] K. T. Wong and M. D. Zoltowski. Closed-form direction finding and polarization estimation with arbitrarily spaced electromagnetic vector-sensors at unknown locations. *IEEE Transactions on Antennas and Propagation*, 48(5):671–681, 2000.

[63] Kainam Thomas Wong and Xin Yuan. "vector cross-product direction-finding" with an electromagnetic vector-sensor of six orthogonally oriented but spatially noncollocating dipoles/loops. *IEEE Transactions on Signal Processing*, 59(1):160–171, January 2011. ISSN 1941-0476. doi: 10.1109/TSP.2010.2084085. Conference Name: IEEE Transactions on Signal Processing.

[64] Y. Xu and Z. Liu. On single-vector-sensor direction finding for linearly polarized sources

having non-circular constellations. In *2006 8th international Conference on Signal Processing*, volume 1, 2006.

[65] Y. Xu, Z. Liu, K. T. Wong, and J. Cao. Virtual-manifold ambiguity in hos-based direction-finding with electromagnetic vector-sensors. *IEEE Transactions on Aerospace and Electronic Systems*, 44(4):1291–1308, 2008.

[66] You Gen Xu and Zhi Wen Liu. Regularized esprit-based direction finding and polarization estimation with one electromagnetic vector sensor. In *Proceedings 7th International Conference on Signal Processing, 2004. Proceedings. ICSP '04. 2004.*, volume 1, pages 399–402 vol.1, 2004.

[67] X. Yuan. Estimating the doa and the polarization of a polynomial-phase signal using a single polarized vector-sensor. *IEEE Transactions on Signal Processing*, 60(3): 1270–1282, 2012.

[68] N. Yuen and B. Friedlander. Asymptotic performance analysis of esprit, higher order esprit, and virtual esprit algorithms. *IEEE Transactions on Signal Processing*, 44(10): 2537–2550, 1996.

[69] Zhenghui Gu and E. Gunawan. A performance analysis of multipath direction finding with temporal smoothing. *IEEE Signal Processing Letters*, 10(7):200–203, 2003.

[70] Zhigang Liu, Jinkuan Wang, and Yanbo Xue. Unitary cyclic esprit-like direction finding. In *2005 Asia-Pacific Microwave Conference Proceedings*, volume 3, pages 4 pp.–, 2005.

[71] M. D. Zoltowski and K. T. Wong. Esprit-based 2-d direction finding with a sparse uniform array of electromagnetic vector sensors. *IEEE Transactions on Signal Processing*, 48(8):2195–2204, 2000.

Appendices

Appendix A

Independent Component Analysis for DOA Estimation

It can be observed from the signal model that DOA estimation for a single electromagnetic vector-sensor approached as a blind source separation problem. Although this approach does not appear to have applications to DOA estimation in the presence of interference, it is found that it can estimate the DOA of more sources than sensor elements depending on the pulse-shaping, although further analysis of this approach is required. It may also estimate the DOA of sources with the same carrier frequency. However, this approach has low-resolution compared to the subspace techniques.

In general, it is known that independent component analysis can be applied to the DOA estimation problem [8, 47]. This approach demonstrates a simple application of independent component analysis to the electromagnetic vector-sensor, which operates on the higher-order statistics to find the array manifold vectors through the non-Gaussianity of the sources, which can be used to obtain the DOA with a single electromagnetic vector-sensor.

Although this approach is capable of estimating the DOA of more sources than sensor elements, it does have drawbacks. The performance of this algorithm in the presence of multiple sources is poor, relative to the ESPRIT-based approach, and degrades as the number of sources increases. Therefore, DOA estimation of a large number of sources appears to require high SNR or a noiseless environment. The performance of this algorithm is mentioned at

the end of this section.

The application of independent component analysis to the DOA estimation problem for a single electromagnetic vector-sensor involves the JADE algorithm by Cardoso [8], although any independent component analysis algorithm that operates on complex-valued data should be applicable to this problem. Let the independent component analysis algorithm be described by the function $\mathcal{L}_{JADE}(\cdot)$. As long as the sources are statistically independent, this can be applied to the received data as follows, where $\boldsymbol{A}$ would be the mixing matrix in the blind source separation problem.

$$\hat{\boldsymbol{A}} = \mathcal{L}_{JADE}(\boldsymbol{Y}) \tag{A.1}$$

For the case of $K > M$ sources, more sources than sensor elements can be estimated with square pulse-shaping, although this approach requires further analysis. A new data set is constructed that increases the total rows to $2M$ by partitioning a time-delayed data set to the original data set. This time-delayed data set will result in a new set of time-series data by sampling across the rising and falling edges of the square pulse shape. Ideally, the time-lag τ is small, since there will be a finite number of samples available.

$$\tilde{\boldsymbol{y}}(t) = \begin{bmatrix} \boldsymbol{y}_1(t) \\ \boldsymbol{y}_2(t) \end{bmatrix} = \begin{bmatrix} \boldsymbol{y}_1(t) \\ \boldsymbol{y}_1(t-\tau) \end{bmatrix}$$

Where $\tilde{\boldsymbol{Y}}$ is the new data matrix sampled from the time-series data. Likewise, for an excessively large number of sources, such that $K > (J-1)M$, the data vector is constructed as follows.

$$\tilde{\boldsymbol{y}}(t) = \begin{bmatrix} \boldsymbol{y}_1(t) \\ \boldsymbol{y}_2(t) \\ \vdots \\ \boldsymbol{y}_i(t) \\ \vdots \\ \boldsymbol{y}_J(t) \end{bmatrix} = \begin{bmatrix} \boldsymbol{y}_1(t) \\ \boldsymbol{y}_1(t-\tau_1) \\ \vdots \\ \boldsymbol{y}_1(t-\tau_{i-1}) \\ \vdots \\ \boldsymbol{y}_1(t-\tau_{J-1}) \end{bmatrix}$$

The array manifold of the constructed data can be estimated from the rows of $\hat{\tilde{\boldsymbol{A}}}$. The DOA for the kth source is then obtained from the Poynting vector of the estimated array manifold contained within the first M rows of the kth column.

$$\hat{\tilde{\boldsymbol{A}}} = \mathcal{L}_{JADE}(\tilde{\boldsymbol{Y}}) \tag{A.2}$$

To conclude, this section describes a simple application of independent component analysis to the DOA estimation problem for a single electromagnetic vector-sensor. This does not perform as well as the high-resolution subspace techniques, but is capable of estimating the DOA of more sources than sensor elements.

Performance of Independent Component Analysis with JADE

This section presents the performance of the independent component analysis algorithm JADE [8] when applied to DOA estimation with a single electromagnetic vector-sensor. Although the performance of JADE will be worse than the subspace approach, it is capable of estimating the DOA of a large number of sources with arbitrary spectral overlap, even if sources have the same carrier frequency. The results of the simulations for diverse polarization and up to five sources are shown in Figure A.1. The performance of independent component analysis is sensitive to the number of sources in spite of its ability to estimate the DOA of a large number of sources without noise.

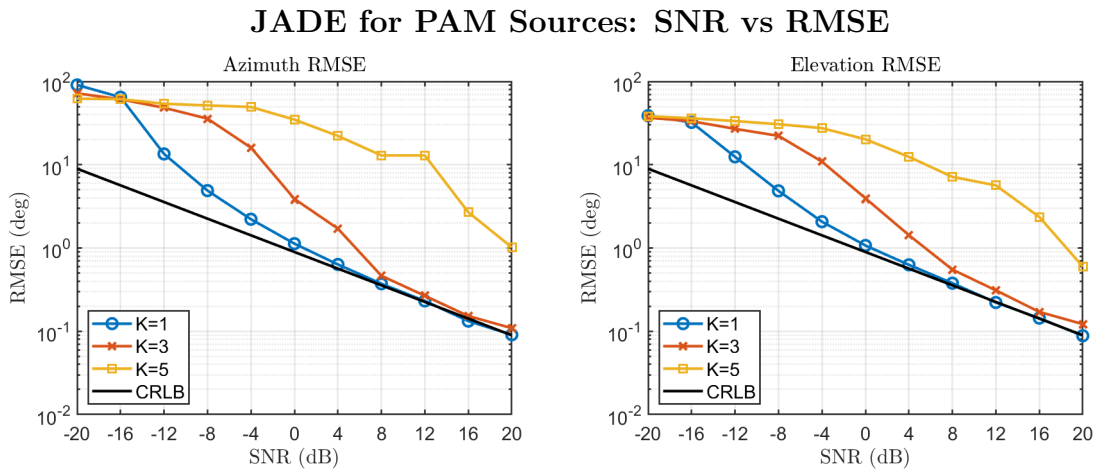

(a) Azimuth, ϕ (b) Elevation, θ

Figure A.1: JADE RMSE for up to five diversely polarized PAM digital sources.

Estimating More Sources Than Sensor Elements with JADE

This section shows how the independent component analysis algorithm JADE can be used to estimate the DOA of a large number of sources using the approach with square pulse-shaping and partitioning the data set. The results of the simulations for $N = 2048$ snapshots, $K = 16$ sources, $T_{sym} = 32$ samples with square pulse-shaping, a time-lag $\tau_i = i$ samples for each partitioned data set, and a fixed DOA for $T = 32$ trials is polarization and up to five sources are shown in Figure A.2. The performance of independent component analysis is found to be sensitive to the spatial diversity of the sources.

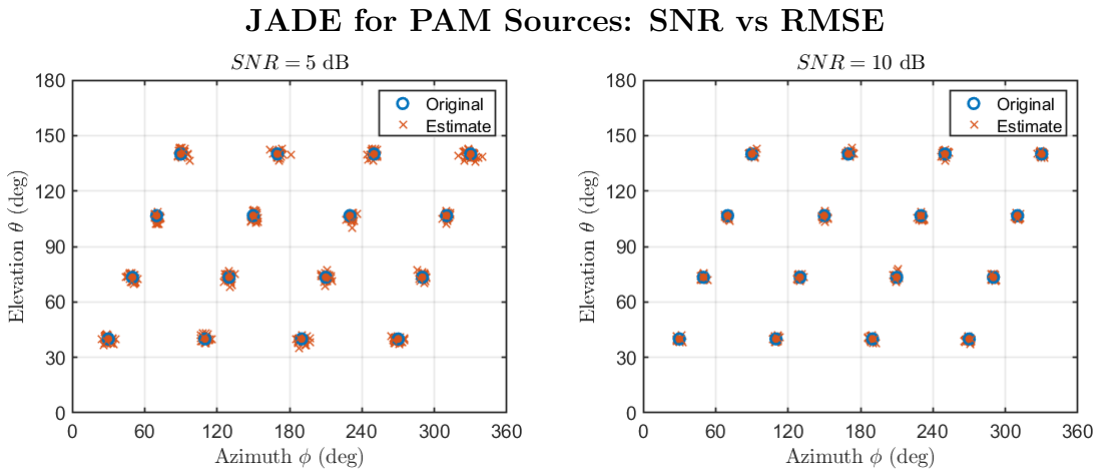

(a) 5dB SNR (b) 10dB SNR

Figure A.2: JADE estimating the DOA of more sources than sensor elements for various SNR.

Appendix B

Simulation Conditions

Tables showing simulation conditions for each figure so the results may be reproduced.

UVS-ESPRIT without Interference for Harmonic and Digital Sources			
Fig.	Simulation	Source	Signal
4.2	$N = 2048$ $T = 2000$ $\boldsymbol{\tau} = [0, 1]$	$\phi \in [0°, 360°]$ $\theta \in [80°, 100°]$ $\boldsymbol{\gamma} = [0°, 45°, 90°, 45°, 45°]$ $\boldsymbol{\eta} = [0°, 90°, 0°, -90°, 0°]$	$\boldsymbol{f} = [0.0, 0.2, 0.4, 0.6, 0.8]$ Harmonic Signals
4.3	$N = 2048$ $T = 2000$ $\boldsymbol{\tau} = [0, 1]$	$\phi \in [0°, 360°]$ $\theta \in [80°, 100°]$ $\gamma \sim \text{Unif}[0°, 90°]$ $\boldsymbol{\eta} = \mathbf{0}$	$\boldsymbol{f} = [0.0, 0.2, 0.4, 0.6, 0.8]$ Harmonic Signals
4.4	$N = 2048$ $T = 2000$ $\boldsymbol{\tau} = [0, 1]$	$\phi \in [0°, 360°]$ $\theta \in [80°, 100°]$ $\boldsymbol{\gamma} = [0°, 45°, 90°, 45°, 45°]$ $\boldsymbol{\eta} = [0°, 90°, 0°, -90°, 0°]$	$\boldsymbol{f} = [0.0, 0.2, 0.4, 0.6, 0.8]$ PAM Digital Signals $T_{sym} = 64$, QPSK Raised-Cosine Pulses, $r = 1$
4.5	$N = 2048$ $T = 2000$ $\boldsymbol{\tau} = [0, 1]$	$\phi \in [0°, 360°]$ $\theta \in [80°, 100°]$ $\gamma \sim \text{Unif}[0°, 90°]$ $\boldsymbol{\eta} = \mathbf{0}$	$\boldsymbol{f} = [0.0, 0.2, 0.4, 0.6, 0.8]$ PAM Digital Signals $T_{sym} = 64$, QPSK Raised-Cosine Pulses, $r = 1$
4.6	$N = 2048$ $T = 500$ $\boldsymbol{\tau} = [0, 1]$	$\phi \in [0°, 360°]$ $\theta \in [80°, 100°]$ $\boldsymbol{\gamma} = [0°, 45°, 90°, 45°, 45°]$ $\boldsymbol{\eta} = [0°, 90°, 0°, -90°, 0°]$	$\boldsymbol{f} = [0.0, 0.2, 0.4, 0.6, 0.8]$ OFDM Digital Signals $T_{sym} = 256$, $N_{sc} = 10$ $T_g = 0.25T_{sym}$ QPSK for each subcarrier

Table B.1: Simulations for UVS-ESPRIT without interference.

Cyclic UVS-ESPRIT and Cumulant UVS-ESPRIT without Interference			
Fig.	Simulation	Source	Signal
4.8	$N = 2048$ $T = 500$ $\alpha = 1/64$ $\boldsymbol{\tau} = [0, 1]$	$\phi \in [0°, 360°]$ $\theta \in [80°, 100°]$ $\boldsymbol{\gamma} = [0°, 45°, 90°, 45°, 45°]$ $\boldsymbol{\eta} = [0°, 90°, 0°, -90°, 0°]$	$\boldsymbol{f} = [0.0, 0.2, 0.4, 0.6, 0.8]$ PAM Digital Signals $T_{sym} = 64$, QPSK Raised-Cosine Pulses, $r = 1$
4.10	$N = 2048$ $T = 500$ $\alpha = 1/256$ $\boldsymbol{\tau} = [191, 192]$	$\phi \in [0°, 360°]$ $\theta \in [80°, 100°]$ $\boldsymbol{\gamma} = [0°, 45°, 90°, 45°, 45°]$ $\boldsymbol{\eta} = [0°, 90°, 0°, -90°, 0°]$	$\boldsymbol{f} = [0.0, 0.2, 0.4, 0.6, 0.8]$ OFDM Digital Signals $T_{sym} = 256$, $N_{sc} = 10$ $T_g = 0.25T_{sym}$ QPSK for each subcarrier
4.11	$N = 2048$ $T = 300$ $\boldsymbol{\tau} = [0, 1]$	$\phi \in [0°, 360°]$ $\theta \in [80°, 100°]$ $\boldsymbol{\gamma} = [0°, 45°, 90°, 45°, 45°]$ $\boldsymbol{\eta} = [0°, 90°, 0°, -90°, 0°]$	$\boldsymbol{f} = [0.13, 0.35, 0.73, 0.89, 0.57]$ PAM Digital Signals $T_{sym} = 64$, QPSK Square Pulses
4.12	$N = 2048$ $T = 400$ $\boldsymbol{\tau} = [0, 1]$	$\phi \in [0°, 360°]$ $\theta \in [80°, 100°]$ $\gamma = 0°$ $\eta = 0°$	$f = 0$ PAM/OFDM Signals $T_{sym} = 64$ (PAM), QPSK Square/RC, $r \in \{1.0, 0.5\}$ $T_{sym} = 256$ (OFDM) $N_{sc} = 10$, $T_g = 0.25T_{sym}$
4.13	$N = 2048$ $T = 400$ $\boldsymbol{\tau} = [0, 1]$	$\phi \in [0°, 360°]$ $\theta \in [80°, 100°]$ $\gamma = 0°$ $\eta = 0°$	f=0 PAM Digital Signals $T_{sym} = 64$, QPSK/16-QAM Square Pulses
A.1	$N = 2048$ $T = 700$ $\boldsymbol{\tau} = [0, 1]$	$\phi \in [0°, 360°]$ $\theta \in [80°, 100°]$ $\boldsymbol{\gamma} = [0°, 45°, 90°, 45°, 45°]$ $\boldsymbol{\eta} = [0°, 90°, 0°, -90°, 0°]$	$\boldsymbol{f} = [0.0, 0.2, 0.4, 0.6, 0.8]$ PAM Digital Signals $T_{sym} = 64$, QPSK Square Pulses

Table B.2: Simulations for Cyclic/Cumulant UVS-ESPRIT and the JADE algorithm without interference.

Cyclic UVS-ESPRIT and Cumulant UVS-ESPRIT with Interference			
Fig.	Simulation	Source	Signal
4.14	$N = 2048$ $T = 400$ $\alpha = 1/64$ $\boldsymbol{\tau} = [0, 1]$	$\phi \in [0°, 360°]$ $\theta_K \in [80°, 100°]$, $\theta_L = 45°$ $\boldsymbol{\gamma}_K = [0°, 45°]$, $\gamma_L = 90°$ $\boldsymbol{\eta} = [0°, 90°]$, $\eta_L = 0°$ $K = 2$, $L = 1$	$\boldsymbol{f}_K = [0.00, 0.20]$, $f_L = 0.40$ PAM Digital Signals $T_{sym} = 64$ (SOI), QPSK $T_{sym} = 44$ (SNOI), QPSK Raised-Cosine Pulses, $r = 1$
4.15	$N = 2048$ $T = 300$ $\boldsymbol{\tau} = [0, 1]$	$\phi \in [0°, 360°]$ $\theta_K \in [80°, 100°]$, $\theta_L = 45°$ $\boldsymbol{\gamma}_K = [0°, 45°]$, $\gamma_L = 90°$ $\boldsymbol{\eta} = [0°, 90°]$, $\eta_L = 0°$ $K = 2$, $L = 1$	$\boldsymbol{f}_K = [0.13, 0.35]$, $f_L = 0.73$ PAM Digital Signals $T_{sym} = 64$, QPSK Square Pulses (SOI) RC Pulses, $r = 1$ (SNOI)

Table B.3: Simulations for Cyclic/Cumulant UVS-ESPRIT with interference.

UVS-ESPRIT with Spectral Overlap			
Fig.	Simulation	Source	Signal
4.16	$N = 2048$ $T = 500$ $\boldsymbol{\tau} = [0, 1]$	$\phi \in [0°, 360°]$ $\theta \in [80°, 100°]$ $\boldsymbol{\gamma} = [0°, 45°]$ $\boldsymbol{\eta} = [0°, 90°]$	$f_k = 0.2, k = 2$ PAM Signals $T_{sym} = 64$, QPSK Raised-Cosine Pulses, $r = 1$
4.17	$N = 2048$ $T = 300$ $\alpha = 1/32$ $\boldsymbol{\tau} = [0, 1]$	$\phi \in [0°, 360°]$ $\theta \in [80°, 100°]$ $\boldsymbol{\gamma} = [0°, 45°]$ $\boldsymbol{\eta} = [0°, 90°]$	$f_k = 0.2, k = 2$ PAM Signals, QPSK $T_{sym} = 32$ (SOI) $T_{sym} = 44$ (SNOI) Raised-Cosine Pulses, $r = 1$
4.18	$N = 2048$ $T = 300$ $\alpha = 1/32$ $\boldsymbol{\tau} = [0, 1]$	$\phi \in [0°, 360°]$ $\theta \in [80°, 100°]$ $\boldsymbol{\gamma} = [0°, 45°]$ $\boldsymbol{\eta} = [0°, 90°]$	$f_k = 0.2, k = 2$ PAM Signals, QPSK $T_{sym} = 32$ (SOI) $T_{sym} = 32$ (SNOI) Raised-Cosine Pulses, $r = 1$
4.19	$N = 2048$ $T = 300$ $\boldsymbol{\tau} = [0, 1]$	$\phi \in [0°, 360°]$ $\theta \in [80°, 100°]$ $\boldsymbol{\gamma} = [0°, 45°, 90°]$ $\boldsymbol{\eta} = [0°, 90°, 0°]$	$f_k \in \{0.2, 0.3\}$ $k = 2, 3$ PAM Signals, QPSK $T_{sym} = 64$ Square Pulses

Table B.4: Simulations for UVS-ESPRIT with spectral overlap.